

✓
Digitised
15/7/09

FOR REFERENCE ONLY

21 APR 1000

40 0680271 2



ProQuest Number: 10183142

All rights reserved

INFORMATION TO ALL USERS

The quality of this reproduction is dependent upon the quality of the copy submitted.

In the unlikely event that the author did not send a complete manuscript and there are missing pages, these will be noted. Also, if material had to be removed, a note will indicate the deletion.



ProQuest 10183142

Published by ProQuest LLC (2017). Copyright of the Dissertation is held by the Author.

All rights reserved.

This work is protected against unauthorized copying under Title 17, United States Code
Microform Edition © ProQuest LLC.

ProQuest LLC.
789 East Eisenhower Parkway
P.O. Box 1346
Ann Arbor, MI 48106 – 1346

APPLICATION OF LIQUID CRYSTAL THERMOGRAPHY
IN
HEAT TRANSFER CHARACTERISTICS OF SLOT JET IMPINGEMENT

TAT LEUNG CHAN

A thesis submitted in partial fulfilment of the
requirements of The Nottingham Trent University
for the degree of Doctor of Philosophy.

This research programme was carried out in the
Department of Mechanical Engineering,
The Hong Kong Polytechnic University, Kowloon, Hong Kong
in collaboration with the
Department of Mechanical Engineering,
The Nottingham Trent University, Nottingham NG1 4BU, UK.

December 1998

© Copyright notice

This copy of the thesis has been supplied for the purpose of research or private study under the condition that anyone who consults it is understood to recognise that its copyright rests with its author and that no quotation from the thesis, no information derived from it, may be published without proper acknowledgement.

Table of Contents

Table of Contents	i
Abstract	v
Acknowledgements	vi
List of Publications	vii
List of Figures and Tables	viii
List of Appendices	xii
Nomenclature	xiii
Chapter 1 Introduction	1
1.1 Background and Description of the Problem	1
1.2 Aims and Objectives	2
1.2.1 Specific aims	
1.2.2 Rationale	
1.2.3 Objectives	
1.2.4 Breakdown of objectives	
1.3 Outline of the Investigation	6
Chapter 2 Literature Review	8
2.1 Introduction	8
2.1.1 Previous reviews of literature	
2.1.2 Flow regions description	
2.2 Experimental Heat/Mass Transfer Characteristics of an Impinging Slot/Circular Jet	10
2.2.1 Nusselt/Sherwood number correlations	
2.2.2 Effect of turbulence on stagnation point/ streamwise local heat transfer	
2.2.3 Effect of surface curvature on local/ average heat transfer	

2.3	Numerical Heat Transfer Investigations	24
2.4	Summary of Review	31
Chapter 3	Experimental Investigation	32
3.1	Introduction	32
3.2	Air Nozzle Jet System, Traverse and Ancillary Equipment	
3.2.1	Slot jet tunnel design	
3.2.2	Hot-wire anemometry system	
3.3	Thermochromic Liquid Crystal Calibration System	36
3.3.1	Thermochromic liquid crystals	
3.3.2	True colour image processing system	
3.3.3	Lighting system	
3.3.4	Selection of liquid crystal calibration technique	
3.3.5	Liquid crystal calibration facility and procedure	
3.3.6	Liquid crystal calibration surface-fit equations	
3.4	Heat Transfer Measurement System	52
3.4.1	Selection of the heat transfer measurement technique	
3.4.2	Analysis of wall transient technique	
3.4.3	Preparation of the test specimen	
3.4.4	Experimental set-up and recording procedure	
3.5	Summary of Chapter	67
Chapter 4	Numerical Investigation	68
4.1	The Governing Equations of Motion	68
4.2	Closure of the Averaged Equations	69
4.3	The Energy Equation	70
4.4	The Near Wall Function	71
4.5	Numerical Solution Procedure	72
4.6	The Grid Dependency	73
4.7	Initial and Boundary Conditions	76

4.8	Convergence	76
4.9	Summary of Chapter	77
Chapter 5	Presentation and Discussion of Experimental and Numerical Results	78
5.1	Introduction	78
5.2	Slot Nozzle Measurements	78
	5.2.1 Slot nozzle contraction design	
	5.2.2 Flow characteristics at the slot nozzle exit	
5.3	Heat Transfer Results	81
	5.3.1 Liquid crystal thermographic images	
	5.3.2 Heat transfer characteristics at the stagnation point	
	5.3.2.1 Effect of Reynolds number	
	5.3.2.2 Effect of slot jet-to-impingement surface separation distance	
	5.3.3 Heat transfer characteristics along the semi-cylindrical convex surface	
	5.3.3.1 Effect of Reynolds number	
	5.3.3.2 Effect of slot jet-to-impingement surface separation distance	
	5.3.4 Comparison with the average Nusselt number on the semi-cylindrical convex surface and flat surface	
5.4	Comparison with the Numerical and Experimental Heat Transfer Results	98
5.5	Summary of Chapter	101
Chapter 6	Summary of Conclusions and Recommendations	106
6.1	Summary of Conclusions	106
	6.1.1 Experimental results	
	6.1.2 Numerical results	
6.2	Qualitative and Quantitative Experimental Results	107

6.3	Numerical Results	111
6.4	Practical Applications of the Results	112
6.5	Recommendations for Further Work	112
References	114
Bibliography	125
Appendices	127
Publications	175

APPLICATION OF LIQUID CRYSTAL THERMOGRAPHY
IN
HEAT TRANSFER CHARACTERISTICS OF SLOT JET IMPINGEMENT

by
Tat Leung Chan

ABSTRACT

A fully automatic non-intrusive liquid crystal thermographic system, based on colour image processing and a transient wall heating technique, has been developed to obtain the surface heat transfer characteristics of a heated slot jet impinging on a semi-cylindrical convex surface. A novel calibration procedure for thermochromic liquid crystals has been developed which allows the technique to be applied with confidence to oblique surfaces for the first time. The parametric effects of jet Reynolds number (Re_w) ranging from 5,600 to 13,200 and the slot jet to impingement surface spacing (Y/W) ranges from 2 to 10 have been studied. Velocity and turbulence measurements of the slot jet exit were determined using hot wire anemometry.

High momentum directly below the jet leads to maximum heat transfer levels at the stagnation point. The flow rapidly decelerates and then begins to accelerate as it is deflected through 90 degrees and a wall jet begins to form. Local Nusselt numbers Nu_s decrease with increasing circumferential distance S/W from its maximum value at the stagnation point up to $S/W = 3.1$. The transition in the wall jet from laminar to turbulent flow was completed by about $3.3 \leq S/W \leq 4.2$ which coincided with a secondary peak in heat transfer. The stagnation Nusselt number Nu_0 shows good agreement with $Nu_0 \propto Re_w^{0.5}$ for laminar boundary-layer flow for $Y/W = 2$ to 6 in this study. For the larger spacings $Y/W \geq 8$, which are beyond the potential core, the jet Reynolds number dependence is stronger ($Nu_0 \propto Re_w^{0.54}$), and air entrainment effects on the jet momentum take place in this region. The local circumferential Nusselt numbers increase with increasing Reynolds numbers and the Nu_0 was shown to increase non-linearly to its peak values at the end of the potential core, $Y/W = 8$.

The rate of decay of average circumferential Nusselt numbers along the cylindrical convex surface is much faster than that which occurs laterally along the flat surface. New correlations of local and average Nusselt numbers with Re_w , Y/W and S/W have been established for the stagnation point and the circumferential distribution. As Y/W increases, the effect of curvature becomes apparent and the difference between the flat surface correlation and the convex surface becomes more pronounced. These provide previously unavailable guidelines for industrialists exploiting jet impingement for optimum heating/cooling applications.

The suitability of the widely used $k-\epsilon$ turbulence model, within the commercial code PHOENICS, has been assessed for predicting this flow. In the stagnation region, Nu_0 was overpredicted by up to 190%. Performance of the model improved in the wall jet region and with careful selection of the near wall cell size, which is crucial to ensure correct implementation of wall functions, Nu_s was predicted to within 29%.

Acknowledgements

I would like to express my sincere thanks to my Director of Studies, Dr. Nath Jambunathan, for all his guidance, enthusiasm, encouragement and confidence in me throughout the course of this work. His technical foresight perceived the need for such jet impingement on curved surface research work. I am also indebted to Dr. Shirley Ashforth-Frost, my second supervisor, for her helpful suggestions on the experimental work and advice concerning the proper use of thermochromic liquid crystals and numerical work, as well as to Prof. Tin Pui Leung, my local supervisor at The Hong Kong Polytechnic University for his useful discussions and constant support. Without their assistance and support, it would not have been possible for this thesis to be completed. I hope that I could share with my students what they have taught me.

Thanks are due to Mrs. Doreen Corlett for maintaining up-to-date jet impingement and liquid crystal databases. In addition, I take this opportunity to extend my sincere appreciation to anyone who have helped to make this thesis possible, especially to my senior colleague in Thermofluids Group, Dr. C. W. Leung for sharing his research experience to me.

I would also like to acknowledge the Department of Mechanical Engineering and the Staff Development Committee of The Hong Kong Polytechnic University, and also the British Council for financial support to this research to a certain extent. I also would like to express my gratitude to Prof. Ronald M. C. So, Chair and Head, Mr. Mike J. Pomfret, Former Head and Dr. C. Y. Chu, Former Principal Lecturer of my Department of Mechanical Engineering for their continued support.

I appreciate very much my wife, Susanna for all her love, understanding, encouragement and endurance during the past six years it has taken to complete this thesis, and my mother for her endless love in my life. Finally I want to dedicate this work to the memory of my father. He has enlightened me the importance of education from my very early age.

List of Publications

Chan T. L., Jambunathan K., Leung T. P. & Ashforth-Frost S., 1994. A Surface Temperature Calibration Method for the Thermochromic Liquid Crystals using True-colour Image Processing, *Proc. of the 10th Int. Heat Transfer Conference*. 14-18 August 1994, Brighton, UK.

Chan T. L., Leung T. P., Jambunathan K. & Ashforth-Frost S., 1995. Calibration of Thermochromic Liquid Crystals Applied to an Oblique Surface, *IMechE Conference Transaction of the 4th UK National Conference on Heat Transfer*, 26-27 September 1995, Manchester, UK.

Chan T. L., 1997. Liquid Crystal Thermography of Heat Transfer Distribution on a Flat Plate in a Turbulent Impinging Circular Jet, *Int. Symposium on Heat Transfer Enhancement and Energy Conservation (ISHTEEC'97)*, 16-19 June 1997, Guangzhou, China.

List of Figures and Tables

Figure:

- 1.1 Slot jet impingement geometry investigated.
- 2.1a Flow regions for a slot impinging free jet.
- 2.1b Flow regions of a free slot jet.
- 3.1 Schematic diagram of air nozzle jet system.
- 3.2 Schematic diagram of the slot nozzle and settling chamber.
- 3.3 Photograph of the slot nozzle and settling chamber.
- 3.4 Comparison of circular jet exit profile with the empirical profile of Schlichting (1979).
- 3.5a, b, c & d Micro-scope photographs of the liquid crystal (R30C5W).
- 3.6 Schematic diagram of a colour image processing system.
- 3.7 Format of a RGB colour system.
- 3.8 Format of a HIS (Hue, Saturation & Intensity) colour system.
- 3.9 Schematic diagram of calibration apparatus layout.
- 3.10 Photograph of liquid crystal colour spectrum along the heat conducting surface.
- 3.11a & b Flow chart of the calibration program.
- 3.12a Thermochromic liquid crystal (R30C5W) calibration surface-fit curve.
- 3.12b Thermochromic liquid crystal (R35C5W) calibration surface-fit curve.
- 3.13 Effect of viewing angle on the temperature versus hue characteristics of thermochromic liquid crystals (R30C5W).
- 3.14a & b Flow chart of the transient program.

- 3.15a & b Equation flow chart of the transient program.
- 3.16 Experimental set-up for the heat transfer investigation.
- 3.17 Schematic diagram of slot jet experiment.
- 3.18 Schematic diagram of the arrangement of video camera set up.
- 3.19a & b Liquid crystal (R30C5W) thermographs of a heated air slot jet impinging on the cylindrical convex surface, $Y/W=5$ and $Re_w=8,500$.
- 3.19c & d Liquid crystal (R35C5W) thermographs of a heated air slot jet impinging on the cylindrical convex surface, $Y/W=5$ and $Re_w=8,500$.
- 4.1 Typical schematic diagram of 27×55 grid system used for $Y/W=2$ computation.
- 4.2 Grid dependency performance tests at $S/W=0.1071$ and 0.5357 .
- 4.3 Grid dependency performance tests at the axial and azimuthal velocities.
- 4.4 Near wall turbulent kinetic energy for different grid systems.
- 5.1a Velocity and streamwise turbulence intensity profiles across the slot nozzle width, $Re_w=5,600$.
- 5.1b Velocity and streamwise turbulence intensity profiles across the slot nozzle width, $Re_w=8,500$.
- 5.1c Velocity and streamwise turbulence intensity profiles across the slot nozzle width, $Re_w=13,200$.
- 5.2a Thermal investigation of a heated air slot jet impinging on a semi-cylinder convex surface, $Re_w=5,600$.
- 5.2b Thermal investigation of a heated air slot jet impinging on a semi-cylinder convex surface, $Re_w=8,500$.

- 5.2c Thermal investigation of a heated air slot jet impinging on a semi-cylinder convex surface, $Re_w = 13,200$.
- 5.3 Effect of Reynolds number on the stagnation point Nusselt number.
- 5.4 Effect of slot jet-to-impingement surface separation distance.
- 5.5 Comparison of the stagnation Nusselt number between present data for a semi-cylinder convex surface and the published correlations for the convex surfaces and flat plate.
- 5.6a Circumferential Nusselt number distribution for different Re_w on the impingement surface at $Y/W = 2$.
- 5.6b Circumferential Nusselt number distribution for different Re_w on the impingement surface at $Y/W = 4$.
- 5.6c Circumferential Nusselt number distribution for different Re_w on the impingement surface at $Y/W = 6$.
- 5.6d Circumferential Nusselt number distribution for different Re_w on the impingement surface at $Y/W = 8$.
- 5.6e Circumferential Nusselt number distribution for different Re_w on the impingement surface at $Y/W = 10$.
- 5.7a Circumferential Nusselt number distributions for different Y/W on the impingement surface at $Re_w = 5,600$.
- 5.7b Circumferential Nusselt number distributions for different Y/W on the impingement surface at $Re_w = 8,500$.
- 5.7c Circumferential Nusselt number distributions for different Y/W on the impingement surface at $Re_w = 13,200$.
- 5.8a Comparison of average Nusselt number calculated using correlations for the semi-cylindrical convex surface and the published correlations for the flat surface at $Y/W = 4$.

- 5.8b Comparison of average Nusselt number calculated using correlations for the semi-cylindrical convex surface and the published correlations for the flat surface at $Y/W=8$.
- 5.9a Circumferential Nusselt number distribution, $Re_w=5,600$ & $Y/W=4$.
- 5.9b Circumferential Nusselt number distribution, $Re_w=5,600$ & $Y/W=8$.
- 5.9c Circumferential Nusselt number distribution, $Re_w=13,200$ & $Y/W=4$.
- 5.9d Circumferential Nusselt number distribution, $Re_w=13,200$ & $Y/W=8$.
- A.1 Schematic diagram of the slot nozzle contraction in horizontal direction.
- A.2 Schematic diagram at the slot nozzle contraction in vertical direction.
- D.1 The geometry of video camera viewing angle on the target surface.
- D.2 Schematic diagram of the representation of video camera viewing angle on the semi-cylinder specimen, $R=75$ mm.

Table:

- 1.1 Experimental parameters.
- 4.1 Constants used in the $k-\epsilon$ turbulence model.
- 4.2 Percentage error associated with near wall cell sizes (ranging from $S/W=0.1071$ to $S/W=0.5357$).
- 5.1 Flow parameters of a single heated air impinging slot jet.

List of Appendices

- Appendix A** Profile coordinates of slot nozzle contraction
- Appendix B** Thermochromic liquid crystal calibration and transient program
- B.1 Calibration program commands user menu in screen format
- B.2 Transient program commands user menu in screen format
- Appendix C** Data reduction equation and propagation of uncertainty for the determination of heat transfer coefficient
- Appendix D** CCD video camera viewing angle analysis in slot jet experiment
- Appendix E** A typical PHOENICS data input file, Q1 and GROUND.for coding for computing the heat transfer and flow characteristics on a semi-cylindrical convex surface due to an impinging slot jet
- E.1 Q1. file
- E.2 Extract from GROUND.for for computing the heat transfer and flow information

Nomenclature

b	Thickness of jet
Bi	Biot number, $\frac{hL}{k}$
CCD	Charge-Coupled Device
c_p	Specific heat at constant pressure
C_{μ}, C_1, C_2	Turbulence model constants
d	Circular nozzle diameter
D	Diameter of impingement cylinder
D_{AB}	Binary diffusion coefficient
erf	Gaussian error function
E	Offset
Eff	Effectiveness
$E(\lambda)$	Lighting spectral distribution
Fr	Froessling number, $\frac{Nu}{\sqrt{Re}}$
g	Gravitational acceleration
G	Mass velocity at nozzle exit
Gr	Grashof number, $\frac{g\beta(T_w - T_{\infty})L^3}{\nu^2}$
h	Local heat transfer coefficient or mass transfer coefficient
h_{ave}	Average heat transfer coefficient
h_p	Enthalpy at near wall node
h_w	Enthalpy at wall
HSI/H,S,I	Hue, Saturation, Intensity
k	Thermal conductivity of acrylic specimen; turbulent kinetic energy
L	Characteristic length scale
m,n	Positive integer

Nu	Nusselt number, $\frac{hL}{k}$
Nu_s	Local Nusselt number in circumferential distance, $\frac{hw}{k}$
Nu_{ave}	Averaged Nusselt number
Nu_0	Stagnation Nusselt number
p, P	Pressure
PAL	Phase Alternation Line
Pr	Prandtl number, $\frac{\mu c_p}{k}$
r	Horizontal (radial) coordinate for axisymmetric flows
$r(\lambda)$, $b(\lambda)$, $g(\lambda)$	Red, green and blue filter functions
$R(\lambda)$, $B(\lambda)$, $G(\lambda)$	Red, green and blue surface reflectance
R	Radius of cylinder, cylindrical, and spherical targets; radius of curvature of jet centre line
R30C5W	Red start 30 °C, blue start 35 °C; the other colour exhibit between this 5 °C bandwidths
R35C5W	Red start 35 °C, blue start 40 °C; the other colour exhibit between this 5 °C bandwidths
Re	Reynolds number, $\frac{UL}{\nu}$
Re_a	Arrival velocity or maximum velocity of a free jet at place of apparent front stagnation point of cylinder
Re_d	Reynolds number of circular jet diameter at nozzle exit
Re_D	Reynolds number of cylinder diameter
Re_{2w}	Reynolds number of double slot jet width at nozzle exit
Re_w , Re_w	Reynolds number of slot jet width at nozzle exit
Re_m	Plate Reynolds number for curved surfaces
R, G, B/RGB	Red, Green and Blue primaries in the PAL colour system
S	Circumferential distance along cylinder surface from the centerline of a slot jet

Sc	Schmidt number, $\frac{\nu}{D_{AB}}$
Sh	Sherwood number, $\frac{h_D D}{\beta}$
Sh_{ave}	Average Sherwood number
Sh_{max}	Maximum Sherwood number
Sh_0	Sherwood number at stagnation point
St	Stanton number, $\frac{h}{\rho U c_p}$
St_{ave}	Average Stanton number
t	Time
T	Temperature
T_j	Mean jet exit temperature
T_{amb}	Initial wall (ambient) temperature
$T_{(0,t)}$	Local wall temperature at specific time, t
T_p	Temperature at near wall node
T_w	Temperature at wall
T_∞	Free-stream temperature
Tu	Overall turbulence intensity at nozzle exit
u	Instantaneous velocity in x-direction
v	Instantaneous velocity in y-direction
v_p	Azimuthal velocity at near wall node
u'	Fluctuating velocity in x-direction
v'	Fluctuating velocity in y-direction
$\overline{u'v'}$	Component of Reynolds shear stress
U	Mean velocity in x-direction
V	Mean velocity in y-direction
w/W	Slot nozzle width
x,y,z	Spatial coordinates

y	Thickness of acrylic specimen
y_p	Distance from the impingement surface wall to the near wall node
y^+	Non-dimensional distance from the impingement surface wall
X	Distance from the centerline of slot nozzle jet
Y	Slot/circular jet-to-impingement surface separation distance
YUV/Y,U,V	PAL transmission system: Y - luminance U,V - chrominances

Subscripts

d	Circular nozzle diameter
D	Impingement cylinder diameter
W	Slot nozzle width
$2W$	Double slot nozzle width

Greek letters

α	Thermal diffusivity
β	Coefficient of thermal expansion, $\frac{1}{T_\infty}$ or Diffusion coefficient
δ_{ij}	Kronecka delta
ε	Dissipation rate of turbulent kinetic energy
κ	von Karman constant
μ	Dynamic viscosity
ν	Kinematic viscosity
μ_t	Turbulent kinematic viscosity
π	Pi
θ	Angular/streamwise coordinate measured from stagnation point
ρ	Density
ρ_a	Density of air at nozzle exit
ρ_s	Density of acrylic specimen

σ_l	Laminar Prandtl number
σ_t	Turbulent Prandtl number
$\sigma_k, \sigma_\epsilon$	Turbulence model constants

Chapter 1 Introduction

This Chapter provides an engineering insight into the importance of jet impingement heat transfer processes and the usefulness of their numerical solution. The explanation and background to the work and identification of research needs to enable further development of jet impingement heat transfer processes and numerical models will be addressed. The rationale and specific aims of the research are presented in a systematic manner together with a set of objectives formulated to achieve these aims. Finally, a brief description of the Chapters in the thesis is given.

1.1 Background and Description of the Problem

Jet impingement heat transfer is commonly encountered in many engineering applications and manufacturing processes because of its excellent heat and mass transfer characteristics, low cost and simple control. Impinging jets provide a means of obtaining high heat transfer coefficients and of localising such transfer coefficients at specific zones on the impingement surface. Another important consequence of jet impingement is that the non-uniform distribution of the heat transfer coefficient can lead to unwanted overheating due to hotspots. Because of these characteristics, the impingement technique is widely used in heating, cooling and drying operations. Detailed knowledge of the heat transfer mechanisms involved in jet impingement is therefore essential when establishing design criteria for optimal jet arrangement. There are many parameters that influence heat transfer and flow characteristics between the impinging jet(s) and impingement surface. These parameters include turbulence, exit jet velocity profiles (i.e. a parabolic or a flat velocity profile), Reynolds number, unconfined and confined jet configurations, nozzle geometry, jet exit temperature, jet-to-impingement surface separation distance, entrainment, angle of incidence, the offset from the stagnation line, impingement surface shape, external factors (i.e. controlled excitation and swirl jet), multiple jets, jet arrays and cross flow. However, the range of physical parameters and boundary conditions are widespread mainly due to the limitations of measurement methods. Jet impingement onto orthogonal surfaces has received much attention, however, there is paucity information on jet impingement

onto oblique/curved surfaces. Many industrial applications include for example, the heating, cooling and/or drying of painted cylinders, glass, paper, textiles, film material, foodstuffs, age hardening, the de-icing of aircraft wings and safety requirements in the storage of cylinders containing liquefied gas. The optimisation of such applications is becoming necessary as industry demands increased efficiency and safety. There is a wide range of jet impingement configurations encountered in practice. Here, attention is focused on heat transfer characteristics of a turbulent hot air impinging slot jet on a semi-cylinder convex surface. Thus a thorough experimental investigation of the heat transfer mechanism will be used to provide both practical data for engineers and reliable experimental information which is required to validate the theoretical heat transfer models and the numerical procedures using mathematical models of turbulence.

The emergence of commercial Computational Fluid Dynamics (CFD) codes has enabled industrial community to model more complex flow geometries without the need to set-up high quality and costly experimental facility. However, there are still major problems with the closure of the turbulence models in which reliable prediction of the flow-field or heat transfer characteristics of all test parameters is still questionable. Hence, work is continually on-going to improve the validation of turbulence models in CFD community. The performance of the widely used kapp-epsilon ($k-\epsilon$) turbulence model will be assessed for the prediction of the outcome of the experimental investigation.

1.2 Aims and Objectives

1.2.1 Specific aims

- i) To develop an automatic colour image processing of liquid crystal thermography for accurate heat transfer measurements in jet impingement on oblique/complex surface.
- ii) To obtain a better understanding of the influences of jet Reynolds number and slot jet-to-impingement surface separation distance on the local and

average heat transfer characteristics from a turbulent slot jet on a semi-cylinder convex surface.

- iii) To provide a benchmark for the future development of numerical solutions and turbulence models.
- iv) To assess the suitability of the standard k - ϵ turbulence model in predicting heat transfer characteristics of a turbulent slot jet impingement on a semi-cylinder convex surface.

1.2.2 Rationale

The experimental parameters used in the present study are listed in Table 1.1. Three jet Reynolds numbers Re_w were chosen to provide a broad circumferential distribution ($0 \leq S/W \leq 13.6$) of local and average heat transfer characteristics on a cylindrical convex surface and to ensure a suitable flow range to allow comparisons to be made with the existing literatures. Five dimensionless slot jet-to-impingement surface separation distance Y/W , ranging from 2 to 10 were considered to include the occurrence of the maximum Nusselt number in the stagnation region. This dimensionless separation distance Y/W range are often quoted for design purposes, based on an impinging slot nozzle jet, Gardon and Akfirat (1966), and Gau and Chung (1991).

Parameters	Range
Re_w	5,600 to 13,200
Y/W	2 to 10
S/W	0 to 13.6

Table 1.1 Experimental Parameters

Figure 1.1 shows schematically the experimental geometry considered together with the nomenclature and coordinates. Despite the industrial relevance of this slot jet geometry, very limited works were identified in the existing literature concerning impingement on a convex surface. In addition, the k - ϵ turbulence model was selected for assessment in this study because of its wide use and availability in industry and academia.

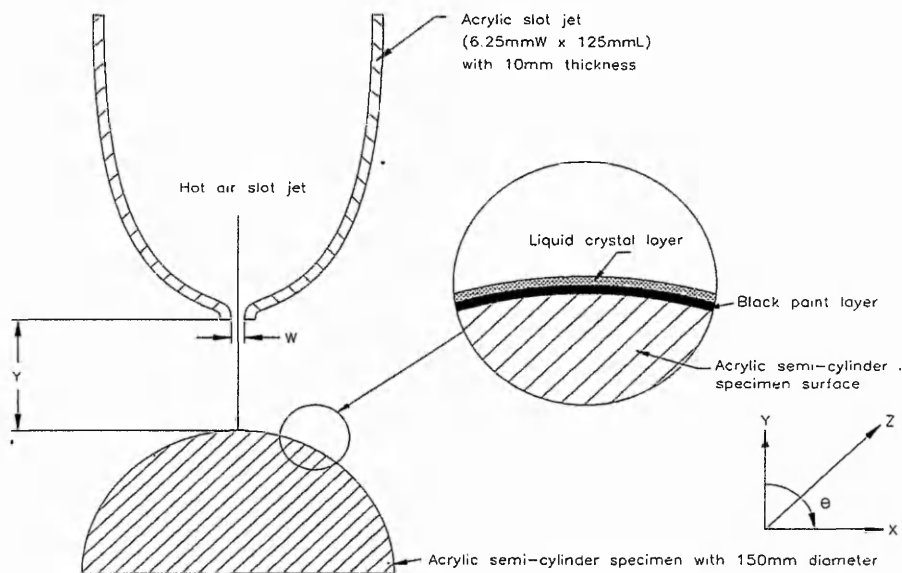


Figure 1.1 Slot jet impingement geometry investigated

1.2.3 Objectives

A set of target objectives were discerned to allow accomplishment of the specific research aims:

- i) Design, build, commission and validate an airflow jet rig to provide the steady airflow required for the investigation. Establish a hot-wire anemometry with associated instrumentation and traverse control system to obtain exit jet characteristics and accurately position the measuring device within jet flow. Develop an automatic colour image processing of liquid crystal thermography for heat transfer measurements in jet impingement on oblique/complex surface. Calibrate the thermochromic liquid crystals in terms of temperature, hue (colour) and camera viewing angle on the oblique/curved surface and interpret the surface heat transfer information from captured liquid crystal images. Caution is required for the experimental planning, debugging and execution of experiments, data analysis and interpretation, and experimental uncertainty analysis.

- ii) Complete a thorough literature review to identify the need of further study on the type of jet impingement surface and experimental parameters.
- iii) Identify the factors that affect the measurement techniques and equipment selection for surface heat transfer and exit jet characteristics studies such as experimental uncertainty, availability, cost, suitability and consistency. Validate the experimental techniques chosen by comparing results with previously published data.
- iv) Obtain the exit jet velocity and turbulence profiles, and surface heat transfer measurements for the test programme. Ensure the repeatability of experimental data.
- v) Apply an existing Computational Fluid Dynamics (CFD) commercial package using the standard k - ϵ turbulence model, with input of measured and defined boundary conditions, predict the heat transfer characteristics on impingement surface. Compare the numerical results with existing experimental data.

1.2.4 Breakdown of objectives

Quality of results

What is the uncertainty in the measured physical properties after data reduction?

What is the calibration error? What is the spatial resolution of hot-wire traversing mechanism system? Why was hot wire anemometry system used?

How does data output vary with signal conditioning and number of data samples? Should steady state or transient liquid crystal method be used to evaluate the convective heat transfer information? How does the effect of camera viewing angle on surface temperature respond to thermochromic liquid crystals? What is the spatial resolution of temperature measurements? What is the temporal resolution? What is the thermal resolution? What is the overall uncertainty?

What is the uncertainty in the airflow jet system? Is the jet two-dimensional? Outlet conditions and characteristics? Are the experimental results repeatable?

Analysis of Results

Is the flow incompressible? What are the V , v , and v' profiles along the slot nozzle width?

Where do the maximum heat transfer coefficients occur? How does the heat transfer distribution vary with the dimensionless circumferential distance, S/W , slot jet-to-impingement surface separation distance, Y/W and Reynolds number, Re ? How are the data to be correlated for design purpose?

Does transition of laminar to turbulent flow take place? At what Y/W and S/W position? Do these relate to Nusselt number profiles? Do the heat transfer profiles correlate/agree with previous work?

How well does the k - ϵ turbulence model predict the surface heat transfer distribution? Can recommendations for future work be proposed?

These questions will be addressed through the course of the work and within the text of this thesis.

1.3 Outline of the investigation

This Chapter has introduced a brief background and the statement of the problem with a clear description of the aims and objectives to achieve the programme of work.

Comprehensive review of relevant literature is detailed in Chapter 2. The review commences with a description of flow regions for a slot impinging jet on convex cylindrical surface, and the Nusselt number and Sherwood number correlations obtained for the curved surfaces. The effect of turbulence on stagnation point/streamwise local heat transfer and surface curvature on local/average heat

transfer and the dependence of Nusselt number on Reynolds number are discussed. The review of literature on the numerical prediction of slot jet impingement has also been focused on recent and relevant works.

The design, development and validation of the experimental rigs, the procedures and the measuring technique adopted for hot-wire anemometry system, liquid crystal calibration system and automatic non-intrusive liquid crystal thermography for surface heat transfer measurement system based on colour image processing system are presented in Chapter 3.

The governing equations for flow and heat transfer, and their numerical solution, are presented in Chapter 4. The numerical grid dependence accuracy and convergence criteria are also discussed. However, the solution algorithm and well-known commercial package PHOENICS (Parabolic, Hyperbolic or Elliptic Numerical Investigation Code Series) are briefly described since the details are available in several texts.

The presentation and discussion of all experimental and numerical results are given in Chapter 5 as well as their comparison. This chapter focuses on the heat transfer characteristics of a heated slot jet impinging on a semi-cylindrical convex surface. A comprehensive set of results for all experimental parameters are given. The parametric effects of jet Reynolds number ranges from 5,600 to 13,200 and the slot jet-to-impingement spacing ranges from 2 to 10 are presented. Correlations of local and average Nusselt numbers with the jet Reynolds number, the slot jet-to-impingement surface spacing and circumferential distance are also established.

Finally, conclusions drawn from this study, practical applications of the results and recommendations for further work are discussed in Chapter 6.

Chapter 2 Literature Review

2.1 Introduction

Jet impingement heat transfer has received considerable attention both in experimental and numerical works due to its high local heat transfer rates for heating, cooling, or drying a surface. The majority of research attention has concentrated on the impingement of unconfined axisymmetric (circular) and slot (two-dimensional) jets on a flat surface. Slot jets impingement heat transfer for curved surfaces, both the peak and the spatial heat transfer distribution, have received less attention although the importance of materials processing and other applications is popular. In this chapter, however, the literature review will mainly focus on previous heat transfer impingement on curved (convex) surfaces. In Section 2.1.1, a comprehensive sources of the literature reviews on impingement heat and mass transfer under jet configurations are available. In Section 2.1.2, a discussion of flow characteristics of single slot jet impinging on convex cylindrical surface is given. Although there are extensive literature on the heat transfer characteristics of single jet impinging on flat surfaces/plates, little is known about those on convex surface. The few studies dealing with the heat transfer distribution on convex cylindrical surface under a single impinging jet or free stream are briefly discussed in Section 2.2.

2.1.1 Previous review of literature

A number of literature review on impinging jets have been published. They include bibliographical form such as Button and Wilcok (1978), Button and Jambunathan (1989), and Jambunathan and Button (1994), critical review on various aspects of the experimental, analytical and numerical work such as Arganbright and Resch (1971), Mujumdar and Douglas (1972), Livingood and Hrycak (1973), Becko (1976), Martin (1977), Hrycak (1981), Downs and James (1987), Polat et al. (1989), Launder (1991), Jambunathan et al. (1992), Viskanta (1993).

2.1.2 Flow regions description

A typical slot impinging jet on a convex cylindrical surface is shown schematically in Figure 2.1a. The slot nozzle geometric arrangement is characterized by the nozzle width, W , and the separation of slot nozzle and the target surface, Y . Nearly uniform jet exit velocity and temperature with some level of turbulence are used.

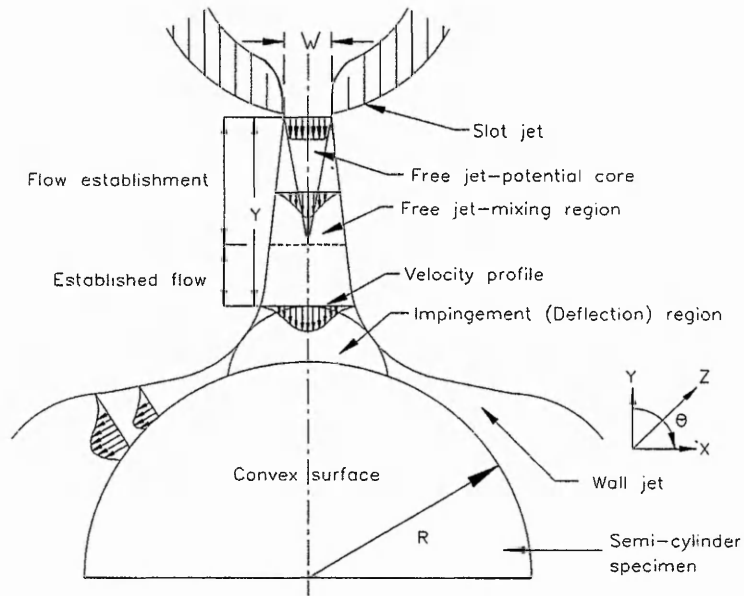


Figure 2.1a Flow regions for a slot impinging free jet.

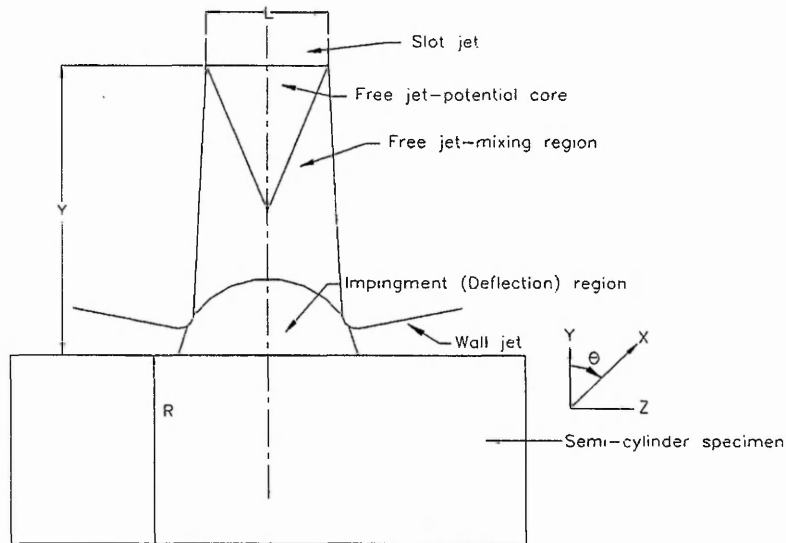


Figure 2.1b Flow regions of a free slot jet.

The characteristic of the flow structure of impinging slot jet on a semi-cylinder can be subdivided into three distinctive regions: the free jet region, the impingement (deflection) flow region, and the wall jet region as shown in Figure 2.1b.

According to the description of Viskanta (1993), the free jet region, shear-driven interaction of the exiting jet and the ambient produces entrainment of mass, momentum, and energy. These combined effects introduce the development of a non-uniform radial velocity profile, expansion of the jet, an increase of total mass flow rate, and modification of the jet temperature before it impinges upon the target surface. The impingement zone is characterised by a deflection region and the turning of the jet fluid in the circumferential and axial directions, which affects the wall jet transition further downstream. In here, the wall jet region is characterised by a bulk fluid flow in the outward cylindrical direction. The free jet region can be further subdivided into flow establishment and established flow zones. In the flow establishment zone, the velocity remains constant in the potential core and equals to the nozzle exit velocity. Whereas, the length of the potential core is strongly dependent on the turbulence intensity of nozzle exit and its initial velocity profile. Livingood and Hrycak (1973) reported that the potential core extended 4.7-7.7 slot width, W , from the nozzle exit for a slot jet. The established flow zone was characterised by the decay of the axial velocity profile caused by large shear stresses at the jet boundary. Due to these large shear stress effects, turbulence and the entrainment of additional fluid were promoted and generated. After the established flow zone, the velocity profile was considered fully developed.

2.2 Experimental Heat/Mass Transfer Characteristics of an Impinging Slot/Circular Jet

2.2.1 Nusselt Sherwood number correlations

Waltz and London (1964) summarized the previous researchers' analytical and experimental work on the stagnation point and average heat transfer coefficients for an axially symmetrical infinite stream flow or jet flow over spheres and circular cylinders. It was found that the circular jet impinging on the sphere gave the highest average

Stanton number. Next followed the slot jet impinging on the cylinder, then the flat rectangular plate, and the lowest was the circular jet impinging on the flat circular plate. Typical experimental correlations for a small stream as produced by a circular jet flow over a spherical target and a slot jet flow over a cylindrical target were expressed as follows:

For a spherical target in the range of $Y/d=1$, $1 \leq R/d \leq 2$ and $4 \times 10^4 \leq Re_{\pi r} \leq 2 \times 10^5$;

$$Nu_0 = 1.26 Pr^{0.33} Re_{\pi r}^{0.5} ; \quad (2.1)$$

$$St_0 = 1.26 Pr^{-0.67} Re_{\pi r}^{-0.5} \quad \text{and} \quad (2.2)$$

$$St_{nve} = 1.41 Pr^{-0.6} Re_{\pi r}^{-0.5} \quad (2.3)$$

For cylindrical target in the range of $4 \leq Y/d \leq 16$, $125 \leq R/W \leq 15$ and $2 \times 10^4 \leq Re_{\pi r} \leq 2 \times 10^5$;

$$St_0 = 1.16 Pr^{-0.6} Re_{\pi r}^{-0.5} \quad \text{and} \quad (2.4)$$

$$St_{nve} = 1.21 Pr^{-0.6} Re_{\pi r}^{-0.5} \quad (2.5)$$

Gardon and Akfirat (1966) investigated the local and average heat transfer coefficients of impinging two-dimensional air jets on an isothermal flat plate for both single jets and arrays of jets. They concluded that the local Nusselt numbers at stagnation point depended on the Reynolds number only for $Re_w < 2,000$. The Nusselt number at stagnation point for a single two-dimensional jet were correlated as follows:

$$Nu_0 = 1.2 Re_w^{0.55} \left(\frac{Y}{W} \right)^{-0.62} \quad \text{for} \quad 50,000 \leq Re_w \leq 2000, 14 \leq Y/W \leq 60, 0.6\% \leq Tu \leq 7.5\% \\ \text{and } 1.6 \text{ mm} \leq W \leq 6.4 \text{ mm} \quad (2.6)$$

As $Y/W < 0.5$, the impinging jet became a wall jet and the heat transfer coefficients increased rapidly with increasing velocities in the gap between the nozzle exit and the plate. In this regime, two peaks of heat transfer rate were observed from the stagnation line. For $Y/W < 8$, two humps began to form at about $Y/W = 7$, and, for $Y/W < 6$, they became well-defined secondary peaks in the heat transfer rate. They explained that these secondary peaks were ascribed to a transition from laminar to turbulent boundary

layers along the plate. For $8 < Y/W < 14$, the lateral variation of heat transfer coefficients began to form a bell shape. For $Y/W > 14$, the lateral variation of heat transfer coefficients became well-defined bell shape.

Gostkowski et al. (1970) investigated the effect of free stream turbulence on the heat transfer to the stagnation point of a sphere. It was found that the increase of Nusselt number at stagnation point was dependent mainly on the Reynolds number and the turbulence intensity whereas the effects of the scale of the turbulence were not discernible. The value of $Nu/Re^{0.5}$ was increased slightly in the lower turbulent Reynolds number, TuRe range but it was increased significantly when the turbulent Reynolds number was greater than 7×10^3 . Correlations of Nu_0 were obtained as follows:

$$\frac{Nu_0}{Re^{0.5}} = 1.255(TuRe)^{0.0214} \quad \text{for } TuRe < 7 \times 10^3 \quad (2.7)$$

$$\frac{Nu_0}{Re^{0.5}} = 1.255(TuRe)^{0.2838} \quad \text{for } TuRe > 7 \times 10^3$$

Kumada et al. (1973) investigated the local and mean mass transfer on a cylinder in the potential core and developed (transition) region of a slot jet. They concluded that the flow pattern around a cylinder in potential core region of a slot jet differed greatly from that in a uniform flow. The front stagnation region was narrow and the pressure gradient was large. The occurrence of separation was delayed by the Coanda effect and a circular wall jet type flow was formed along the cylinder. The separation region was small and no periodic vortex shedding (the van Karman street vortex) could be observed. Sherwood number at the front stagnation point could be treated as a uniform flow case. Minimum Sherwood number took place at $S/W \cong 2 \sim 2.5$ which was independent of D/W or Re_p . The second maximum peak of Sherwood number appeared at the transition to turbulent flow and its position was somewhat downstream from the end of acceleration region. The dependency of the Reynolds number for the mean Sherwood number was explained by correspondence to the local Sherwood profiles. The mean Sherwood number produced by the slot jet was 30% to 40% higher than in uniform flow with negligible intensity of turbulence, but was almost equal to

that for turbulence of uniform flow stream (turbulence intensity, 2%~6%). The pressure gradient near the stagnation point was affected strongly by D/W and its effect remained large in the developed region. The base pressure was nearly constant (C_p) and independent of D/W , and even in the developed region, but it was smaller than that created when a cylinder was placed in a uniform flow stream with turbulence. Again, no periodic vortex shedding could be identified. The local Sherwood number distribution due to a slot jet impinging normally on a cylinder differed remarkably from that in uniform flow and was strongly affected by the Coanda effect as a cylinder in shear flow. The experimental correlations obtained in the ranges of $4.3 \times 10^4 \leq Re_D \leq 2 \times 10^5$, $3.75 \leq D/W \leq 15$ and $2 \leq Y/W \leq 4$ were as follows:

$$Sh_0 = 1.19CRe_D^{0.5}Sc^{0.4} \quad \text{where} \quad C=1+0.037(D/W)^{1.21} \quad \text{for } 3 \leq D/W < 10 \quad (2.8)$$

$$C=1+0.102(D/W)^{0.77} \quad \text{for } 10 < D/W \leq 25$$

$$Sh_{\max} = 0.218(D/W)^{1/6}Re_D^{2/3} \quad (2.9)$$

$$Sh_{\text{ave}} = 0.49Re_D^{0.6}; \quad D/W=3.75 \quad (2.10)$$

$$= 0.369Re_D^{0.63}; \quad D/W=7.5$$

$$= 0.227Re_D^{2/3}; \quad D/W=15$$

Another experimental correlations which were arranged by Kumada et al. (1974) in the ranges of $4 \times 10^4 \leq Re_D \leq 2 \times 10^5$, $3 \leq D/W \leq 15$ and $6 \leq Y/W \leq 40$ were as follows:

$$Sh_0 = 0.74(1+0.75(Y/D)^{-0.57})(D/W)^{0.0934}Re_a^{0.58} \quad \text{for } 0.4 \leq Y/W \leq 12 \quad (2.11)$$

$$Sh_{\text{ave}} = 0.225(Y/W)^{0.34}Re_a^{0.63} \quad \text{for } 6 \leq Y/W \leq 8 \quad (2.12)$$

$$Sh_{\text{ave}} = 0.435Re_a^{0.63} \quad \text{for } 10 \leq Y/W \leq 40$$

Sparrow et al. (1984a) reported that the axial distribution of the heat transfer coefficient peaked at the circular jet impingement point on a cylinder. Three parameters systematically varied from the range of $0.189 \leq d/D \leq 0.424$, $5 \leq Y/d \leq 15$ and $4,000 \leq Re_d \leq 25,000$ respectively. The peak heat transfer coefficient increased as

the distance between the initiation of the jet and the cylinder surface decreased for a fixed jet diameter and Reynolds number. The drop-off of heat transfer coefficient with increasing axial distance from the impingement point was accentuated for smaller jet initiation distances (at a fixed jet diameter and Reynolds number) and for smaller jet diameters (at a fixed initiation distance and Reynolds number). The axial distributions of Sherwood number and Nusselt number were correlated as follows:

$$\frac{\text{Sh}}{\text{Re}_d^{0.765} e^{-1.62(d/D)}} = 0.775 \text{Re}_d^{-0.08}, \quad Y/d = 5 \quad (2.13)$$

$$\frac{\text{Sh}}{\text{Re}_d^{0.765} e^{-1.62(d/D)}} = 0.306, \quad Y/d = 10$$

$$\frac{\text{Sh}}{\text{Re}_d^{0.765} e^{-1.62(d/D)}} = 0.244, \quad Y/d = 15$$

$$\text{Nu} = 0.586 \text{Sh} \quad (2.14)$$

However, the circumferential distribution of the heat/mass transfer coefficient along the cylinder was not available in their investigation.

Gau and Chung (1991) studied the surface curvature effects on the different sizes of slot-air-jet impingement cooling flow structure and heat transfer along a concave/convex side of a heated semicylindrical surface. In this experiment, the jet Reynolds number, Re ranged from 6,000 to 350,000, the slot-to-plate spacing, Y/W from 2 to 16, and the surface diameter-to-slot-width ratio, D/W from 8 to 45.7. In the convex surface case, it was found that a series of three-dimensional counter rotating vortices along the surface could increase the momentum transport in the flow structure and enhance the heat transfer process on the wall near the stagnation point. The increasing of surface curvature could augment the size of the counter rotating vortices, which produced a higher Nu number at stagnation point. However, the heat transfer magnitude was reduced in the region away from the stagnation point where the flow became more stable due to the centrifugal force along the surface curvature. In the concave surface case, no three-dimensional vortices in the stagnation point were

observed. However, the local Nusselt number in the region away from the stagnation was increased with increasing of surface curvature due to the generation of Taylor-Gortler vortices along the surface. Correlations of Nu_0 at the stagnation were obtained for $6,000 \leq Re \leq 35,000$ and $8 \leq D/W \leq 45.7$ as follows:

For convex surface,

$$Nu_0 = 0.729 Re^{0.5} (D/W)^{-0.14} (Y/W)^{0.16} \quad \text{for } 2 \leq Y/W \leq 8 \quad (2.15)$$

$$Nu_{ave} = 0.221 Re^{0.65} (D/W)^{-0.33} (Y/W)^{0.1}$$

$$Nu_0 = 1.716 Re^{0.54} (D/W)^{-0.15} (Y/W)^{-0.38} \quad \text{for } 8 \leq Y/W \leq 16$$

$$Nu_{ave} = 0.308 Re^{0.65} (D/W)^{-0.38} (Y/W)^{0.2}$$

For concave surface,

$$Nu_{ave} = 0.251 Re^{0.68} (D/W)^{-0.38} (Y/W)^{0.15} \quad \text{for } 2 \leq Y/W \leq 8 \quad (2.16)$$

$$Nu_{ave} = 0.394 Re^{0.68} (D/W)^{-0.38} (Y/W)^{-0.32} \quad \text{for } 8 \leq Y/W \leq 16$$

Whitaker (1992) studied the heat transfer resulting from the impingement of a heated circular jet upon a cylinder. The cylindrical target for heat transfer studies was a hollow aluminum pipe having an outside diameter, D of 16.5 cm. It had a length of 1.8 m which was sufficient to eliminate any end effects. The nozzle exit diameters, d of 1.27, 1.75 and 2.54 cm were used and the nozzle Reynolds numbers ranged from 32,000 up to 160,000. Measurement locations at impingement distances of 7, 10, 12, 15, 18, 21 and 25 nozzle diameters were selected. The range of jet exit temperatures used in his study were 80°C, 135°C and 190°C. The effect of each parameter (i.e. nozzle Reynolds numbers, nozzle exit temperatures, nozzle diameters, and impingement distances) had on heat transfer characteristics was determined. He concluded that the range of nozzle exit temperatures used did not affect much on velocity profiles in the free jet and did not influence heat transfer behaviour. Nusselt numbers at the stagnation was found to be solely dependent on the nozzle Reynolds number and impingement distance. Results were also comparable to values obtained with flat plate targets for less than 12 nozzle diameters of impingement distances. The

flow and heat transfer behaviour near the stagnation point region ($S/d < 0.2$) was independent of target geometry for those impingement distances. Local Nusselt number distributions along the longitudinal axis of the cylinder were found to have similarity in the distributions on a flat plate target. Convex target curvature around the circumference of the cylinder enhanced the decay rate of local Nusselt numbers. This was attributed to convex curvature suppressing turbulent mixing. The Nusselt numbers around the circumference of the cylinder decayed faster than they did along the longitudinal axis. Increasing the impingement distance did not have much effect on it. The transition from a deflection region to a wall jet occurred at 2.5 to 3 nozzle diameters from the stagnation point around the circumference and 3 nozzle diameters along the longitudinal axis. These locations also corresponded to where the Nusselt numbers reached a constant minimum value. There was also a weak dependence upon the range of the jet nozzle diameter to target cylinder diameter ratio, d/D studied. Correlations for non-dimensional Nusselt number distribution along the longitudinal axis and around the circumferential axis were expressed as follows:

Along the longitudinal axis,

$$Nu/Nu_0 = 1.0 - 2.36(S/Y) + 2.41(S/Y)^2 - 0.89(S/Y)^3 \quad (2.17)$$

Around the circumferential axis,

$$Nu/Nu_0 = 1.01 - 3.15(S/Y) + 3.42(S/Y)^2 - 1.25(S/Y)^3 \quad (2.18)$$

The distribution of the average Nusselt numbers was given as follows:

$$Nu_{ave} = 0.62Re^{0.73}(Y/d)^{-0.69}(S/d)^{-0.46} \quad (2.19)$$

Recently, Lee et al. (1997) investigated the effects of the hemispherically convex surface curvature on the flow and heat transfer from a fully developed axisymmetric impinging jet. In this experiment, the jet Reynolds number, Re ranged from 11,000 to 50,000, the nozzle-to-surface distance, Y/d from 2 to 10, and the nozzle-diameter-to-surface curvature ratio, d/D from 0.034 to 0.089. The potential core of jet flow was found from 3.1 to 4.2 nozzle diameters for $Re = 11,000$ to 50,000. The Nusselt number

at the stagnation point, Nu_0 was increased with the increasing surface curvature (i.e. increasing value of d/D) and both Nu_0 and turbulent flow intensity along the free-jet centerline reached their maximum values at $Y/d \cong 6$ to 8 for the Re and d/D ranges studied. However, the effect of surface curvature on the heat transfer was found less in the wall jet region compared to its stagnation point region. The local Nusselt number was decreased monotonically from its maximum value, Nu_0 . In this experiment, for $Y/d = 2$ and $Re = 23,000$, and for $Y/d \leq 4$ and $Re = 50,000$, the streamwise Nusselt number distributions were observed increasing values in the region $1.3 \leq r/d \leq 1.5$ and reached its secondary maxima at $r/d \cong 2.2$. Correlations of Nu_0 were obtained as follows:

$$Nu_0 = 1.68(Re)^{0.48}(Y/d)^{0.1}(D/d)^{-0.18} \quad \text{for } 2 \leq Y/d \leq 6 \quad (2.20)$$

$$Nu_0 = 1.38(Re)^{0.57}(Y/d)^{-0.28}(D/d)^{-0.18} \quad \text{for } 6 \leq Y/d \leq 10$$

2.2.2 Effect of turbulence on stagnation point/streamwise local heat transfer

In the early 50's, Giedt (1951) investigated the effect of turbulence level of incident air stream on local heat transfer coefficients around a cylinder. The diameter of heated cylinder was 102 mm with a length 533 mm. It was found that the average heat transfer coefficient was increased from 10% to 20% due to increasing of turbulence level, with Reynolds numbers varying from 90,900 to 212,000. The local heat transfer in the stagnation region was also increased approximately 25% due to increasing of turbulence level.

Seban (1960) demonstrated that the local heat transfer coefficients and recovery factors from the elliptical and circular cylinders were affected by the free stream turbulence. Larger local heat transfer coefficients were obtained by increasing the turbulence intensity, in a way dependent upon the location of the cylinder configurations, through a direct increase in the heat transfer to the laminar boundary layer, through an earlier transition to turbulence, or through an alteration in the character of the separated flow. However, recovery factors were unaffected with respect to the turbulent intensity for attached boundary layer flow, but observing large changes in those separated flow regions.

Lowery and Vachon (1975) have reported on the effect of free-stream turbulence on heat transfer from heated cylinders placed normal to an air flow stream. Reynolds number ranging from 109,000 to 302,000 at values of turbulence intensity from 0.4% to 14.2% were performed. The results showed that the remarkable increases in heat transfer rate over the theoretical zero turbulence value were on the order of 20% occur for small increases in lower values of turbulence intensity (0.4% to 1.2%). In the laminar boundary-layer range along the cylinder, $0 < \theta < 40^\circ$, the effect of increased turbulence intensity always increased the local heat transfer rates and appeared to be independent of Reynolds number over the range of this investigation. Partial success was obtained in correlating the linear relation between the overall rate of heat transfer and the values of $TuRe^{0.5} < 10.5$ as $Nu/Re^{0.5} = 0.686 + 0.043TuRe^{0.5}$.

Cooper et al. (1975) used the liquid crystal technique to obtain both qualitative and quantitative heat transfer and fluid flow information on heated cylinder placed in free air stream. A 100 mm diameter of circular cylinder was used and Reynolds numbers varied from approximately 40,000 to 150,000. The turbulence intensity was found to vary from 0.5% to 0.7% in the clear test section. The angular variation of the Froessling number Fr obtained with liquid crystal thermography was compared with the experimental results of Giedt (1951) and Seban (1960). The experimental heat transfer results were in close agreement with those obtained by other investigators. In addition, the effects of flow separation, the separation bubble region, the turbulent boundary layer and the turbulent wake on the heated cylinder could be observed using this non-intrusive liquid crystal thermographic technique.

Kataoka et al. (1992) investigated the local controllability of slot jet impingement heat transfer on a plate by immersing an array of circular cylinders with the fixed Reynolds number of 4,500. Maximum heat transfer on the central stagnation line was augmented by about 180% due to the acceleration and surface-renewal effects of large-scale turbulent eddies impinging on the heat transfer surface when the cylinder array was placed from 4 to 6 cylinder diameters ($D = 8$ mm) upstream of the heat transfer surface in a passing arrangement. The maximum heat transfer location was shifted, without attenuation, to half the cylinder pitch off the jet axis on both sides by a blocking

arrangement whereas the central stagnation line heat transfer was suppressed largely due to the blocking effect.

2.2.3 Effect of surface curvature on local/average heat transfer

In the mid 50's, Kreith (1955) investigated the influence of curvature on heat transfer for fully developed turbulent flows. It was found that the heat transfer from a heated concave wall was considerably higher than from a convex wall of the same curvature and under the same conditions of flow. The Nusselt number for a concave surface was 25% to 60% higher than for a convex surface at the same Reynolds number for fluids having Prandtl numbers higher than 0.7. For analytical investigation, the influence of curvature was insignificant at Reynolds number below 10^5 , but the Nusselt number along a concave surface was twofold higher than that of a convex surface at Reynolds number above 10^6 for fluids having a Prandtl number below 0.02.

Since then, more papers related to the effect of surface curvature on the heat and flow characteristics have been published. Sawyer (1962) and (1963) measured the growth of two-dimensional turbulent wall jets blowing round surfaces constructed to maintain the ratio of jet thickness b to surface radius of curvature R at a constant value along the length of the jet. For b/R of the order of 0.05, the rate of spread of the curved jet was found to be increased by about 50% for a convex surface and decreased by about 50% for a concave surface as compared with that of a plane wall jet. He also concluded that the curvature has a considerable effect on the entrainment properties of jets. This was significant in a number of situations, for example, the growth of curved wall jets, the curved-jet recirculation flows associated with air cushion vehicles, and the velocity field induced by curved jets.

Schuh and Persson (1964) investigated the mean heat transfer coefficient on a circular cylinder placed symmetrically in a two-dimensional jet with Reynolds number around 20,000 to 50,000. The maximum heat transfer coefficient was obtained for a jet with a height of one eighth of the cylinder diameter and with the cylinder at a distance from the nozzle exit of about 2 to 8 times the jet height. The heat transfer coefficient was found to be about 20% higher than that for a cylinder in free stream (an unlimited

parallel) flow with negligible turbulence in the main stream and with an undisturbed speed equalled to that in the nozzle exit. They explained that this result was due to the characteristic of thin jets which adhered to curved surface of the cylinder (Coanda effect) and the high turbulence intensity in a jet.

Thomann (1968) investigated the effect of streamwise wall curvature on heat transfer in a supersonic turbulent boundary layer. The free-stream Mach number was 2.5 and the Reynolds number based on total model length was about 4.5×10^6 . In comparison with the constant pressure along the flat, concave and convex wall cases, it was found that the heat transfer rate was increased to about 20% in the concave wall, while the heat transfer rate was decreased to about 20% in the convex wall in respect to the flat wall case. The changing of heat transfer rate was mainly due to an increase or decrease of turbulent mixing by the effect of the curvature.

So and Mellor (1972 & 1973) investigated the turbulent boundary layer flow with uniform and adverse pressure distributions along a convex and concave surface of varying curvature. They found that the turbulent mixing between fluid layers was very much reduced along the convex surface. Under the same wall static pressure distribution, the ability of the flow to support adverse pressure was reduced. Hence the flow would separate earlier than the corresponding plane flow. Turbulence energy production was drastically reduced and almost vanished at about half the boundary layer thickness. However, the law of the wall held and the determined skin friction correlated well along the convex surface with other measurements. A system of longitudinal vortices similar to the Taylor-Gortler type vortices was observed inside the boundary layer along the concave surface, thus indicating the enhancement of turbulent mixing. The turbulent energy production was not confined to the region near the wall, but rather it extended nearly to the edge of the boundary layer. A self consistent set of curved turbulent boundary layer equations was derived together with a modified eddy viscosity. Those equations correlated well with the experimental data on flow along the convex surface with arbitrary pressure distribution. However, it could only be used to predict the mean characteristics of the flow along the concave surface due to the existence of the system of longitudinal vortices inside the boundary

layer.

Wilson and Goldstein (1976) investigated the effect of convex curvature surface of a circular cylinder on the development of a two-dimensional wall jet. The jet width was 50.8 cm, and the slot heights were 0.615 cm and 0.609 cm for the curved and plane wall jets respectively. The radius of the convex surface was 101.6 mm. The Reynolds numbers ranged from 3,500 to 16,500. They found that the centrifugal force instabilities could introduce rapid mixing of the curved wall jet with its surrounding causing the enhancement of turbulence intensity and Reynolds shear stress in the jet. The curved wall jet showed a strong sensitivity to slot Reynolds number variations, which caused the jet separation point from the curved surface to increase with increasing the Reynolds number until a stable separation point occurred at Reynolds number of 9,000, but the wall jet was relatively insensitive to the slot Reynolds number for values greater than 5,000. Large departures from self-preservation of the turbulence velocity field in the curved jet were observed, while the streamwise mean velocity profiles were unchanged in downstream development region.

Mayle et al. (1979) showed that the heat transfer rate on the concave surface was about 33% greater than the correlation of flat plate, while on the convex surface it was about 20% less at the downstream position of about 120 boundary layer thickness from the start of curvature. The results on the concave surface were still changing rapidly (compared to the results on the convex surface) at the downstream position due to the streamwise growth of large-scale vortices with the axes in the flow direction (Gortler vortices). Although similar heat transfer trend on the curvature had been reported by Thomann (1968), the deviation was much larger than the Mayle's experiment in which a much smaller Reynolds numbers (1,000 to 2,000) and Mach number of about 0.06 were tested. It was shown that the curvature effects were more important at higher Mach numbers.

Simon & Moffat (1982) investigated the effects of convex curvature surface on the heated turbulent boundary layer. It was found that the strong convex curvature effects on the parameters of surface heat transfer rates, mean velocity and temperature profiles

were significant. The Stanton numbers and skin friction coefficients were reduced almost 35% compared with the flat-wall value. The recovery from curvature was extremely slow in all the parameters tested. The mean velocity profiles were affected in the outer layers, but not in the inner-region structure. The turbulent Prandtl number deduced from the thermal law-of-the-wall was increased from 40% to 50% due to the strong convex curvature surface.

Potts (1984) studied the effects of a round turbulent jet impinging normally on a circular cylinder and the resulting flow field. The cylinder had a diameter of 168.3 mm. The nozzle exit velocities of 120 and 150.4 m/s were used with a 17.5 mm diameter. The circular jet was impinged upon the cylinder at distances of 7, 15 and 30 nozzle diameters. The free jet was validated and found to agree very well with both theoretical predictions and previous experimental work. The velocity profiles about the cylinder were found to be similar to those found on flat plate for nozzle distances close to the cylinder ($Y/d=7$) but became significantly different at farther nozzle distances ($Y/d=15$ and 30). At the farther nozzle distance, the velocity profiles along the cylinder's axis became very flat and they showed very little similarity to that of a flat plate in the circumferential direction. The spread rate of the wall jet along the cylinder was much greater than that found on a flat plate. Increasing both with farther nozzle distances and as the circumferential axis was approached. The velocity of the wall jet was found to decay much slower than that of a flat plate, especially about the circumference of the cylinder. The wall jet turbulence profiles were found to be similar to those of a wall jet on a flat plate except at larger nozzle distances ($Y/d=30$) where the turbulence profiles in the circumferential axis decreased significantly. Based on the experiments, it was found that the wall jet might have attached to the cylindrical surface until about 120° to 160° from the impingement point, depending upon the flow velocity and nozzle distance. The relationship between the radius of the nozzle and the cylinder was found to be a very significant parameter in the formation of wall jet upon the surface curvature.

Alhomoud (1984), and Sparrow and Alhomoud (1984b) studied the mass (heat) transfer coefficients and fluid flow patterns from a circular cylinder due to a slot jet

impingement. In one set of experiments, the symmetry plane of the slot jet was aligned with the axis of the cylinder, while in other set of experiments, the slot jet was offset from the cylinder. The effects of three dimensionless geometrical parameters, the offset ratio, E/D (0, 0.5 and 1.0), the slot width ratio, W/D (0.25 and 0.5) and the slot-to-cylinder separation ratio, Y/D (3.25 to 7.25) were investigated over the Reynolds number ranging from 4×10^3 to 6.3×10^4 . From the experiments, it was concluded that the heat transfer coefficient increased with the slot width and Reynolds number but decreased with increasing the slot-to-cylinder separation distance. At large offsets the results were relatively insensitive to the separation distance. The effect of offset was accentuated for narrow slot width and at small slot-cylinder separation distances. The largest measured offset-related reduction in heat transfer coefficient was up to 53%. In addition, the numerical solution was developed for a laminar jet ($Re < 1,000$) and for Prandtl numbers of 0.7 and 2.5. For $Re \cong 400$ to 450, the difference between a special set of low-Reynolds number experiment and the computation was about 7%. The deviation increased to about 17% for $Re = 910$.

Rojas et al. (1987) used the Laser-Doppler Anemometry and liquid crystal technique to obtain the velocity and local wall heat transfer characteristics of the flows in two curved diffusers of rectangular cross section with C and S-shaped centerlines, respectively. The effects of secondary flow near the heated wall caused the increasing of local wall heat transfer coefficients and quantified the variation for maximum secondary-flow velocities ranging from 1.5% to 17% of the bulk flow velocity.

Fujisawa and Kobayashi (1987) investigated the effects of strong convex curvature on the mean flow and turbulence characteristics of two dimensional wall jets experimentally. The three constant radius convex surfaces considered were 83, 134 and 250 mm. The two-dimensional rectangular nozzle was used with slot height of 5 mm and width of 588 mm, thus giving a width to height aspect ratio of approximately 120:1. The mean velocity at the nozzle exit was 40 m/s. The wall jet spreading and the levels of Reynolds stresses along the surfaces were increased significantly by strong convex curvature, compared with those of the plane wall jet. These flow characteristics were well correlated by the ratio of half width of wall jet to the surface radius except

for the initial region of the convex surface. The interactions of mean flow and turbulence were observed to be increased due to the production of the turbulent fluctuation normal to the surface, the shear stress and the advection of streamwise turbulent fluctuation.

Davenport (1989) investigated the local heat transfer coefficients due to a water 60° cone spray impinging on a cylindrical surface. It was found that heat transfer coefficient in the region of direct impingement was essentially uniform but dropped off rapidly outside this region, being 50% of its maximum value at about 1.45 times the radius of direct impingement. A year later, Davenport (1990) studied the heat transfer distribution due to arrays of liquid sprays impinging on a cylindrical surface. He concluded that heat transfer coefficients from a row of 30° cone sprays with nominally 50% overlap above the spray centre line varied from the maximum values at the centre of each spray pattern to about 50% of this between sprays. With 60° cone sprays and the same nominal overlap, there was no measurable variation along the center line. In the indirect regions, the coefficient maxima were in the zones between spray centre lines where thick lines of coolant flowed down the surface. Switching out a single 30° cone spray reduced the circumferentially averaged coefficient to about 30% of its maximum value where the spray was switched off. With two or more sprays switched off, the remaining sprays behaved as though they were isolated. Changing the glancing angle of sprays substantially altered the coefficient distribution and led to 44% increase in the integral of heat transfer coefficient with respect to area.

2.3 Numerical Heat Transfer Investigations

Miyazaki H. (1975) and Miyazaki and Sparrow (1976) obtained a closed form solution for the potential flow about a circular cylinder situated in an impinging slot jet. Among other results, the potential flow solution produced the free stream velocity for the boundary layer adjacent to the cylinder surface. A basic feature of the solution was the division of the flow field into subdomains, thereby making it possible to employ harmonic functions that were appropriate to each such subdomain. The boundary conditions on the free streamline and the conditions of continuity between the subdomains were satisfied by a combination of least squares and point matching

constraints. Numerical evaluation of the solution was carried out for cylinder diameters greater or equal to the nozzle width, D/W , in the range from 1 to 15, and for a range of dimensionless separation distances between the nozzle and the impingement surface, Y/W , in the range from 0.5 to 2. Results for the velocity distribution on the cylinder surface and for the position of the free streamline showed that the flow field was not symmetric on the fore and aft part of the cylinder. Rather, the skewing was accentuated as the cylinder diameter increased and the nozzle distance decreased (relative to the nozzle width). Pressure distribution in the stagnation region of the cylinder was evaluated and compared with available experimental data. A very good agreement prevailed up to 20° from stagnation point for $D/W=1$ and 2. However, the agreement was not satisfactory for $D/W=0.4$ since the flow field in that case was influenced by early separation, which was not taken into account in their analysis. The Nusselt number predictions agreed well with experimental results obtained using the naphthalene sublimation technique. The Nusselt number at the stagnation region for the convex circular surface could be expressed as follows:

$$\text{Nu} = 0.312 + 0.1431\theta^{-0.75}\text{Re}^{0.5} \quad (2.21)$$

van Heiningen A. R. P. et al. (1976) investigated the effects of slot nozzle exit and uniform suction profile on the flow and heat transfer characteristics of a semi-confined laminar impinging jet for $\text{Re}=100, 450$ and 950 and $W/Y=0.25$ numerically. The full Navier-Stokes and energy equations were used to incorporate into their vorticity-stream-function forms. The maximum heat transfer was found at the stagnation point and was almost independent of Reynolds numbers range studied. The stagnation heat transfer value for a jet with a parabolic velocity profile was 1.5 to 2 times higher than the value for a flat velocity profile due to the contraction and the higher momentum of the parabolic jet. The maximum skin friction ratio was about 2.7 for $\text{Re}=950$. The relative effect of suction was the smallest in the stagnation region and the heat transfer did not vary much over the length of the plate. In their study, the influence of variable properties on the Stanton number distribution, based on the properties of jet exit temperature as 450 K and the temperature of the plate as 300 K was hardly affected.

Ojha S. K. (1977) predicted the effects of curvature on the flow near the impingement region of a two-dimensional incompressible jet impingement over a curved surface. The flow regime near the stagnation point was divided into inviscid and viscous flow regions in a curvilinear coordinate system. The numerical solutions predicted well in the impingement region and the curvature length of half slot width from the stagnation point. It was shown that the inviscid flow velocities decreased as a result of decreasing of surface curvatures. The increasing of the surface curvature would move up the first-order boundary-layer velocity profiles accordingly. However, increasing of the surface curvature would suppress the first-order displacement of momentum thickness. The total skin friction was much higher in the case of a concave surface than in the case of a convex surface.

Faghri (1984) used a finite difference scheme to obtain numerical solutions for a slot jet impingement on a cylinder. An algebraic non-orthogonal coordinate transformation which mapped the complex fluid domain onto a rectangle was developed. The computations were performed with (12x26), (12x30), (12x34), and (12x43) grid points, respectively for $Re = 100, 200, 500$ and 1000 . The distance from the center of the cylinder to the outflow boundary varied from 5.5 cylinder diameters for $Re = 100$ to 22.5 cylinder diameters for $Re = 1,000$. The agreement between the predictions and the experimental results was satisfactory, but there was a remarkable deviation between the developed numerical scheme and an alternative computation using the stepped-boundary approximations.

Polat et al. (1985) used a two-equation ($k-\epsilon$) model of turbulence to predict the flow and heat transfer characteristics of a single, semi-confined turbulent slot jet impinging normally on an impermeable isothermal planar surface. The effect of jet turbulence level did not affect on the axial centerline velocity profile. For $Y/W = 6$, the predicted centerline velocity did not start to decay until about $4W$, which was lower than the values observed by previous workers such as Gardon and Akfirat (1965), Cadek (1968) and Sadd (1981). The local Nusselt number at stagnation point was enhanced about 41% by increasing the jet turbulence intensity from 0.7% to 10% and an addition of 48% when it further increased the jet turbulence intensity from 10% to 28% for

$Y/W = 2.6$ and $Re = 10,000$. However the average lateral Nusselt number was increased only 2% to 10% by increasing the jet turbulent intensity from 0.7% to 28%. It was observed that the inflection point (secondary peak) moved away from the stagnation point when increasing the jet turbulence intensity due to the diffusion of its turbulent kinetic energy. They also argued that this secondary peak would be observed near the stagnation line and not moved away from it if the occurrence of inflexion point could be simply explained by the transition of the boundary layer from laminar and turbulent flow. Furthermore, no secondary peak occurred when the diffusion of turbulent kinetic energy reached the jet centerline. For the same Y/W and jet turbulence intensity, the local Nusselt number at stagnation point and the secondary peak became more enhanced and pronounced when the Reynolds numbers were increased.

Shyy et al. (1991) studied the heat transfer and convection characteristics of superheated turbulent argon jet interacting with a solid object numerically. Two flow jet configurations were stimulated. One case for a slot jet impingement on a solid cylinder inside a circular cylindrical chamber and the other case for a circular jet impingement on a solid sphere inside a circular cylindrical chamber. Both superheated jets (7,000 K and 100 m/s at the inlet) issued into a chamber and impinged on a solid object of a constant wall temperature of 1,000K. Based on the object diameter, the incoming density and viscosity, a low Reynolds number $\cong 2,000$ version of the $k-\epsilon$ two equation model were used in the context of adaptive non-orthogonal grid system. In both jet configurations, the increasing of inlet turbulent intensity (5% to 15%) could enhance not only the effectiveness of turbulent mixing within the gas phase and the heat transfer between gas and solid object, but also the highly non-uniform Nusselt number distributions around the object. For the slot jet configuration, the increased turbulent intensity of the incoming fluid could resist the adverse pressure gradient and suppress the flow separation along the object, but not in the circular jet configuration due to much smaller area ratio of jet compared to the ambient gas volume.

Celik and Shaffer (1991) studied the mean turbulent flow past a circular cylinder. The standard $k-\epsilon$ model and the well known wall function were employed in both boundary-fitted coordinate and cylindrical-polar grids. For the subcritical flow regime

($Re = 1 \times 10^5$) and supercritical flow regime ($Re = 3.6 \times 10^6$), the predicted pressure coefficient distribution, location of separation and wall shear stress were in fairly good agreement with the experimental work on having a sufficient number of grid cells (points) placed in the thin boundary layer of the cylinder up to the separation point. It was pointed out that a better prediction could be achieved if the first grid point was placed within the viscous sublayer or at most the buffer layer. However the agreement deteriorated rapidly after the separation point. This could be attributed to the fact that the numerical model did not take into account the presence of vortex shedding, the transition of the boundary layer from laminar and turbulent flow, and an adverse pressure gradient.

Kang and Greif (1992) investigated the flow and heat transfer distributions from a plane laminar hot buoyant impinging air jet on a circular cylinder numerically. The effects of the Reynolds number, $Re = 100$ to $1,000$, Grashof to Reynolds number ratio, $Gr/Re^2 = 0, 0.1, 0.5$ & 1.0 , the distance between slot nozzle and the cylinder-to-radius of a cylinder ratio, $Z/R = 5$ & 10 , half slot width-to-radius of a cylinder, $W_{0.5}/R = 0.6, 0.8$ & 1.0 parameters were studied. They concluded that the flow pattern was stable and symmetric over the range of parameters studied. The results in flow and heat transfer were quite different from that for uniform flow. The Nusselt number was increased due to the effect of flow-acceleration of buoyancy jet and reduced the separation bubble downstream of the cylinder. The average Nusselt number was increased with increasing Reynolds number and Grashof number. For a wider slot jet, the viscous diffusion and heat loss from the jet to the surroundings were reduced, which gave a higher skin-friction and Nusselt numbers. Both the stagnation and the average Nusselt numbers were increased at low Reynolds number with decreasing distance between the nozzle and the cylinder. However, the effects of reduced flow-acceleration for the shorter distance were dominant at the higher Reynolds numbers and given in smaller values for the stagnation and averaged Nusselt numbers.

Seyedein et al. (1994) used both low-Reynolds and high-Reynolds number versions of $k-\epsilon$ turbulence models to predict the two-dimensional flow field and heat transfer impingement due to a turbulent single heated slot jet discharging normally into a

confined channel. The parameters studied were the jet Reynolds number ($5,000 < Re < 20,000$) and nozzle-to-impingement surface spacing ($2.5 < Y/W < 7.5$). They concluded that the accuracy of the results of standard $k-\epsilon$ turbulence model depended on both parameters and the near-wall approach. The low-Reynolds-number isotropic $k-\epsilon$ turbulence model of Launder and Sharma was recommended to predict the flow and heat transfer characteristics of a confined turbulent slot jet.

Shiravi et al. (1995) presented a study of various $k-\epsilon$ turbulence models in order to identify the best model for an array of multiple confined impinging slot jets as well as exhaust ports in the confinement surface located symmetrically between adjacent jets, for comparing with the experimental data reported by Saad (1981) and Ichimiya et al. (1989). They have concluded that the flow field was predicted well in a single jet and multiple jets problem by using both "High Reynolds number" and "Low Reynolds number" including the standard $k-\epsilon$ model. However, the prediction of heat transfer to the impingement surface was only reasonably well predicted by all these models in a single jet problem. Only low-Reynolds model introduced by Abe et al. (1994) gave sufficiently correct prediction of heat transfer in multiple jets problem. It may be due to the using of the correct boundary conditions for the variable at the wall as well as good grid independency.

Dianat et al. (1996) used the standard $k-\epsilon$ turbulence model and a version of a second-moment closure to predict the flow resulting from the orthogonal impingement of circular and a two-dimensional jet on a solid surface. The predicted rms fluctuating velocity profiles normal to the surface on the stagnation line, mean velocity and shear stress profiles within the wall jet region and rms fluctuating radial velocity profiles within the wall jet region at the varied range of Re and Y/d or Y/W and r/d or r/W parameters were compared with previous experimental work. The second-moment closure demonstrated a much better predicted values in the stagnation and wall jet regions than the transport equation model.

Knowles (1996) used the standard $k-\epsilon$ turbulence model as well as the Rodi (1980) and Malin (1988) corrections to improve the prediction of the hydrodynamic field of

subsonic free and impinging jets, and the radial wall jet, respectively. It was shown that as the nozzle exit turbulence intensity was increased from 1.5% to 15%, both the rate of decay of the free jet and the spreading rate were increased accordingly. In addition, the length of potential core of the jet was shortened as more rapid diffusion was promoted in the mixing region. He concluded that the spreading rate of a free jet was overpredicted, but the spreading rate of a radial wall jet was underpredicted by using the standard $k-\epsilon$ model. Applying the Rodi correction could improve the free jet prediction, but Malin correction did not seem to enhance the spreading rate of the radial wall jet as well as its wall jet thickness.

Cziesla et al. (1997) computed heat transfer on the impingement plate of slot jets by large-eddy simulation (LES) with the dynamic subgrid-scale stress model for Reynolds number Re_{2w} between 600 and 3,000. The maximum difference in Nusselt number at stagnation point between the constant and parabolic nozzle exit velocity profile could be higher than 68%. More than 28% and 52% averaged heat transfer rates could be obtained if $Re_{2w} = 1,000$ and 1,500 and $Re_{2w} = 1,500$ and 3,000. The area-averaged Nu was correlated as follows:

$$Nu_{ave} = 0.202 Re_{2w}^{0.61} \quad \text{for } Re_{2w} = 600 \text{ to } 3,000 \quad (2.22)$$

For the three dimensional jet case, the spacing of the local Nu minima on the left- and right-hand sides of the jet centerline was decreased when the Reynolds number increased. A saddle-like contour of the Nusselt number distribution over the plate was also observed.

Recently, Craft et al. (1997) presented a new nonlinear eddy-viscosity turbulence model to handle non-equilibrium low Reynolds number phenomena. This model was tested on a flat plate at different levels of free-stream turbulence, a turbulent impinging jet on a flat plate and the flow around a turbine blade. They showed that this model was far more reliable than the linear eddy-viscosity model especially in impinging flows. However, they have pointed out that a defect in this model has appeared on convex surface due to its insufficient damping of the stress field results.

2.4 Summary of Review

A large number of publications for the case of simple geometries such as a unconfined/confined circular/slot jet impinging on a flat surface exist in archived literature. It is because the fluid dynamic structure of such processes is extremely complex and, as such, the problem is often reduced to the investigation of a single impinging jet which might be in turbulent/laminar. However, other configurations such as rows and arrays, orthogonal and non-orthogonal, and others jets impinging on a flat surface or circular (convex/concave) surface have received comparatively limited attention. They have been included in bibliographies such as Button and Wilcock (1978), Button and Jambunathan (1989), and Jambunathan and Button (1994). Critical reviews on various aspects of the experimental, analytical and numerical work also exist such as Arganbright and Resch (1971), Mujumdar and Douglas (1972), Livingood and Hrycak (1973), Becko (1976), Martin (1977), Hrycak (1981), Downs and James (1987), Polat et al. (1989), Launder (1991), Jambunathan et al. (1992), Viskanta (1993). These reviews highlight the paucity of data and correlations which can be applied to more complex surfaces. In this study, the overall existing jet impingement literature reviews have focused on the general experimental and numerical findings relevant to the complex geometries. Description of flow regions for a slot impinging jet on convex cylindrical surface, and the Nusselt number and Sherwood number correlations obtained for the curved surfaces are presented. Only a very limited heat transfer and flow studies of a circular/slot jet impinging on a convex cylindrical/spherical surface have been identified in this critical review. The work of Waltz and London (1964), Miyazaki H. (1975) and Miyazaki and Sparrow (1976), Ojha S. K. (1977), Sparrow and Alhomoud (1984), Potts (1984), Faghri (1984), Whitaker (1986), Gau and Chung (1991), Celik and Shaffer (1991), Kang and Greif (1992), Shiravi et al. (1995) and Lee et al. (1997) are relevant to the present study only to a limited extent, but no identical experimental and numerical configurations have ever been reported in comparing with the present investigation.

Chapter 3 Experimental Investigation

3.1 Introduction

"Experimentation is Not Just Data-Taking". In fact, a considerable portion of the time and effort are spent in the experimental planning, apparatus design and construction, debugging and execution of experiments, and data analysis and interpretation. Only a small part of the total time and effort goes to the actual data-taking of a well-run experimental programme, Moffat (1985), and Coleman and Steele (1989). This chapter aims at describing briefly the complete experimental facility with regard to the apparatus design and construction, the theory behind measurement techniques, the execution of experiments and uncertainties in experimental measurements, and analysis and interpretation of results.

3.2 Air Nozzle Jet System, Traverse and Ancillary Equipment

The experimental air nozzle jet system is shown schematically in Figure 3.1. The system consists of the air supply system, traverse and ancillary equipment.

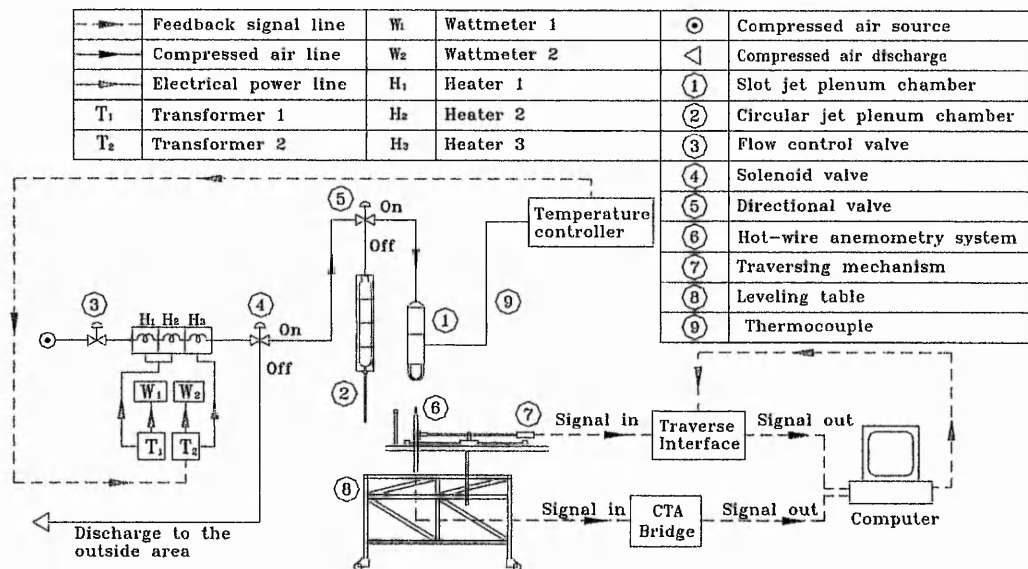


Figure 3.1 Schematic diagram of air nozzle jet system.

3.2.1 Slot jet tunnel design

The jet tunnel design had to meet the following criteria,

Contraction outlet dimensions	: 6.25 mm x 125 mm
Uniform temperature outlet	: $40 \pm 0.2^\circ\text{C}$
Maximum outlet velocity	: 42.6 m/s
Uniform velocity profile	: <1%
A low, repeatable turbulence intensity	

The air jet tunnel was designed as a slot nozzle type using the existing campus compressed air line. To ensure high air quality, air from the compressed air line passed through a set of air filtering system, a refrigerated air dryer, a high precision regulator, air receiver tank, heating and cooling unit, a high response solenoid valve, then through a settling chamber and contraction containing a layer of aluminum honeycomb to straighten the flow and turbulence eliminating screens to produce uniform velocity profile of the nozzle outlet. These are shown schematically in Figure 3.2 and Figure 3.3.

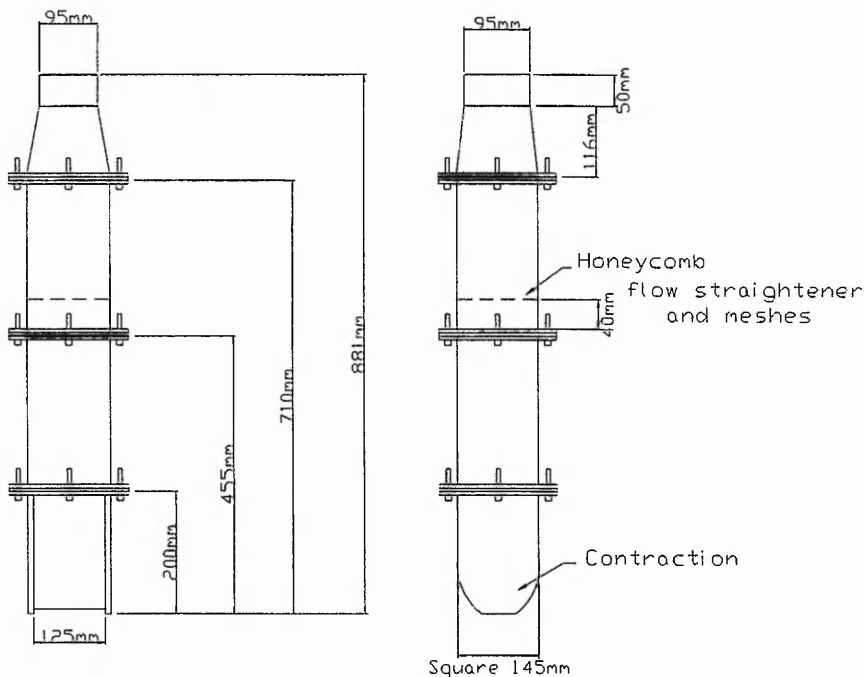


Figure 3.2 Schematic diagram of the slot nozzle and settling chamber.

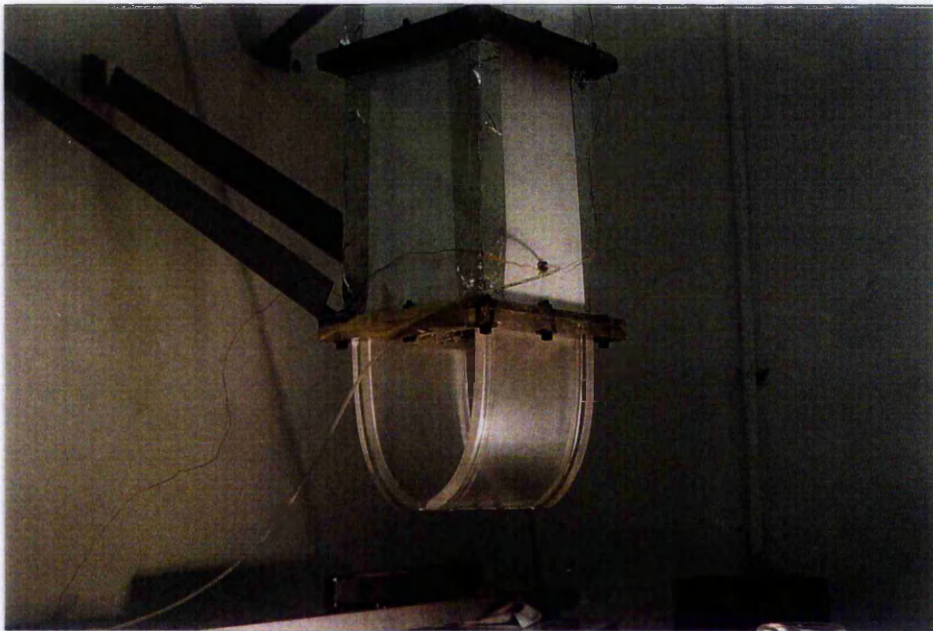


Figure 3.3 Photograph of the slot nozzle and settling chamber.

The diffuser section has an expansion angle of 12.2° in vertical plane and an area expansion ratio of 2.8 which, according to Mehta (1977), qualifies it as a wider angle diffuser. To reduce the possibility of any separation of boundary layer along the expansion section, curved mesh screen are placed at the entrance to diffuser. An aluminium alloy honeycomb which acts as a flow straightener, of 40 mm length and a cell size of 5 mm are used. Directly after the honeycomb, a fine mesh screen, of wire diameter 0.22 mm and an open area ratio of 0.745, is placed across the flow to minimise large scale turbulent structures. The distance between screens is 500 times the mesh wire diameter, i.e. 110 mm, which is the minimum length required for the small turbulent eddies, created by the mesh, to be decayed. The contraction to the slot nozzle was designed with a BASIC computer program described by Button and Leech (1972). The contraction area ratio was 20:1, giving a reduction in area from 125 mm x 125 mm to 6.25 mm x 125 mm, i.e. the slot nozzle exit area. The contraction length was calculated to be 153.24 mm and is curved in such a way as to minimise the growth

of boundary layer. The contraction profile co-ordinate is presented in Appendix A.

Velocity and temperature stability of the slot jet facility were determined by measuring both data every five minutes over a four-hour period. The mean jet exit velocity, and turbulence intensity, remained steady to within 2%. The jet exit temperature is stable to within 0.2 °C after the jet facility has been warmed up for more than three hours after setting up a particular jet exit temperature and velocity accordingly.

3.2.2 Hot wire anemometry system

The hot wire anemometer (HWA) operates as a thermal transducer. In fundamental terms the anemometer works by passing an electric current through a fine filament which is subject to a fluid cross flow. The filament is made from material which possesses a temperature coefficient of resistance, i.e. the resistance varies with temperature, which can be monitored by electronic equipment producing output signals when the fluid flow velocity and/or temperature is varied. The filament is fine enough ($\leq 5 \mu\text{m}$ in diameter) for considering as a point measurement in the fluid flow. Many literature on the application of hot wire anemometry are available, and the books by Bradshaw (1971), Perry (1982) and Bruun (1995) provide quite comprehensive information.

A complete set of Constant Temperature Anemometer (CTA) System (Dantec Main Frame-56C01 & 56B12, Mean Value Unit-56N22, Bridge-56C17, Signal Conditioner-56N20, Traversing System- 57H10 & 57G15, Data Acquisition board- Keithley STA-16 and Dantec Advanced acqWIRE software) and a miniature hot wire probe (Dantec 55P11, platinum-plated tungsten wire, 5 μm diameter and 1.25 mm length) are used to measure the nozzle jet exit fluctuating fluid velocity. A fully developed circular pipe experiment was set up to validate the suitability and accuracy of hot wire anemometry (HWA) for measuring jet exit profile. An axisymmetric nozzle of internal diameter 12 mm and length 22d was manufactured from seamless stainless steel pipe, described by Chan (1997). This was connected to campus air compressed line and other facilities similar to the slot jet arrangement, to provide a constant flow rate with a Reynolds number of 20,000. The length of the pipe is sufficient to ensure

that the flow issuing from the pipe is fully developed to within $\pm 5\%$, according to Obot et al. (1979). In Figure 3.4, the circular jet exit profile is compared with that computed from the empirical Equation (3.1) of Schlichting (1979):

$$\frac{U}{U_{\max}} = \left(\frac{y}{R}\right)^{\frac{1}{n}} \quad (3.1)$$

where $n=6.5$ for $Re_d=20,000$ and y is the distance from the wall of the pipe. It can be seen that the velocity profiles and magnitudes of U/U_{\max} measured by the hot wire anemometer are within $\pm 5\%$ of the empirical relationship.

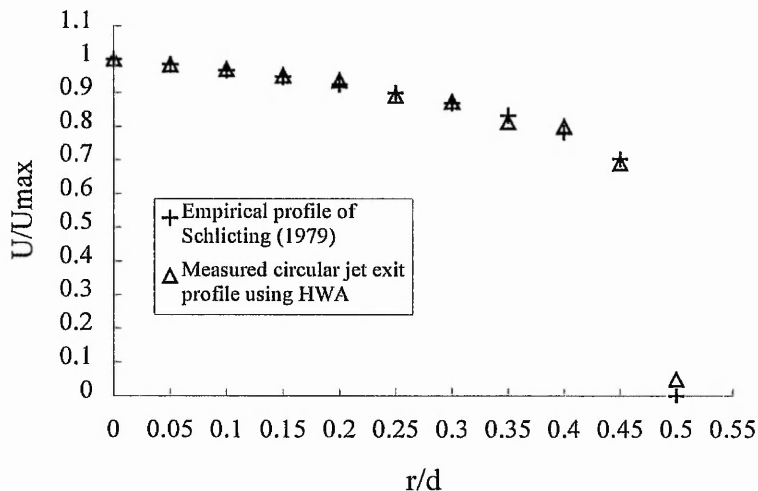


Figure 3.4 Comparison of circular jet exit profile with the empirical profile of Schlichting (1979).

3.3 Thermochromic Liquid Crystal Calibration System

3.3.1 Thermochromic liquid crystals

Thermochromic liquid crystals have in recent years been widely used in surface heat transfer measurement. In general, liquid crystals are non-intrusive, inexpensive and capable of high spatial resolution and accuracy in temperature measurement. However, the effect of viewing/illumination angle, optical access and deterioration could cause some problems. Proper calibration procedure is therefore necessary. Strictly

speaking, all thermochromic liquid crystals are cholesteric liquid crystals which possess a special optically active state and reflect incident light selectively over a specific range of wavelength (colour). As selective reflection of the liquid crystal is function of temperature, the liquid crystal colour display can be used as a temperature indicator over a larger area. Micrographs of these encapsulated chiral nematic thermochromic liquid crystal mixture (Hallcrest Ltd. BM/R30C5W/C17-10) are shown in Figures 3.5a to 3.5d. The encapsulated liquid crystals started to change colour from red to blue in microscopic view. It appears to contain microencapsulated liquid crystal with an average of 10 to 15 μm in diameter and lies within the manufacturers specification of 1 to 30 μm in diameter.

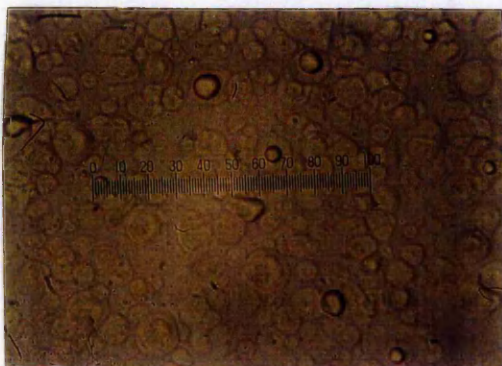


Figure 3.5a



Figure 3.5b



Figure 3.5c



Figure 3.5d

Figures 3.5a to d Micro-scope photographs of the liquid crystal (R30C5W).

During the last decade, digital image processing techniques have been increasingly used to interpret surface temperatures from liquid crystal thermography, from which local convective heat transfer coefficients are inferred. The image processing technique eliminates the subjective (human) interpretation of colour and replaces the labour intensive process of data analysis. Surface temperature information can be obtained using either chromatic or mono-chromatic interpretation. Akino et al. (1989a) used a set of band-pass optical filters; for a steady liquid crystal thermograph the filters were interchanged until a series of isothermal lines had been obtained. Ashforth-Frost et al. (1992) used a similar approach to record a single isotherm using a narrow band filter. Further work by Akino et al. (1989b) used a method of multiple regression between temperature and the three primary colours reflected by the liquid crystals. Wang et al. (1995) used the full intensity history recorded during an experiment to obtain the surface heat transfer coefficient at selected pixels. Several authors, Hollingsworth et al. (1989), Camci et al. (1991) and Toy and Savory (1992), Chan et al. (1994 & 1995) Wang et al. (1996), Gillespie et al. (1996), Babinsky and Edwards (1996) obtained the hue versus temperature relationship using the standard chromaticity diagram based on the RGB decomposition of colour. Many isothermal lines can be obtained from a single liquid crystal colour image. This method is more advantageous than the mono-chromatic approach in terms of time efficiency, image resolution and suitability for transient phenomena. Reviews of the characteristics of thermochromic liquid crystals, their mono/chromatic interpretation, and available methods of heat transfer/surface temperature measurement and their applications can be found in several papers by Kasagi et al. (1989), Moffat (1990), Parsley (1991), Jones et al. (1992), Ashforth-Frost (1994) and Baughn (1995). Most of these papers cover associated digital image processing techniques.

3.3.2 True colour image processing system

The image acquisition and processing system (as shown in Figure 3.6) used in the present investigation is composed of a high resolution 756 (horizontal) x 581 (vertical) pixels CCD video colour camera (Pulnix TMC-76-PAL) with a 12.5 to 75 mm zoom lens (Cosmicar C31204) , a colour frame grabber board (Imaging Technology Inc. VP-CFG-AT) for 24-bit true colour image processing with 8 bit digitization per colour

per pixel, a 16Mb image processing accelerator board (Imaging technology Inc. VIPA-16Mb), a 486 personal computer, a magnetic optical/Jaz disk driver, a professional PAL encoder/decoder compact box for RGB/super-video signal conversion (Truevision Inc. VIDI/O Box), a professional PAL super-video cassette recorder (Panasonic AG-7750 Editing SVCR) with optional super-video printer (Sony MDP-1).

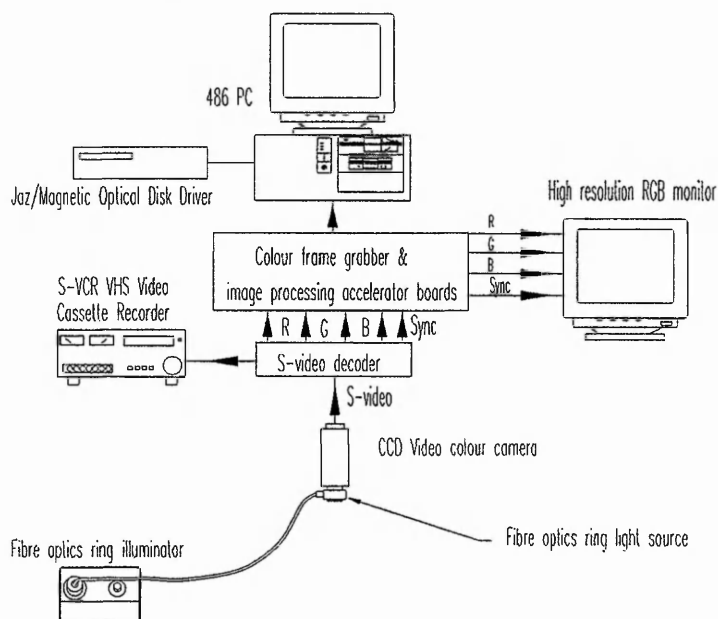


Figure 3.6 Schematic diagram of a colour image processing system.

In order to enhance the spatial resolution of the colour information, the conversion will take place between RGB and PAL super-video signals rather than regular composite video signals. The high quality of super-video signals from the CCD video camera will enhance twofold the spatial resolution of the colour information compared to the regular PAL composite video signals. It will also minimise the signal conversion errors in calibration and experimental work while recording on a high quality super-video cassette when required. The super-video output signals from the CCD video camera are first decoded and then individual red, green, blue and synchronization components of that signal are generated, using the high quality PAL decoder/encoder box. Three digitisers of the image processing board convert the RGB signals into an array of 768 x 512 pixels by sampling the signal in time, space and intensity. For most colour image processing, the colour description is normally separated from the colour (chrominance) and the intensity (luminance) information.

This avoids the generation of colour fringes and users can examine the colour or intensity information closely in their particular application. The RGB format signals are functions of lighting spectral distribution, temperature and filter transmissive. The Equations (3.2) of RGB format signals are shown as follows:

$$\begin{aligned} R &= \int_{-\infty}^{\infty} E(\lambda)R(\lambda)r(\lambda)d\lambda \\ G &= \int_{-\infty}^{\infty} E(\lambda)G(\lambda)g(\lambda)d\lambda \\ B &= \int_{-\infty}^{\infty} E(\lambda)B(\lambda)b(\lambda)d\lambda \end{aligned} \quad (3.2)$$

The PAL RGB primaries are typically transformed into YUV colour coordinate system. A relationship between the transmission primaries YUV and the RGB linear signals are formulated in Equation (3.3) as follows:

$$\begin{bmatrix} Y \\ U \\ V \end{bmatrix} = \begin{bmatrix} 0.299 & 0.587 & 0.114 \\ -0.147 & -0.289 & 0.437 \\ 0.615 & -0.515 & -0.100 \end{bmatrix} \begin{bmatrix} R \\ G \\ B \end{bmatrix} \quad (3.3)$$

The YUV primaries can be further transformed into the chromaticity coordinates and a chromaticity diagram. Detailed discussions of the trichromatic decomposition, colour space transformation in various coordinate systems and chromaticity can be found in Sproson (1983) and Hunt (1991).

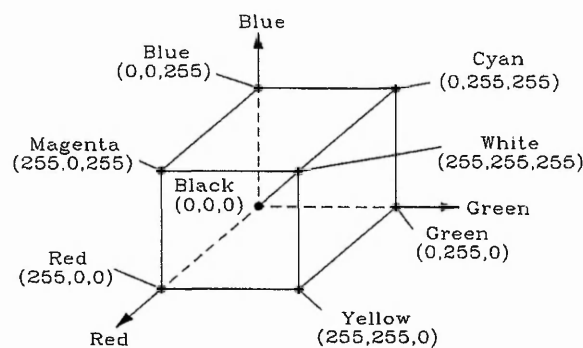


Figure 3.7 Format of a RGB colour system.

The current 24-bit true-colour image processing board from Imaging Technology Inc., USA is able to transform RGB into HSI and vice versa. The RGB colour model is based on a cube with boundary points at the 255 scale. It implies that the coordinate points (R, G, B) of eight fundamental colours on the cubical viewed along the principal diagonal from black to white as shown in Figure 3.7. This model is normally used to exhibit the colour images in monitors.

However, the HSI model is preferred as it can better approximate the human description of colour and is perceptually more uniform than the RGB representation. In addition hue corresponds to the attribute of a colour perception. Consequently the colour spectrum information of the thermochromic liquid crystals can be more usefully determined. The HSI colour format system can be imagined as a conical shape. Black colour is located at the shape point and white colour is located on the center of the cone base. The location of each colour of HSI colour system format is shown in Figure 3.8. Coordinate values of the HSI format colour system are (Hue, Saturation, Intensity).

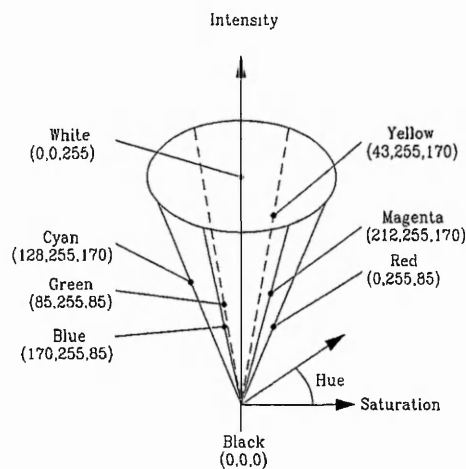


Figure 3.8 Format of a HSI (Hue, Saturation & Intensity) colour system.

The H,S,I values are given from 0 to 255 scale by this colour image processing board described in the following equations (3.4), (3.5) and (3.6), Chan et al. (1994):

$$\begin{aligned}
 H &= \{ [90 - \tan^{-1}(Z)] 255/360; G > B \} & (3.4) \\
 \text{or } &= \{ [270 - \tan^{-1}(Z)] 255/360; G < B \} \\
 \text{or } &= \{ 180 * 255/360 \text{ if } R=0 \text{ \& } G=B \} \\
 &= \{ 0 \text{ if } R=255 \text{ \& } G=B \}
 \end{aligned}$$

where $Z = [(2R - G - B)/(G - B)]/\sqrt{3}$

$$I = (R + G + B)/3 \quad (3.5)$$

$$S = [1 - \min(R, G \text{ or } B)/I] 255 \quad (3.6)$$

The R, G and B values in the above equations are based on the scale of RGB colour model as mentioned previously. A similar approach for the hue technique for the quantitative interpretation of liquid crystals was employed by Hollingsworth et al. (1989), Camci et al. (1991), Toy and Savory (1992), Braun et al. (1993), Chan et al. (1994), Crabtree (1994) and Wang et al. (1996), Hay and Hollingsworth (1996), and Babinsky and Edwards (1996). The colour image processing and super-video recording system were precalibrated using the standard Macbeth colour checker in the range of 0 to 255 hue values to be within $\pm 1\%$. Detailed discussion of a colour rendition chart can be referred to McCamy et al. (1976).

3.3.3 The Lighting system

The choice of different light sources is mainly dependent on their competence to influence the colour appearance of the object. Four common light sources are examined. They are regular fluorescent lamp, metal halide lamp, tungsten lamp and tungsten-halogen lamp/quartz lamp. Millerson (1991) described the characteristics of these light sources. The fluorescent lamp produces flicker problems due to the activated AC voltage reverse 100 times a second; the light inherently pulsates. More important still, the quality of fluorescent lighting is not really suitable for an optimal colour reproduction. In fact, the colour rendering of the object under the fluorescent lighting is so unstable that although "compensating filters" are normally available, many lighting cameramen prefer to turn them off where possible. Metal halide lamps produce a high proportion of ultra-violet light which is highly undesirable in the liquid

crystal application although an ultra-violet filter is available. Its uneven spectrum of luminance may produce some erroneous colour rendering. The colour and lighting quality of a tungsten lamp deteriorates with use, as its filament evaporates and blackens its bulb. The tungsten-halogen lamp eliminates these problems. In addition the major benefits of tungsten-halogen lamps are that they produce an excellent colour rendering even in a long run, a reasonably high efficacy, high luminance and compact size as described by de Boer and Fischer (1981). Herold and Wiegel (1980), and Farina et al. (1994) discussed the effect of the lighting/viewing arrangement on the thermochromic liquid crystals measurement. Farina et al. reported an uncertainty of ± 0.25 °C when an on-axis lighting/viewing arrangement was displaced up to $\pm 25^\circ$ from the normal. However, the liquid crystals temperature shift are more pronounced when the illuminant was placed off-axis.

In view of these, a 150W fibre optics ring light (cold light) sources and cross polarized/filtered CCD video camera lens are used to reduce radiative heating from the light sources to the thermochromic liquid crystals coated surface and ultra-violet light absorbed for the chromatic interpretation. In addition, a better thermochromic liquid crystals calibration technique is developed to compensate the significant effect on the chromatic interpretation due to the viewing angle, especially on the curved surface. This will be discussed in Section 3.3.6.

3.3.4 Selection of liquid crystal calibration technique

The accurate temperature-colour relationship of liquid crystals is essential. Such information obtained from the manufacturer is often insufficient. The calibration procedure of liquid crystals can be achieved by five general methods. A constant temperature water bath was used by several research workers. The temperature of the bath was monitored and controlled with a temperature controller up to 0.1 °C. The colour of the liquid crystal specimen could be calibrated by increasing the bath temperature in 0.1 °C incremental steps throughout the colour spectrum. A thin layer of liquid crystals suspended in a polyacrylate resin was applied to the glass plate, while the hot water was circulated on the other side of the plate to obtain a uniform surface temperature, as described by den Ouden and Hoogendoorn (1974). The painted

specimen was placed into a sealed clear plastic bag before immersion by Cooper et al. (1975). The water-proof liquid crystal sheets were submerged in the water bath to obtain the quantitative results by Gomiciaga et al. (1991). The working sections were covered with the liquid crystal sheet, while its uniform surface temperature and heat flux were achieved by the water bath, as described by Stasiak et al. (1996). However, to heat up and maintain the new water temperature setting is rather time-consuming. Moreover, this method is more suitable for water-proof liquid crystal sheet than the sprayable liquid crystals and black paint products. The sprayable black paint and liquid crystal layers may be water soluble, and if the material is splashed with water or water vapour, the uniformity of the thickness of liquid crystal will also be affected.

A stainless steel foil sheet was used by Hollingsworth et al. (1989) to adjust the liquid crystal colour display by varying a small power input to the sheet. The average surface temperature could be determined by the thermocouples which were attached to the other side of the foil sheet covered with a thick sheet of insulation. However, a uniform surface heat flux is not easy to obtain by using this electrical resistance heating element method. A thin brass disc with a thermocouple embedded in the center of the top face was used for calibration by Toy and Savory (1992), over which a layer of aluminium foil was attached to ensure high conductivity. Black paint and liquid crystals were sprayed onto the foil over a small area at the centre of the disc. The whole assembly was then placed directly onto the hot copper heater plate. Only by adjusting the power to the heater could the full range of the liquid crystal be calibrated.

Several thin foil thermocouples were flush mounted at different locations on the flat heat transfer surface by Camci et al. (1991), where the flat surface was sprayed with black paint and liquid crystal layers. However, the colour (in hue) value at specific pixel locations may not accurately reflect the local surface temperature especially in the narrow bandwidth of the liquid crystals.

A linear temperature distribution method was used to determine the temperature-colour relationship of the liquid crystals by Mizell (1970) and Akino et al. (1989). This technique has been widely used and is probably the most common one. However, Mizell (1970) reported the difficulty in maintaining the linearity of the temperature

distribution due to changing ambient conditions and the material used for the heat conducting surface. In order to minimise heat loss due to convection, the heat conducting block was placed in a plexiglass chamber with plate glass top. Most of the applications have involved flat surfaces, but a limited number of works, Mapple (1972), Herold et al. (1980), Smith et al. (1989), Moffat (1990), Jones et al. (1992) and Farina et al. (1994), have reported that small changes in viewing and/or illumination angle can have a significant effect on the chromatic interpretation of the thermochromic liquid crystal isotherm.

Based on the above calibration methods and viewing and/or illumination angle problems, a unique calibration technique has been developed for the present investigation on the curved surfaces. The effect of viewing angle when the light source and recording video camera (on the same axis) are displaced up to 72° from the normal, will be discussed in Section 3.3.6.

3.3.5 Liquid crystal calibration facility and procedure

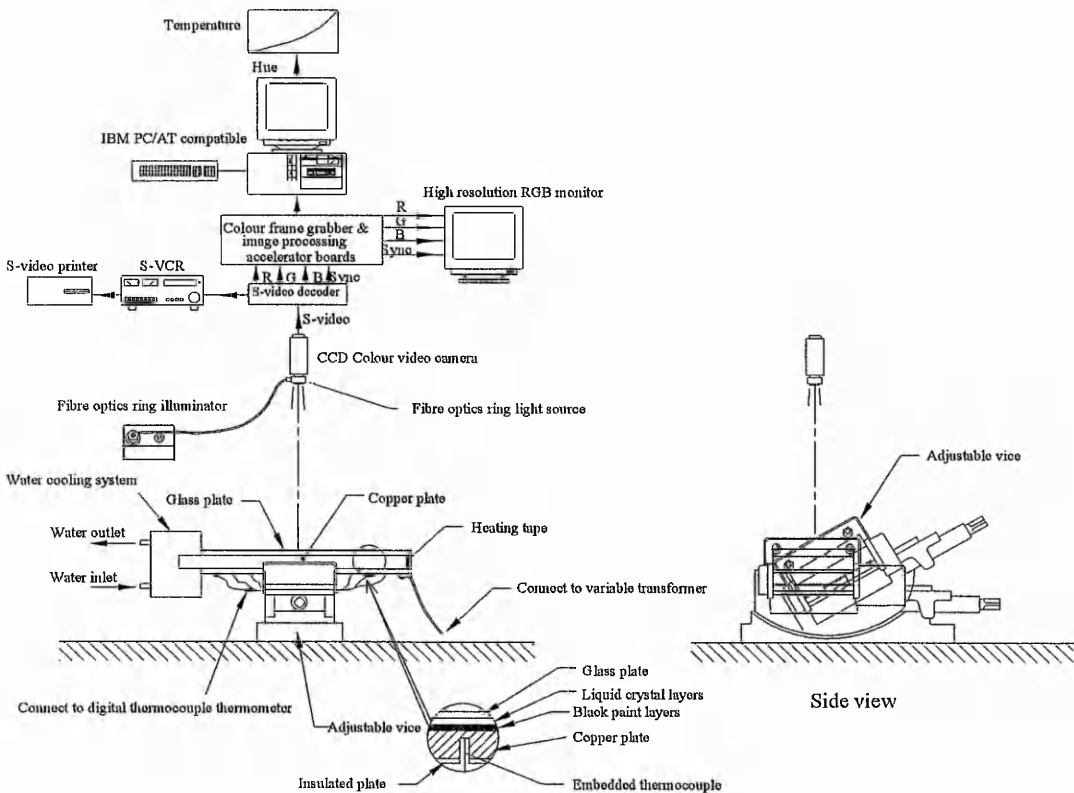


Figure 3.9 Schematic diagram of calibration apparatus layout.

The layout of the liquid crystal calibration rig is shown in Figure 3.9. A 600 mm long, 160 mm wide and 25 mm thick copper plate was used as the heat conducting surface. The sprayable black backing paint and 5°C bandwidth microencapsulated thermochromic liquid crystals (BB-G1, BM/R30C5W and R35C5W/C17-10 supplied by Hallcrest, USA) are sprayed uniformly onto a copper conducting surface using a pressurized artist's air brush (Olympos PB-306 and PB-308). A thin layer of thermochromic liquid crystals was applied over a water-based black paint which improves the colour resolution by absorbing unreflected light. The total thickness of the combined layers was estimated to be less than 30 μm with a time response within a few milliseconds by Schultz and Jones (1973). The colour temperature and the intensity (Minolta Colour meter III F and Intensity meter III F) of the light source are monitored over the test surface and were observed to be uniform within $3200\pm 10\text{K}$ and 300 ± 3 lux, respectively. A linear temperature gradient is imposed across the conducting surface using a variable power supply and a constant temperature water bath at opposite sides of the surface, and enclosed beneath is a low reflection glass plate with compression springs at four corners of the conducting surface to minimise overall heat transfer losses in the vertical direction.

The calibration test surface is illuminated completely by the 150W fibre optics ring light source on-axis lighting/viewing to prevent the ultra-violet and infra-red radiation effects and over heating on the coated surface during the thermochromic liquid crystals calibration process. An adjustable vice facilitated the change in illumination/viewing angle from 0° to 72° in increments of $3^\circ\pm 0.1^\circ$ (SPI-Tronic Pro 360° Digital Level). Nineteen fine-wire Type T thermocouples (0.74 mm diameter and 0.01 second time constant), were embedded in the bottom of the plate to measure the local surface temperature along the conducting surface. All the thermocouples were installed and pre-calibrated according to Moffat (1990). Temperatures in the range of 30°C to 40°C could be measured with an accuracy of 0.2°C . The location of these thermocouples can be defined on the captured image within the boundary limit of 768 pixels in the horizontal and 512 pixels in the vertical coordinates respectively. The full colour spectrum of the liquid crystals along the conducting surface can be observed by

varying the power supplied to the heating tape as shown in Figure 3.10 and is recorded using a Pulnix TMC-76-PAL CCD video camera with a professional Super-video recorder.



Figure 3.10 Photograph of liquid crystal colour spectrum along the heat conducting surface.

The developed calibration software program written in Microsoft C language (see Appendix B) is then executed to follow the flow chart as shown in Figures 3.11a and 3.11b. This program is incorporated into the colour image processing system and is used to capture the hue values at specific pixel locations of the liquid crystal colour display along the heat conducting surface, whilst the corresponding local steady-state surface temperatures measured and monitored by the embedded 19 fine-wire thermocouples, can be entered manually. All input data can be checked and conveniently deleted by this user-friendly environment software application tool. If any particular hue versus local surface temperature data at specific viewing angle are insufficient, then the calibration procedure can be re-executed. Nineteen commands (or function keys) of this software program have been developed to fulfill the calibration purpose. For each of the 48 sets of results, more than five hundred raw data have

been carefully recorded. Ultimately a graphic representation of the temperature-hue relationship can be generated, and the user can observe and note the trend of results immediately.

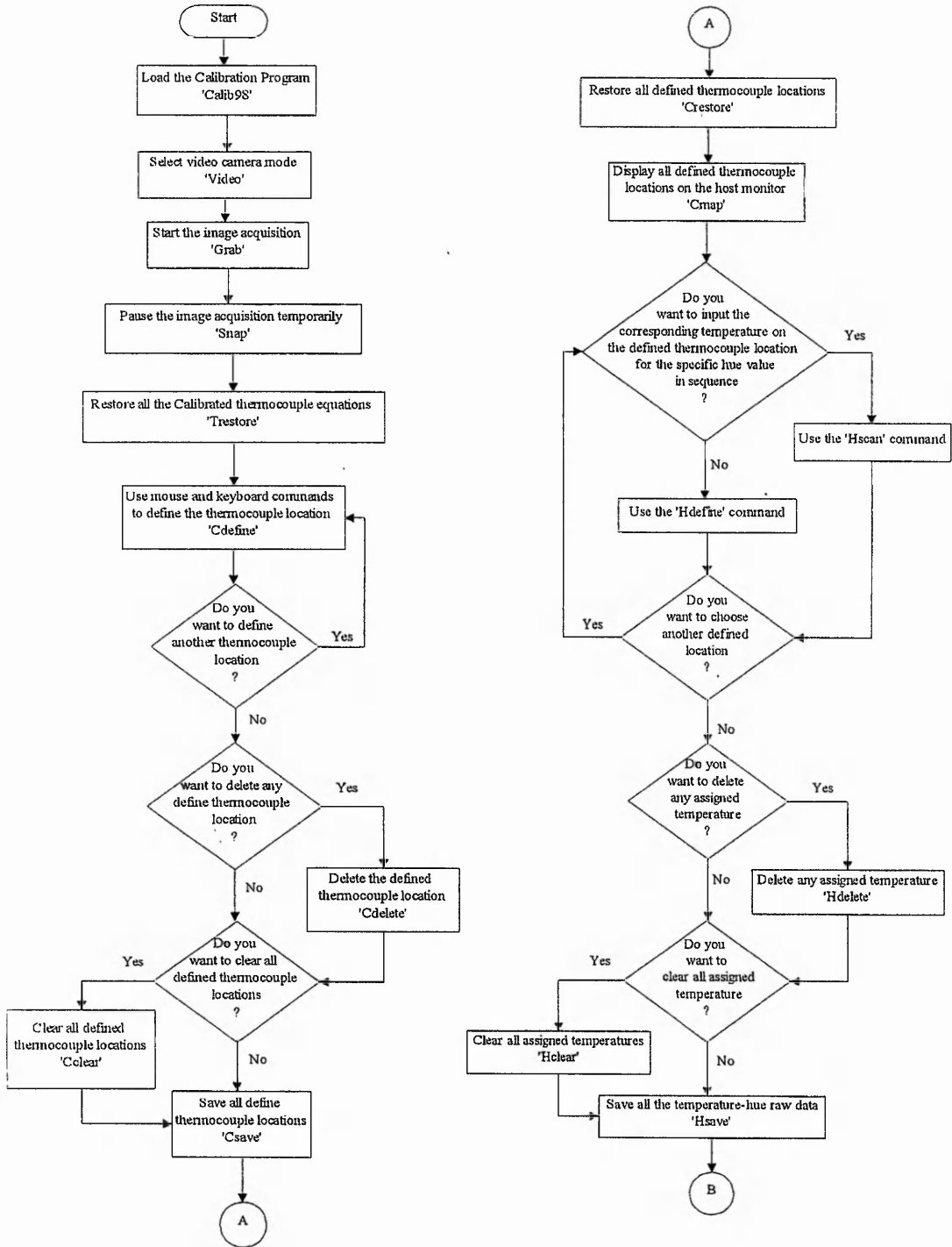


Figure 3.11a Flow chart of the calibration program.

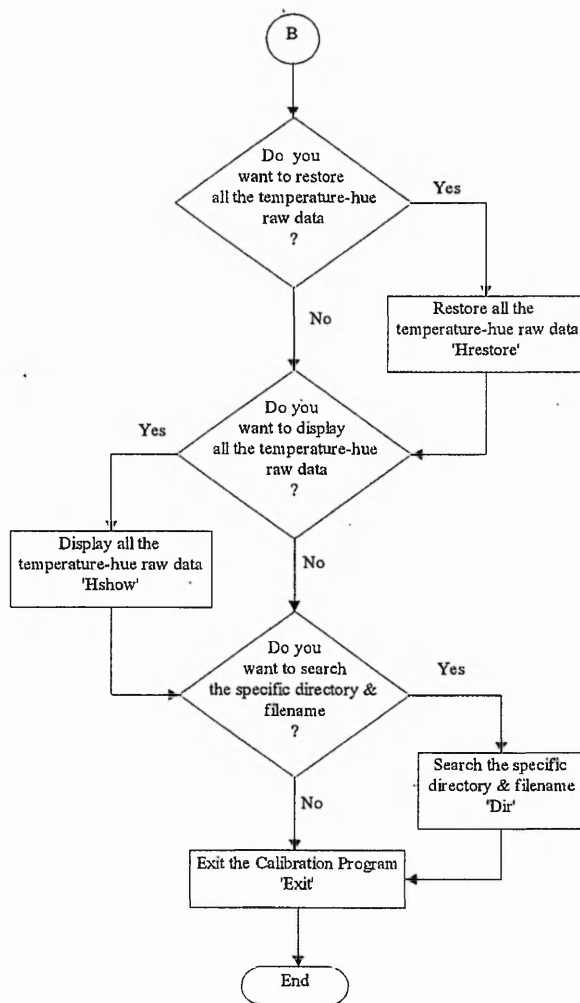


Figure 3.11b Flow chart of the calibration program.

3.3.6 Liquid crystal calibration surface-fit equations

In order to assess the effect of viewing angle on the temperature versus hue relationship, and to obtain the thermochromic liquid crystal formulations (R30C5W and R35C5W) calibration over the entire surface, more than 30,000 raw data were recorded and analysed. Based on a 95% confidence interval, the following generated surface-fit equation (3.7) was correlated to the collected data:

$$Z = a + b \exp \left[-0.5 \left(\frac{X-c}{d} \right)^2 \right] + e \exp \left[-0.5 \left(\frac{Y-f}{g} \right)^2 \right] + h \exp \left[-0.5 \left(\left(\frac{X-c}{d} \right)^2 + \left(\frac{Y-f}{g} \right)^2 \right) \right] \quad (3.7)$$

For the liquid crystals formulation of R30C5W:

$$\begin{aligned} a &= 29.69011, & b &= -0.18971, & c &= -95.64106, & d &= 204.46378 \\ e &= -0.19851, & f &= 282.31227, & g &= 113.91047, & h &= 18.39552 \end{aligned}$$

For the liquid crystals formulation of R35C5W:

$$\begin{aligned} a &= 35.91629, & b &= 0.26171, & c &= 126.67176, & d &= -3.67851 \\ e &= 22.70941, & f &= 323.63179, & g &= 99.41877, & h &= 12.56338 \end{aligned}$$

where Z, X and Y represent temperature, viewing/illumination angle from the normal and hue, respectively. These generated surface-fit equations with a fitted standard error of less than 0.3 °C, are used to determine the liquid crystal coated surface temperature of specimen with the transient technique in Section 3.4, and are shown in Figures 3.12a and 3.12b.

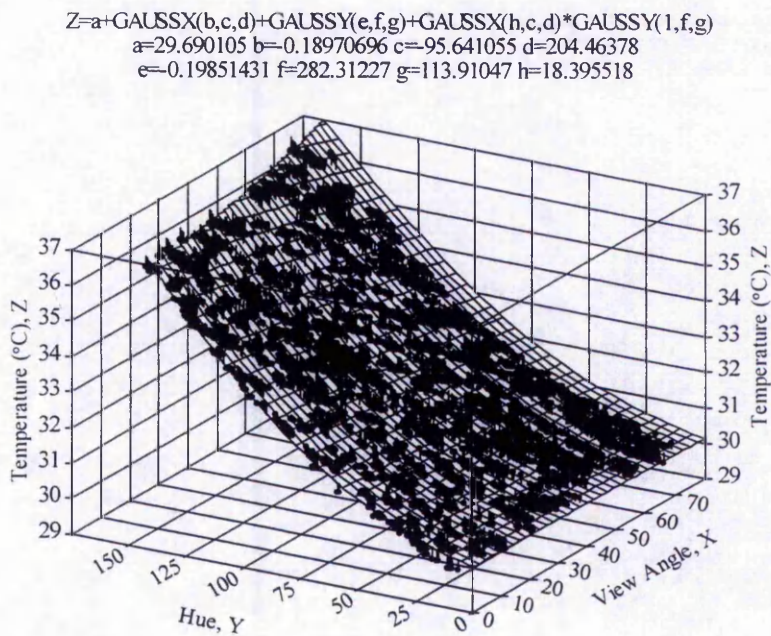


Figure 3.12a Thermochromic liquid crystal (R30C5W) calibration surface-fit curve.

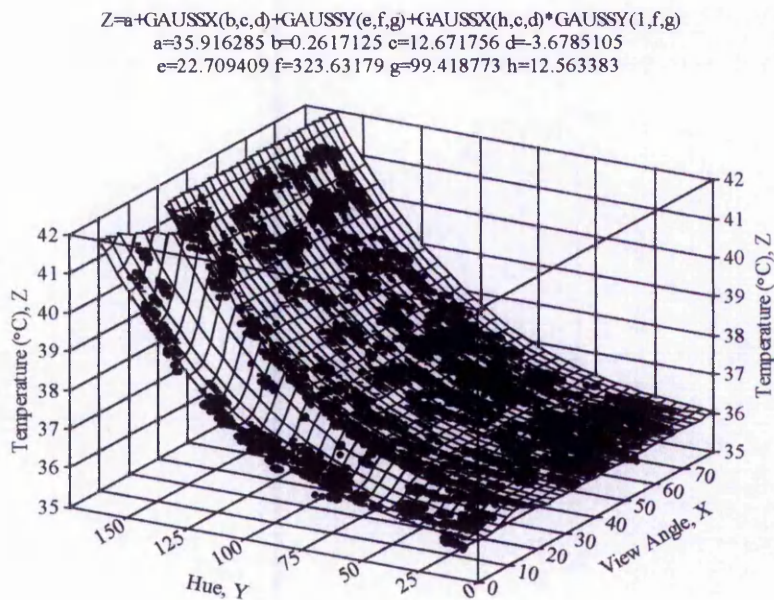


Figure 3.12b Thermochromic liquid crystal (R35C5W) calibration surface-fit curve.

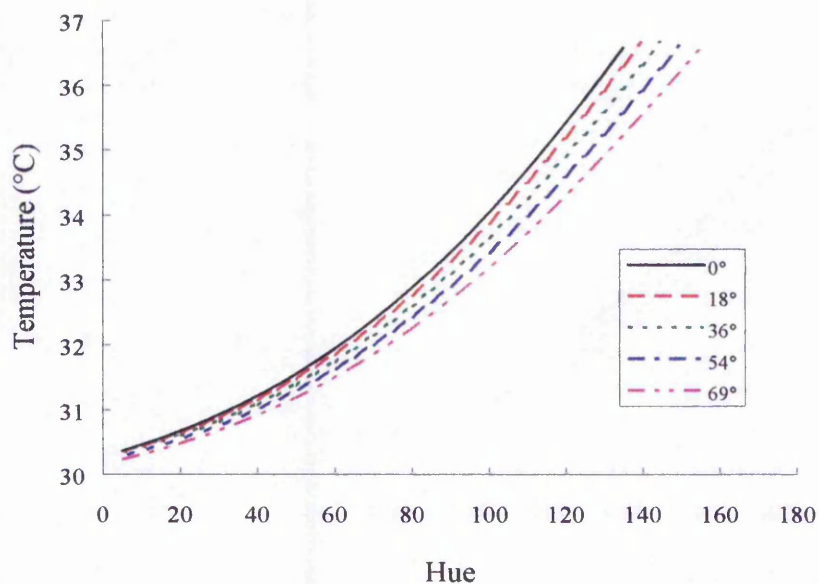


Figure 3.13 Effect of viewing angle on the temperature versus hue characteristics of thermochromic liquid crystals (R30C5W).

Figure 3.13 shows graphically the typical effect of viewing angle on the temperature versus hue characteristics of the liquid crystal (R30C5W) at 0° , 18° , 36° , 54° and 69° . The greatest effect occurs mid-spectrum of the liquid crystal formulation, where

variations up to -1.3°C were observed for a viewing/illumination angle of 69° with the normal. At about 25° , a maximum deviation of -0.4°C occurred which is slightly larger than that observed by Farina et al. (1994).

Assuming that the liquid crystal will exhibit the same characteristics when sprayed onto a test acrylic specimen as when applied to the calibration plate, the above surface-fit equations will allow the surface temperature (and hence heat transfer coefficient) to be determined, with relatively low and known uncertainty, over any oblique surface within the limits of the viewing angle investigated. This will considerably extend the application of the liquid crystal technique to many engineering applications, both in the laboratory and in-situ, where the liquid crystal technique was previously unsuitable due to the orientation or curvature of the surface.

Since liquid crystals deteriorate with time and exposure to ultra-violet light, it is recommended that the calibration be undertaken immediately prior to experimental tests. A second liquid crystal calibration at the end of all the experimental tests has been carried out. However, negligible change have been observed in the calibration temperature over several weeks of testing, if the test specimen is carefully stored in dark, dry and cool conditions. It should be noted that these equations are specific to the liquid crystal under test since the change of hue with temperature is non-linear and may vary with the liquid crystal formulation.

3.4 Heat Transfer Measurement System

3.4.1 Selection of the heat transfer measurement technique

Two commonly used methods for the heat transfer measurement are the steady state technique, where experimental properties do not vary with time, and the transient technique in which heat transfer coefficient are deduced from a time-temperature history recorded. Baughn et al. (1989a) has given a brief history of these techniques. Two recent reviews on the use of liquid crystals in turbulent heat transfer measurement have also been given by Jones (1992) and Baughn (1995). In general, the steady state technique provides a better uncertainty in heat transfer coefficient when it is greater than $200 \text{ W/m}^2\text{K}$. Detailed discussion on the comparison of the accuracy of steady

state, heated coating and transient techniques can be found in Baughn et al. (1989b) and Whitney (1995). But Valencia (1995) presented that the corresponding test surface temperature error by the steady (hot film) technique with liquid crystal thermography may be more than 100% when the tangential heat conduction was neglected. In comparison, the transient technique provided less than 20% of its surface temperature difference. Vedula et al. (1988) found that the effect of lateral conduction on the determination of local convection heat transfer characteristics with transient tests and surface coatings could be less than 5%. Furthermore, Tarasuk and Castle (1983) showed that the electrical power dissipation in a heated wide metallic foil of uniform heater thickness can still be generated 30% higher near the center of the foil than near the foil edge. On the other hand, the transient technique does not require the maintenance of a uniform surface heat flux especially on a larger surface area and therefore there are less limitations on complex model shapes (i.e. curved surfaces), where such nonuniformities are probable. Direct comparisons between measurements made with the steady state method and the transient method can be found in Hippensteele et al. (1983) and Baughn et al. (1989b). Clifford et al. (1983), Metzger and Larson (1986), O'Brien et al. (1986) and Saabas et al. (1987) have widely used this transient technique for very complex geometries, including blade-cooling passages, curved ducts, cylinders and airfoil cooling passages. Based on the above considerations, the transient experimental technique was selected for this investigation.

3.4.2 Analysis of wall transient technique

This technique requires measurement of the elapsed time to increase the surface temperature of the liquid crystals coated on test acrylic specimen from a known initial temperature to predetermined value. The rate of heating is recorded by monitoring the colour change patterns of the liquid crystal with respect to time. The basic principles and data reduction for transient liquid crystal technique were described by Ireland and Jones (1985, 1986) and Ireland (1987). If the specimen is made from a material with low thermal diffusivity (i.e. acrylic material) and chosen to be sufficiently thick, then the heat transfer process can be considered to be one-dimensional into a semi-infinite medium. Schultz and Jones (1973) suggested a criteria for the minimum thickness of material, y , according to Equation (3.8):

$$y > 4\sqrt{\alpha t} \quad (3.8)$$

where y is the thickness of specimen, α is the thermal diffusivity and t is the time.

The governed Equation (3.9) of one-dimensional transient equation:

$$\frac{\partial T}{\partial t} = \alpha \frac{\partial^2 T}{\partial y^2} \quad (3.9)$$

where temperature T is a function of distance y from the surface (through the thickness of the specimen) and time t , i.e. $T(y,t)$. α is thermal diffusivity, y is measured from the surface. The surface temperature was subjected to a hot air jet flow of temperature T_j and a local heat transfer coefficient of h . The following boundary conditions are used in the analysis:

$$\text{Initial condition} \quad : \quad T_{(y,0)} = T_{\text{amb}} \quad (3.10)$$

$$\text{Semi - infinite assumption} \quad : \quad T_{(\infty,t)} = T_{\text{amb}} \quad (3.11)$$

$$\text{Heat flux condition at surface} \quad : \quad q = h[T_j - T_{(0,t)}] = -k \left(\frac{\partial T}{\partial y} \right)_{y=0} \quad (3.12)$$

The solution of the Equation (3.9) subject to the initial and boundary condition is (Kreith and Black, 1980):

$$\frac{T_{(0,t)} - T_{\text{amb}}}{T_j - T_{\text{amb}}} = 1 - \text{erf}\xi - e^{\text{Bi}+\eta} (1 - \text{erf}(\xi + \sqrt{\eta})) \quad (3.13)$$

$$\text{where} \quad \xi = \sqrt{\frac{y^2}{4\alpha t}}, \quad \text{Bi} = \frac{hy}{k} \quad \text{and} \quad \eta = \frac{h^2\alpha t}{k^2} = \frac{h^2 t}{k\rho c} \quad (3.14)$$

At the surface, $y = 0$, thus $\xi = Bi = 0$, and the Equation (3.13) becomes:

$$\frac{T_{(0,y)} - T_{amb}}{T_j - T_{amb}} = \theta = 1 - e^{-\eta} (1 - \text{erf}(\sqrt{\eta})) \quad (3.15)$$

In which the Gaussian error function, erf, is defined as

$$\text{erf}(\sqrt{\eta}) = \frac{2}{\sqrt{\pi}} \int_0^{\sqrt{\eta}} e^{-\xi^2} d\xi \quad (3.16)$$

The exact values of the Gaussian error function, erf, are available from the table provided by Astin (1965). Those values can be evaluated well by using the Simpson rule ($\eta \leq 9$) and Taylor series ($\eta > 9$).

The Simpson rule can be expressed as follows:

$$\text{erf}(\sqrt{\eta}) = \frac{2\Delta y}{3\sqrt{\pi}} \left(\exp(-\xi_0^2) + \exp(-\xi_{2m}^2) + 4 \sum_{m=1}^{2m} \exp(-\xi_{2m-1}^2) + 2 \sum_{m=2}^{2m} \exp(-\xi_{2m-2}^2) \right) \quad (3.17)$$

and

The Taylor series (asymptotic expansion) can be expressed by Gautschi (1954) as follows:

$$\text{erf}(\sqrt{\eta}) = 1 - \frac{1}{\sqrt{\pi\eta}} e^{-\eta} \left[1 - \frac{1}{2\eta} + \frac{3 \cdot 1}{2^2 \eta^2} - \dots - \frac{1 \cdot 3 \cdot 5 \cdot 7 \dots 19 \cdot 21}{2^{11} \cdot \eta^{11}} \right] \quad (3.18)$$

It is also found that the values of Gaussian error function can be more precise when series expansion for Simpson rule are applied up to 100 terms. However, the computed data processing time will increase twofold by using 100 expansion terms instead of 30 terms. Therefore, the 100 expansion terms of Simpson rule are only used in the critical range of $9 \leq \eta \leq 10.65$. Using the numerical calculation for Gaussian error function, the local heat transfer coefficient can be determined when the local surface temperature

information, the jet temperature T_j , initial temperature T_{initial} and the thermal properties of the acrylic specimen are known. Baughn et al. (1989a) found that the radiation could only provide a maximum of 6% of the uncertainty of convective heat transfer information which the surface emissivity might vary with the thickness of the liquid crystal layer. Hence, the radiation correction has not been applied in determining the heat transfer information. The developed transient software program written in Microsoft C language (see Appendix B) was then executed to follow the flow chart as shown in Figures 3.14a, 3.14b, 3.15a and 3.15b.

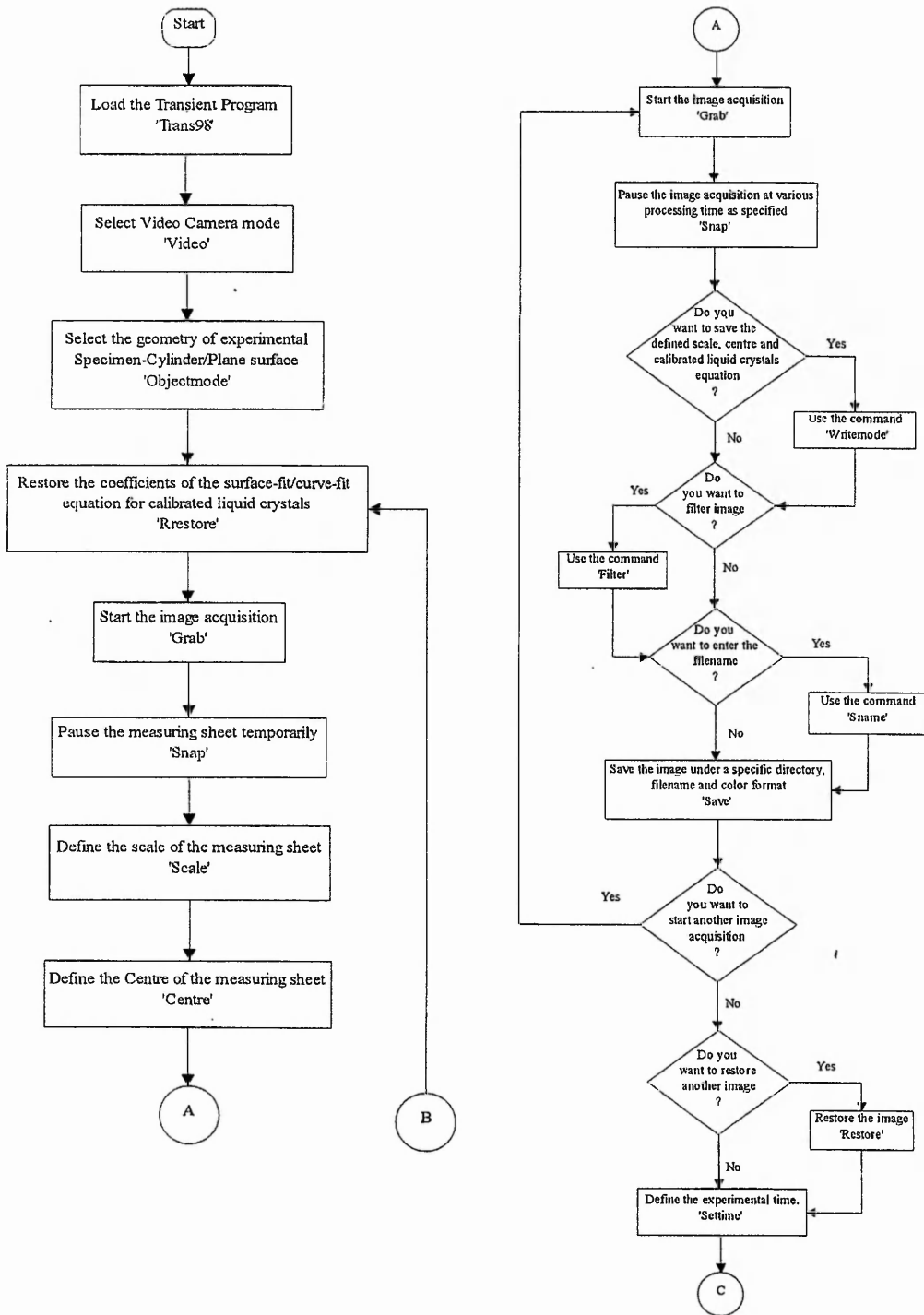


Figure 3.14a Flow chart of the transient program.

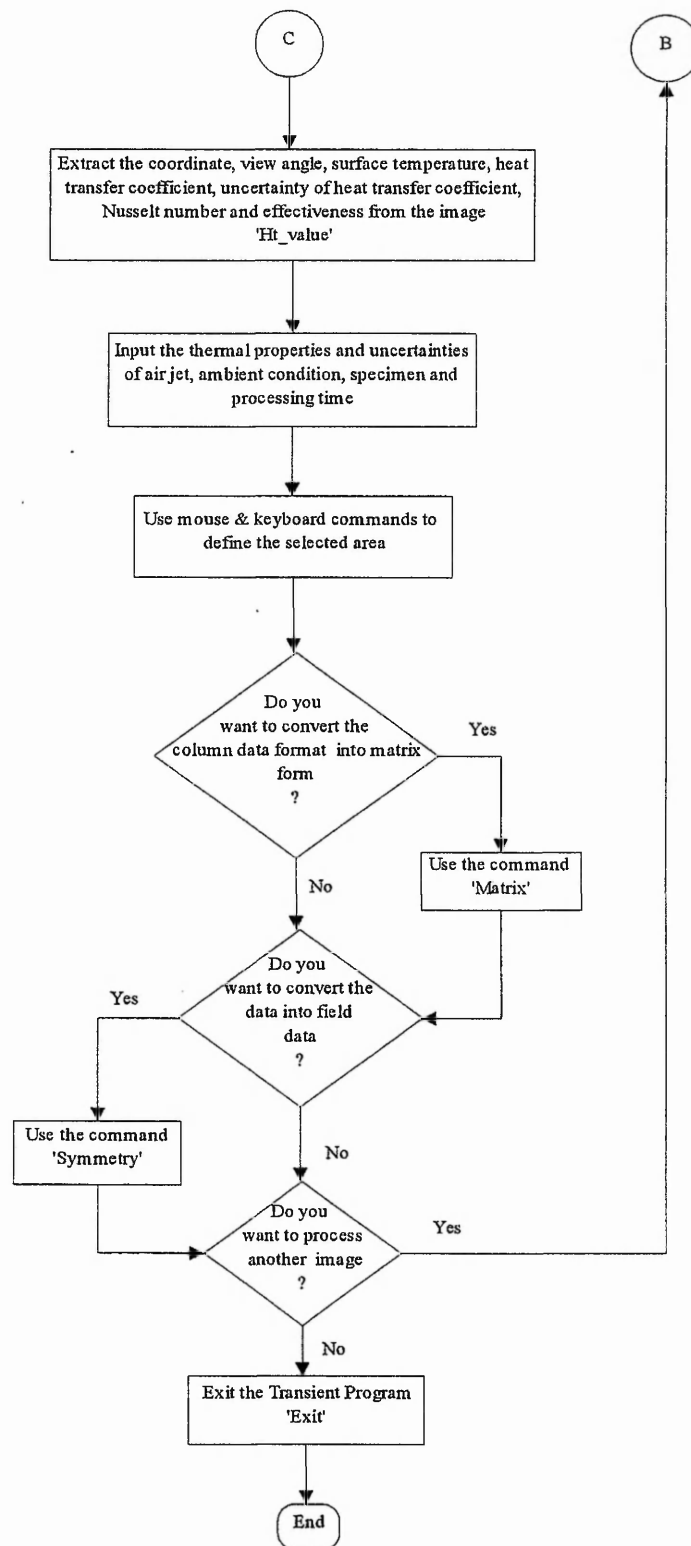


Figure 3.14b Flow chart of the transient program.

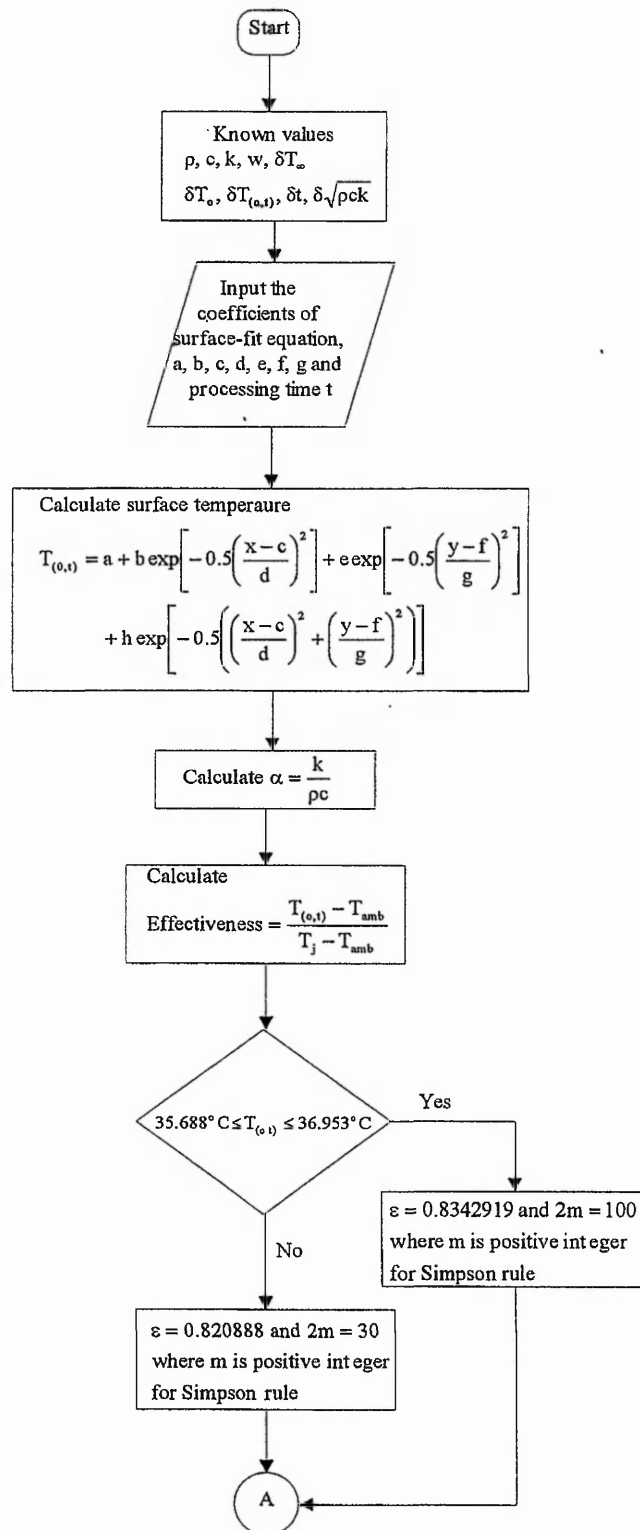


Figure 3.15a Equation flow chart of transient program.

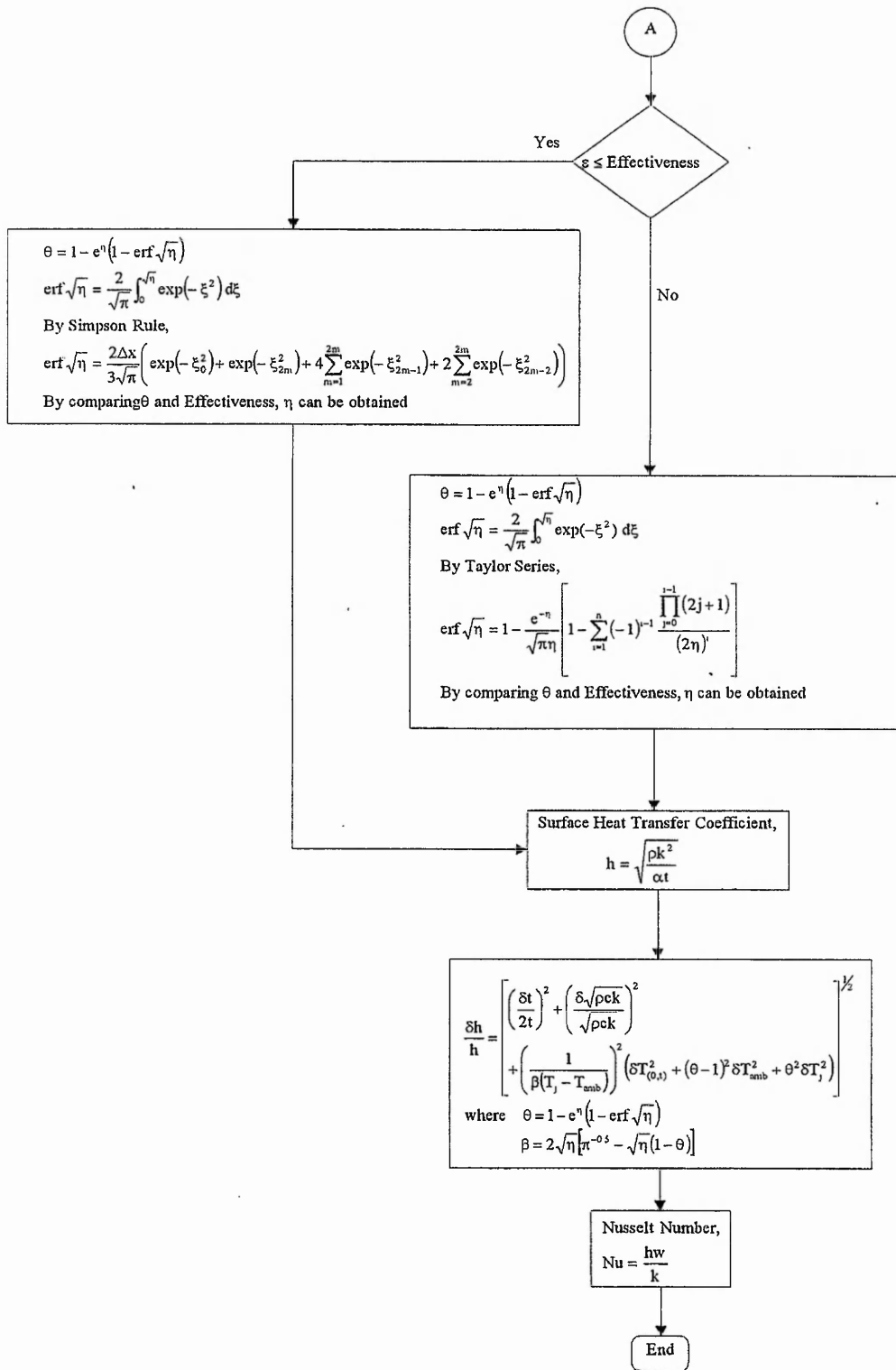


Figure 3.15b Equation flow chart of transient program.

The partial differentiation of the terms of Equation (3.15) and the propagation of the uncertainty in each measured variable through this equation is derived in Appendix C.

$$\frac{\partial h}{h} = \left[\left(\frac{\delta t}{2t} \right)^2 + \left(\frac{\delta(\sqrt{\rho c k})}{\sqrt{\rho c k}} \right)^2 + \left(\frac{1}{\beta(T_j - T_{amb})} \right)^2 \left(\delta T_{(0,t)}^2 + (\theta - 1)^2 \delta T_{amb}^2 + \theta^2 \delta T_j^2 \right) \right]^{0.5}$$

$$\text{where } \beta = 2\sqrt{\eta}[\pi^{-0.5} - \sqrt{\eta}(1 - \theta)] \quad (3.19)$$

The uncertainty in h due to $\delta t/2t$ diminishes as t increases and achieves a maximum for higher values of h . The fractional uncertainty in h due to uncertainty in temperature measurement is a minimum when $\beta(T_j - T_0)$ is large. Selection of the test conditions as described leads to a typical overall uncertainty in heat transfer coefficient, h to be within 10% when the error of video camera viewing angle on the colour interpretation is taken into consideration.

3.4.3 Preparation of the test specimen

A semi-cylinder of acrylic, 150 mm diameter, was used as the impingement target surface. A thin layer of thermochromic liquid crystals was sprayed over a water-based soluble black paint using a pressurized artist's air brush which improves the colour resolution by absorbing unreflected light. The total thickness of the combined layers was estimated to be less than 40 μm with a time response within a few milliseconds by Schultz & Jones (1973). Bonnett (1989) showed that the thermal conductivity and diffusivity of chiral nematic liquid crystals are similar to those of acrylic material, so that the effects due to different thermal resistance have been considered negligible. In addition two thermocouples were placed on the underside of the impingement surface which were used to measure the initial plate temperature (ambient) and validated the semi-infinite assumption.

3.4.4 Experimental set-up and recording procedure

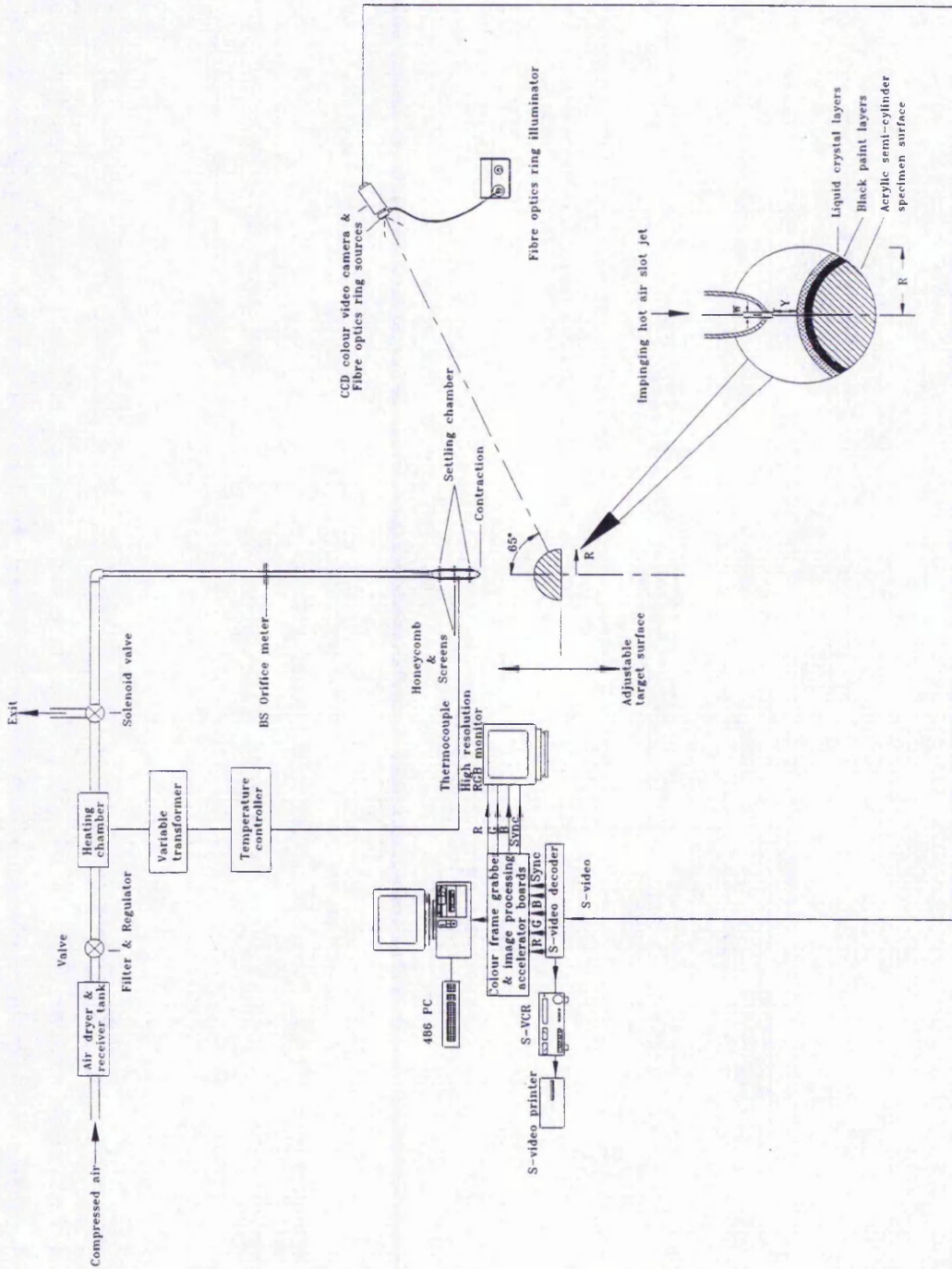


Figure 3.16 Experimental set-up for the heat transfer investigation.

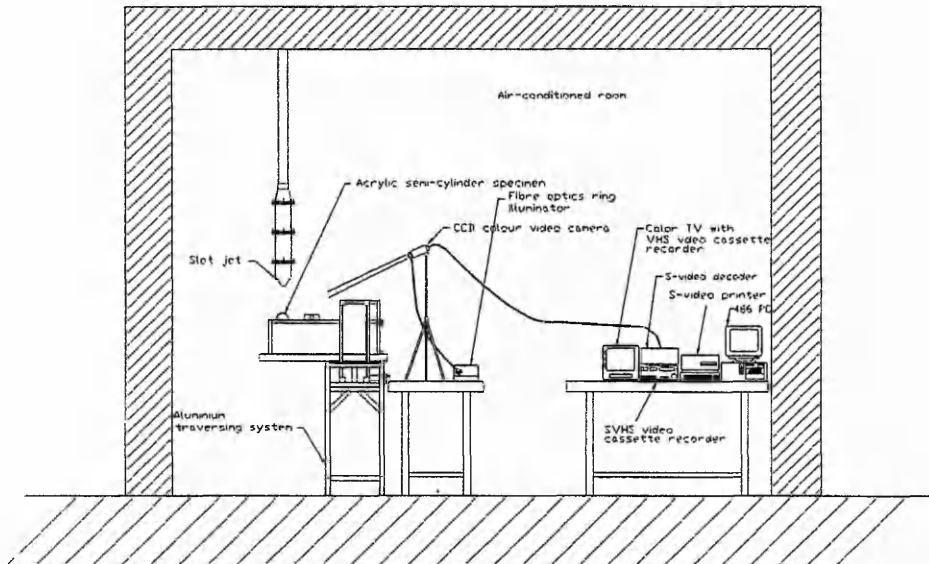


Figure 3.17 Schematic diagram of slot jet experiment.

Figures 3.16 and Figure 3.17 show the experimental set-up for the heat transfer investigation. A hot air slot nozzle system has been discussed in Section 3.2. The required slot jet temperature was set at the temperature controller and a thermocouple feedback loop was employed to maintain a steady air flow temperature at 40 ± 0.2 °C. The solenoid valve was energised from a DC power supply. The change of digital micromanometer pressure reading was used to identify the start time of the test on the recorded video tape. The starting time of video picture can easily be found by the available video picture frame function (40 ms/frame speed) in the professional super video recorder. The time to energise the solenoid valve quoted by the manufacturer was 32.2 ms which was still less than the 40 ms frame speed of the video camera and the duration of the test. The hot air was passed through the pipework and the slot nozzle configuration for a period of time (at least three hours) and the jet exit temperature was allowed to stabilise, which minimised errors due to transient changes in the jet exit temperature caused by losses to the nozzle and plenum chamber. All pipework, and the plenum chamber were well insulated to minimise heat losses during the test. The uniformity of the jet exit velocity was monitored using an orifice plate manufactured to BS1042, connected to a digital micromanometer, allowing measurement of the differential pressure to within 0.1 Pa. The hot air was then diverted by the solenoid to the exhaust position and the impingement specimen at ambient temperature quickly in the right position in place (such as the slot jet-to-

impingement surface distance, Y). Without further delay, the solenoid valve was re-energised to start the test, and the full field liquid crystal thermographs recorded on the super-video tape, which obtained a twofold quality of colour picture in comparing with the ordinary composite video tape.

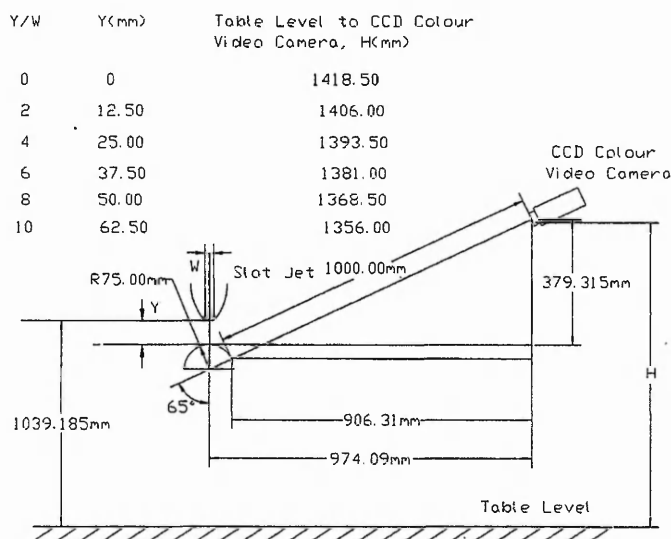


Figure 3.18 Schematic diagram of the arrangement of video camera set up.

The CCD video camera was positioned as shown in Figure 3.18, to record the liquid crystal thermographs from a slot jet impingement to the test specimen (a coated liquid crystal and black paint on a semi-cylinder acrylic with 150 mm diameter), which provided a maximum video camera viewing angle of 68.7° from the impingement stagnation line (see Appendix D).

After the tests the super-video tape was replayed and a colour image processing system, described by Chan et al. (1994 & 1997), was used to analyse the recorded colour images. Super-video pictures can be analysed at intervals of 40 ms, determined by the PAL video camera system, which the full history of surface heat transfer characteristics can be obtained easily. The captured colour liquid crystal thermographic images can then be used to determine the surface temperature (hence heat transfer information) by the developed transient program with the liquid crystal surface-fit equation, discussed in Sections 3.3 and 3.4. Typical liquid crystal thermographs of a heated air slot jet impinging on a semi-cylindrical surface are shown in Figures 3.19a to 3.19d.

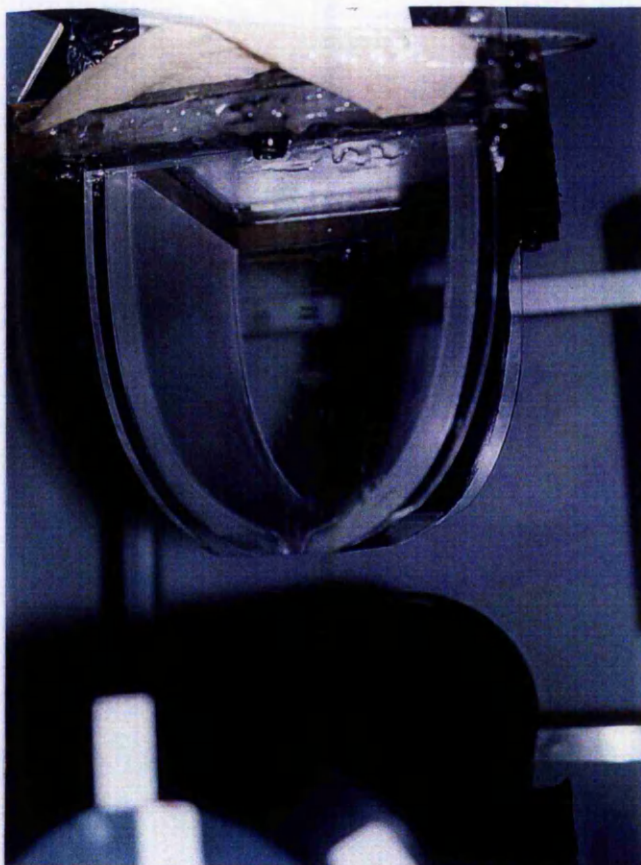


Figure 3.19a
Side view.



Figure 3.19b Front view.

Figures 3.19a and 3.19b Liquid crystal (R30C5W) thermographs of a heated air slot jet impinging on the cylindrical convex surface, $Y/W=5$ and $Re_w=8,500$



Figure 3.19c
Side view.

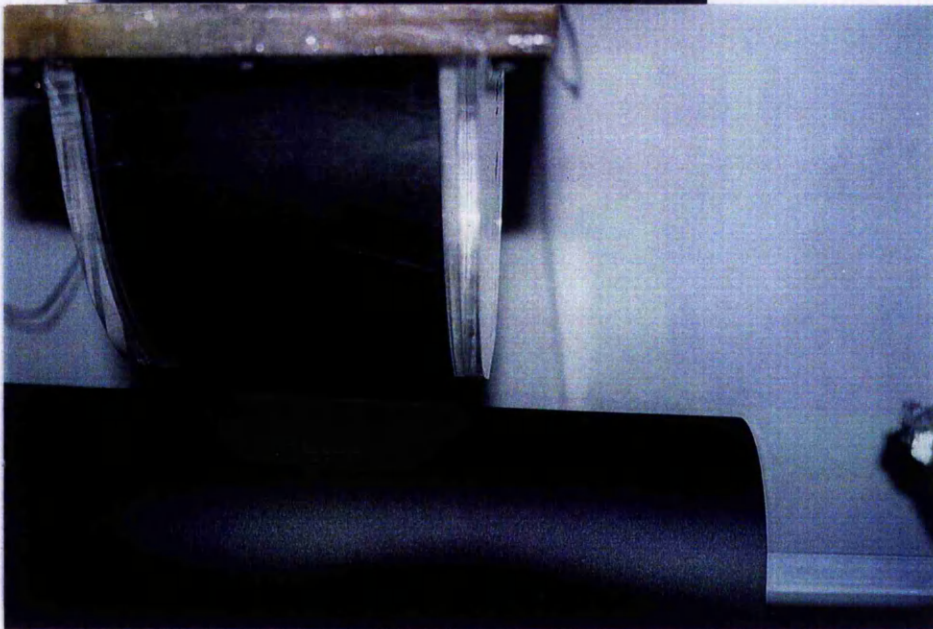


Figure 3.19d Front view.

Figures 3.19c and 3.19d Liquid crystal (R35C5W) thermographs of a heated air slot jet impinging on the cylindrical convex surface, $Y/W=5$ and $Re_w=8,500$

3.5 Summary of Chapter

The design, development and validation of the experimental rigs, the procedures adopted for hot-wire anemometry system, liquid crystal calibration system and automatic non-intrusive liquid crystal thermography for surface heat transfer measurement system based on colour image processing system have been described. The transient wall heating technique was selected for liquid crystal thermography for a heated slot jet impingement tests based on experimental uncertainty analysis and the complex geometrical surface (i.e. convex surface). The preparation of the test specimens, the experimental set-up and recording procedures using a colour image processing system. The overall uncertainty in the measured heat transfer coefficient is calculated to be within 10% in the test conditions, if the error of video camera viewing angle on the colour (or hue) interpretation is taken into consideration.

Chapter 4 Numerical Investigation

4.1 The Governing Equations of Motion

For an incompressible, two-dimensional, steady state turbulent impinging jet, the governing equations in cartesian coordinates (Bird et al., 1960) can be described by the full Navier-Stokes equations and the continuity equation:

Equation of motion in y-direction:

$$\rho \left(u \frac{\partial v}{\partial x} + v \frac{\partial v}{\partial y} \right) = -\frac{\partial p}{\partial y} + \mu \frac{\partial}{\partial x} \left(\frac{\partial v}{\partial x} + \frac{\partial u}{\partial y} \right) + \frac{\partial}{\partial y} \left(2\mu \frac{\partial v}{\partial y} \right) \quad (4.1)$$

Equation of motion in x-direction:

$$\rho \left(u \frac{\partial u}{\partial x} + v \frac{\partial u}{\partial y} \right) = -\frac{\partial p}{\partial x} + \mu \frac{\partial}{\partial y} \left(\frac{\partial v}{\partial x} + \frac{\partial u}{\partial y} \right) + \frac{\partial}{\partial x} \left(2\mu \frac{\partial u}{\partial x} \right) \quad (4.2)$$

Continuity equation:

$$\frac{\partial}{\partial x}(\rho u) + \frac{\partial}{\partial y}(\rho v) = 0 \quad (4.3)$$

These are exact equations and form a closed set describing all the details of fluid motion where the variables represent instantaneous values. The time-averaging process is most clearly explained for stationary turbulence. For such a flow, the instantaneous velocities and pressure can be expressed as the sum of mean (time-averaged) and a fluctuating part of variables, so that:

$$u = U + u'; \quad v = V + v'; \quad p = P + p' \quad (4.4)$$

Using time-averaged quantities in Navier-Stokes, the governing equations become:

Equation of motion in y-direction:

$$\rho \left(U \frac{\partial V}{\partial x} + V \frac{\partial V}{\partial y} \right) = -\frac{\partial P}{\partial y} + \frac{\partial}{\partial x} \left(\mu \left(\frac{\partial V}{\partial x} + \frac{\partial U}{\partial y} \right) - \rho \overline{u'v'} \right) + \frac{\partial}{\partial y} \left(2\mu \frac{\partial V}{\partial y} - \rho \overline{v'^2} \right) \quad (4.5)$$

Equation of motion in x-direction:

$$\rho \left(U \frac{\partial U}{\partial x} + V \frac{\partial U}{\partial y} \right) = -\frac{\partial P}{\partial x} + \frac{\partial}{\partial y} \left(\mu \left(\frac{\partial V}{\partial x} + \frac{\partial U}{\partial y} \right) - \rho \overline{u'v'} \right) + \frac{\partial}{\partial x} \left(2\mu \frac{\partial U}{\partial x} - \rho \overline{u'^2} \right) \quad (4.6)$$

Continuity equation:

$$\frac{\partial}{\partial x} (\rho U) + \frac{\partial}{\partial y} (\rho V) = 0 \quad (4.7)$$

This set of averaged equations is only closed when the Reynolds shear stress terms $\overline{u'v'}$; can be solved through the use of a turbulence model.

4.2 Closure of Averaged Equations

The k- ϵ model (Jones and Launder, 1972 and Launder and Spalding, 1972) used in the present study is that built into the PHOENICS code which determine the Reynolds stresses through the mean rate strain of the Boussinesq eddy viscosity concept which is given by

$$-\rho \overline{u'v'} = \mu_t \left(\frac{\partial U}{\partial y} + \frac{\partial V}{\partial x} \right) - \frac{2}{3} \rho k \delta_{ij} \quad (4.8)$$

The turbulent or eddy viscosity μ_t is found from $\mu_t = \frac{\rho C_\mu k^2}{\epsilon}$, where k and ϵ are the turbulent kinetic energy and its rate of dissipation respectively. The two transport equations used for the solutions of k and ϵ can be deduced from the Navier-Stokes equations (Tennekes and Lumley, 1972):

$$\rho \left(U \frac{\partial k}{\partial x} + V \frac{\partial k}{\partial y} \right) = \frac{\partial}{\partial x} \left(\frac{\mu_t}{\sigma_k} \frac{\partial k}{\partial x} \right) + \frac{\partial}{\partial y} \left(\frac{\mu_t}{\sigma_k} \frac{\partial k}{\partial y} \right) + S_k \quad (4.9)$$

$$\rho \left(U \frac{\partial \varepsilon}{\partial x} + V \frac{\partial \varepsilon}{\partial y} \right) = \frac{\partial}{\partial x} \left(\frac{\mu_t}{\sigma_\varepsilon} \frac{\partial \varepsilon}{\partial x} \right) + \frac{\partial}{\partial y} \left(\frac{\mu_t}{\sigma_\varepsilon} \frac{\partial \varepsilon}{\partial y} \right) + S_\varepsilon \quad (4.10)$$

$$S_k = P_k - \rho \varepsilon \quad (4.11)$$

$$S_\varepsilon = C_1 \frac{\varepsilon}{k} P_k - C_2 \rho \frac{\varepsilon^2}{k} \quad (4.12)$$

$$P_k = \mu_t \left[\left(\frac{\partial U}{\partial y} + \frac{\partial V}{\partial x} \right)^2 + 2 \left(\left(\frac{\partial U}{\partial x} \right)^2 + \left(\frac{\partial V}{\partial y} \right)^2 \right) \right] \quad (4.13)$$

4.3 The Energy Equation

For a two-dimensional, steady state turbulent impinging jet flow, the energy equation reads

$$\frac{\rho}{c_p} \left(U \frac{\partial h}{\partial x} + V \frac{\partial h}{\partial y} \right) = \frac{\partial}{\partial x} \left(\frac{\mu_t}{c_p \sigma_t} \frac{\partial h}{\partial x} \right) + \frac{\partial}{\partial y} \left(\frac{\mu_t}{c_p \sigma_t} \frac{\partial h}{\partial y} \right) \quad (4.14)$$

$$\frac{\rho}{c_p} \left(U \frac{\partial H}{\partial x} + V \frac{\partial H}{\partial y} \right) = \frac{\partial}{\partial x} \left(\frac{\mu_t}{c_p \sigma_t} \frac{\partial H}{\partial x} - \rho \overline{u' h'} \right) + \frac{\partial}{\partial y} \left(\frac{\mu_t}{c_p \sigma_t} \frac{\partial H}{\partial y} - \rho \overline{v' h'} \right) \quad (4.15)$$

The constants in k-ε model are listed in Table 4.1. These values were chosen after extensive examination of free turbulent flows by Launder and Spalding (1974).

C_μ	C_1	C_2	σ_k	σ_ε
0.09	1.44	1.92	1.0	1.3

Table 4.1 Constants used in the k-ε turbulence model.

4.4 The Near Wall Function

In the immediate vicinity of the impingement surface where the direct viscous effects are influential, the logarithmic law of wall is selected for bridging within this region. The logarithmic law of the wall was used to compute the skin friction which is used to determine the Stanton number. The well-known wall function approach (Rosten and Worrell, 1988) for turbulent boundary layers was adapted and its further details are given by the CHAM Ltd. (1991). Since the PHOENICS code does not provide any heat transfer information directly as a standard option but gives the skin friction, Stanton number and other computed physical variables had to be output into a result file using appropriate GROUND coding provided in Appendix E. When the local Reynolds number $Re > 132.5$, the skin friction can be determined by:

$$s = \left(\frac{\kappa}{\ln(1.01 + 9 Re s^{0.5})} \right)^2 \quad (4.16)$$

where κ is the von Karman constant, 0.435. Otherwise,

$$s = \frac{1}{Re} \quad (4.17)$$

The heat flux to the near wall is computed from

$$St = \frac{-q}{(h_p - h_w) \rho v_p} = \frac{s}{\sigma_t (1 + Ps^{0.5})} \quad (4.18)$$

where

$$P = 9 \left(\frac{\sigma_t}{\sigma_t} - 1 \right) \left(\frac{\sigma_t}{\sigma_t} \right)^{0.25} \quad (4.19)$$

This equation was originally developed by Jayatilleke (1969). Nusselt number can be calculated according to the definition given in Chapter 3, where h_p , h_w , T_p and T_w

denote the computed enthalpies and temperatures at the near wall node and the wall respectively.

4.5 Numerical Solution Procedure

To solve the governing equations, a fully staggered grid system is adopted for the velocity components at the face of the grid cells and the scalar variables at the grid points. These equations are discretised using a control finite volume method, applying a staggered grid arrangement to overcome the oscillatory pressure and velocity fields. It was introduced by Patankar and Splading (1972) and then elaborated in detail by Patankar (1980). A hybrid upwinding scheme was used for discretisation of the combined effects of convection and diffusion terms in the equations. In order to determine the approach in which the convection and diffusion terms in the momentum equations are handled, this scheme is calculated in the local cell Peclet number, Pe (or local cell Reynolds number): if the Pe is two or less, central differences are used; and if the Pe is greater than 2, upwinded differences are employed (Patankar, 1980). The solution procedure used the commercially available PHOENICS computer code version 2.2 based on the SIMPLEST (Semi-Implicit Method for Pressure Linked Equations Shortened) solution algorithm of Splading (1991). The u-momentum and v-momentum equations are solved to obtain the velocity field, then the pressure correction equation is solved simultaneously. Finally the velocity and pressure are corrected, then the turbulent kinetic energy, dissipation rate, and energy equations are solved sequentially using the TDMA (TriDiagonal-Matrix Algorithm) line solver.

The general form of the algebraic governing equations obtained from discretisation can be given as follows:

$$a_p \phi_p = a_E \phi_E + a_W \phi_W + a_N \phi_N + a_S \phi_S + b_\phi \quad (4.20)$$

where the a 's are the coefficients of the convection and diffusion terms. E, W, N and S denote as the grid locations at the east, west, north and south sides of nodal point, P respectively, and b is the discretised source term.

4.6 The Grid Dependency

Cylindrical-polar grids were used to allow the distribution of grid points very close to the cylindrical surface (impingement surface). In the course of the free slot jet modelling, only half of the jet was modelled owing to its symmetrical geometry. The grid was distributed with different cell sizes in the y direction and x , azimuthal (streamwise) direction where the finest cell sizes were near the front stagnation region and impingement surface region respectively as shown in Figure 4.1. To verify the algorithm, the predicted velocity profiles were studied to ensure that the computational solution were grid independent. A coarse 27×55 grid system is first generated, then the grid resolution was doubled to 54×110 and 68×110 grid systems to represent half of the semi-cylinder (from the front stagnation point, 0° to the azimuthal/streamwise (θ) direction, 92°) on the case $Y/W=2$ and $Re_w=13,200$. In this case, the size of the grid cells (ranging from $0.01W$ to $0.04W$) within a $0.28W$ from the impingement surface were addressed.

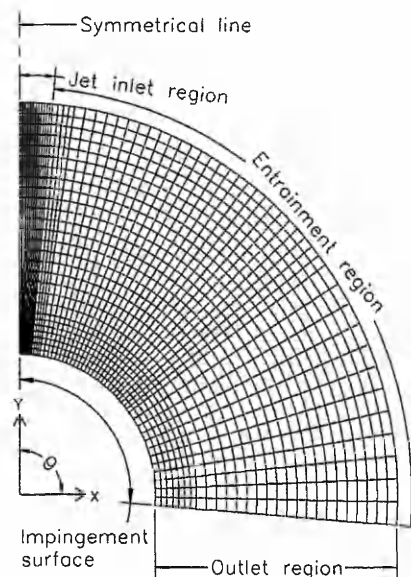


Figure 4.1 Typical schematic diagram of 27×55 grid system used for $Y/W=2$ computation.

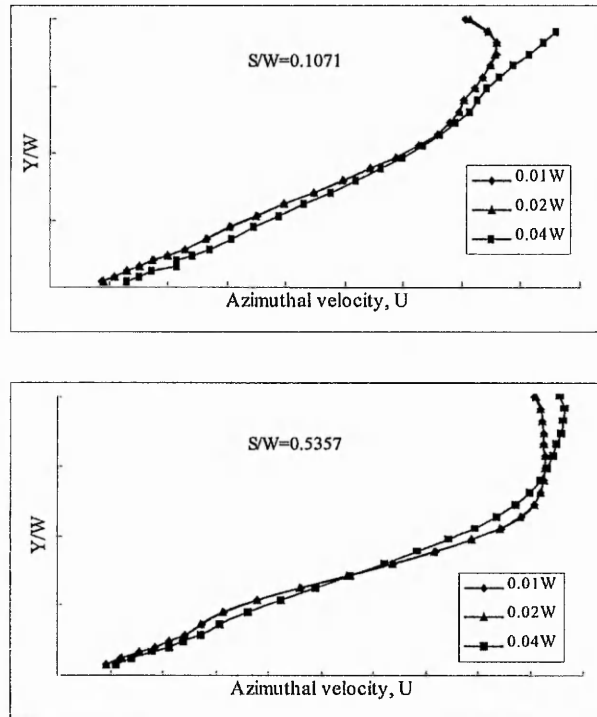


Figure 4.2 Grid dependency performance tests at $S/W= 0.1071$ and 0.5357 .

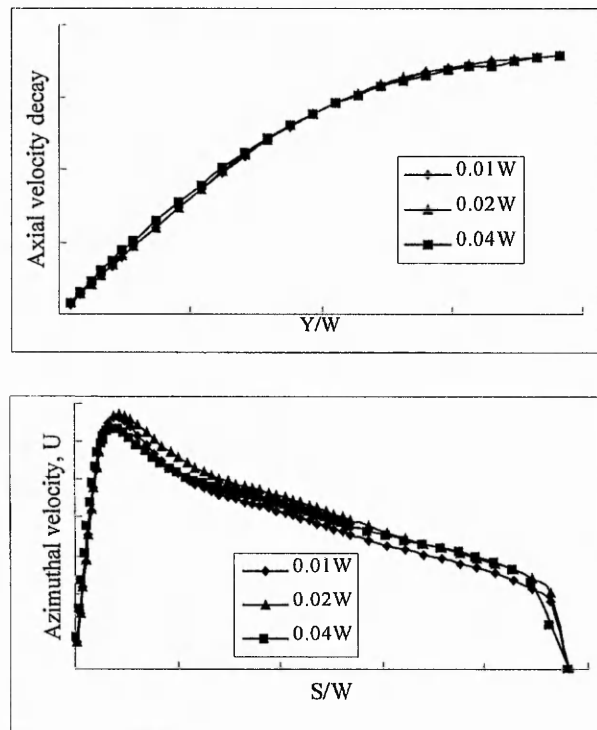


Figure 4.3 Grid dependency performance tests at the axial and azimuthal velocities.

Figure 4.2 and 4.3 show the dependence of velocity and velocity gradient on the near wall cell sizes. Results corresponding to the $0.01W$ grid are not shown as distinguishable from those of the $0.02W$ grid. The development of the axial velocity is shown little dependence on the near wall cell sizes. The azimuthal velocity profiles however show a significant dependence at small azimuthal distance from the jet axis due to the large velocity gradients in this stagnation region. The change in the predicted velocity gradient with near wall cell sizes is given in Table 4.2. In Figure 4.4, the computed maximum turbulent kinetic energy errors were 19% at $S/W=0.1071$ and 12% at $S/W=0.5357$ when compared between a 54×110 ($0.02W$ near wall cell size) and a 68×110 ($0.01W$ near wall cell size) grid systems. The improvement obtained with the $0.01W$ grid cell size was not significant when compared to the computational time/cost of using the $0.02W$ grid cell size. In addition, it is assumed that this near wall cell size lies within a turbulent region when the wall function is activated. The computed non-dimensional distance from the wall y^+ , showed that a near wall cell size of $0.02W$ would satisfy this criterion in the stagnation region. Hence all numerical results reported in Chapter 5 were chosen an accurate near wall cell size.

Near wall cell size	% difference with the finest grid cell
$0.04W$	21
$0.02W$	1.3
$0.01W$	0

Table 4.2 Percentage error associated with near wall cell sizes (ranging from $S/W=0.1071$ to $S/W=0.5357$).

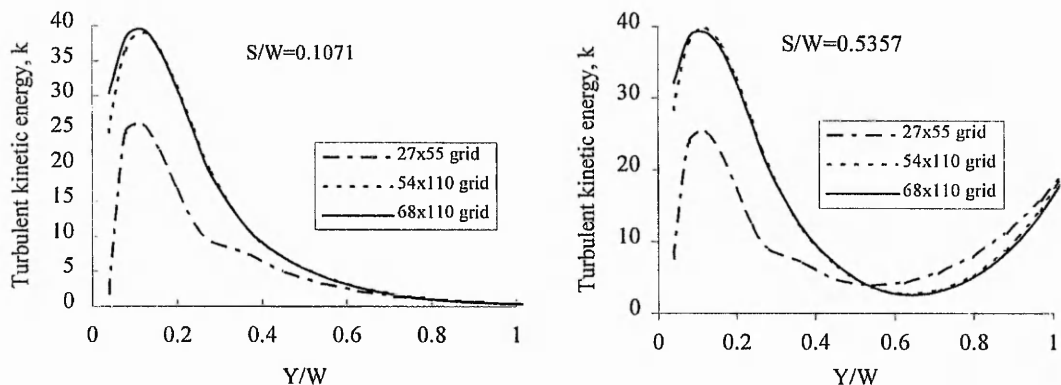


Figure 4.4 Near wall turbulent kinetic energy for different grid systems.

4.7 Initial and Boundary Conditions

In the elliptic nature of the flow field, equations require boundary conditions specified over a completely closed boundary of the solution domain. Measured uniform velocity and turbulence intensity, obtained using hot wire anemometry and presented in Chapter 5, and temperature were specified at the slot nozzle exit. Symmetry boundary conditions were used at jet centerline axis. The value of turbulent kinetic energy of the jet inlet was deduced from $k = 0.5(u'^2 + v'^2)$, Shaw (1992) and the value of turbulent dissipation rate at the inlet was deduced from $\varepsilon = \frac{C_\mu^{0.75} k^{1.5}}{L}$ where L is the characteristic length scale, CHAM Ltd. (1991). Zero velocities were specified at the impingement surface and a logarithmic wall function was activated which was proposed by Launder and Spalding (1974). A floating zero were specified at the outlet and entrainment boundaries where the computed pressure domain is relative to it. The use of SAME command in the PHOENICS Input Language (PIL) ensured that the inflowing mass brings in the same value of the physical variable as already prevails at the specified cell. Ambient temperature was specified at the impingement surface as the initial boundary condition. All other physical properties such as viscosity, thermal conductivity, specific heat capacity and density were assumed to be independent of temperature in the computed domain.

4.8 Convergence

Ideally, a set of numerical equations are said to be convergent if such a solution tends towards the analytical solution in a defined problem. However, in most real problems, there is no analytical/exact solution that can be determined in order to compare with the numerical solution. In PHOENICS code, a number of devices are provided to control the convergence of the numerical solution. A convergence monitoring device can be used to monitor the trend of residuals in particular spot values during the iterative run. Linear relaxation and false time-step underrelaxation are the most commonly used device to promote convergence as described by CHAM Ltd. (1990). The relaxation factors were applied to promote smooth convergence of the discretised equations. The amount of relaxation varied during the iterative process (i.e. pressure:

0.2 to 0.8 and other physical variables depending on the grid system and cell size). In addition, greater relaxation has been applied to the turbulent quantities. Maximum and minimum values for the variables and initial values were also specified according to the experimental conditions. The sums of the absolute residuals of the numerical equations were used to monitor the overall convergence. For each 1000 sweeps (iterations), the numerical solution were required to use approximately 1 to 3 hours CPU time when the slot jet-to-impingement surface separation ratio, range from $Y/W= 2$ to $Y/W= 10$. All cases were computed on the Pentium MMX200 PC with 64Mb Ram.

4.9 Summary of Chapter

The governing equations of motion and equations for the $k-\varepsilon$ turbulence model are described. The discretisation methods are used to require a very fine grid cell sizes near the solid wall in order to produce substantial small numerical solution errors. The grid was finest in those regions where the physical property gradients would be expected to be very large. However, it has been demonstrated that a considerable numerical errors are obtained even with very fine grids, when a high density of cells, are used in these critical regions. By careful consideration of the grid systems and an acceptable trade-off of accuracy against computational time/cost, $S/W= 0.0536$ cell size in the x-direction and an accurate near wall cell size in the y-direction was finally adopted within the stagnation and near the impingement wall regions. Grid dependency study was used to reduce numerical errors as far as possible.

Chapter 5 Presentation and Discussion of Experimental and Numerical Results

5.1 Introduction

The effects of jet Reynolds numbers, and the separation distance between the impingement surface and the jet nozzle on local circumferential heat transfer from a turbulent impinging hot air slot jet on a semi-cylinder convex surface have been studied. The results obtained also cover range of geometries that are relevant to both the previous work and industry. The jet Reynolds number Re_w ranges from 5,600 to 13,200 and the dimensionless slot jet nozzle-to-impingement surface separation distance (Y/W) ranges from 2 to 10. The major emphasis of this work is to provide more comprehensive heat transfer data regarding the effects of Re_w and Y/W on the impingement heat transfer distribution along a semi-cylinder surface, and correlations of both the stagnation point, local and average Nusselt number over the circumferential distribution. Finally, comparisons of experimental results are also made to the predicted results using the standard $k-\epsilon$ turbulence model. Every effort has been made to compare results with previously published relevant research works.

5.2 Slot Nozzle Measurement

5.2.1 Slot nozzle contraction design

The contraction to the slot nozzle was designed with a BASIC computer program developed by Button and Leech (1972). The contraction area ratio was 20:1, giving a reduction in area from 125 mm x 125 mm to 6.25 mm x 125 mm, i.e. the slot nozzle exit area. The cross-sectional dimensions of slot nozzle were 6.25 mm (W) x 125 mm (L), which gave an aspect ratio of 20, without significant end effects. The contraction length was calculated to be 153.24 mm, and was made convergent and curved smoothly, which allowed rapid acceleration of fluid without occurrence of flow separation and generation of turbulence. To ensure the air stability, a settling chamber with a honeycomb and meshes was used to minimise the turbulence intensity and maintain a uniform air flow at the exit. Therefore, a uniform velocity profile associated

with relatively low turbulence intensity across the nozzle width at the exit was obtained. The contraction profile co-ordinate is presented in Appendix A.

5.2.2 Flow characteristics at the slot nozzle exit

The streamwise turbulence intensity at the slot nozzle exit was measured with a hot-wire anemometer and was found to be around 1% turbulence intensity for the jet Reynolds number, Re_w ranging from 5,600 to 13,200. To ensure that the length of the nozzle, L would not affect the slot jet flow, the nozzle was made long enough in the direction perpendicular to nozzle axis, namely 125 mm. Experiments were run at a number of levels of nominal jet Reynolds number, Re_w , for which the corresponding values of slot nozzle exit mean velocity, V , were tabulated as shown in Table 5.1. Air viscosity and density for Re_w were evaluated at the nozzle exit temperature. The flow could be considered incompressible since the maximum value of nozzle exit velocity did not exceed Mach number of 0.3.

W (mm)	L (mm)	Re_w	V (m/s)
6.25	125	5,600	15.2
		8,500	23.1
		13,200	35.8

Table 5.1 Flow parameters of a single heated air impinging slot jet.

Measurements of axial mean velocity and axial fluctuating velocity, v' , were made mainly on the middle nozzle as well as along the slot nozzle length. Axial mean, V and fluctuating velocity profiles, v' , across the nozzle width, normalised respectively to V and V_{CL} were measured at nozzle exit, $Y/W=0$. The flat profile desired are clearly shown in Figures 5.1a, 5.1b and 5.1c. With respect to mean axial velocity profiles at the slot nozzle exit, they were flat and uniform to within 3% over approximately the central 90% of the slot nozzle width, and dropping very sharply to almost zero near the nozzle wall. The turbulence intensity profiles across the nozzle width were found to be around 1% intensity in the central region, and rising to about 2% at the nearest location to the nozzle wall. Similar, slot jet exit velocity and turbulence intensity profiles were reported in Whitney (1995).

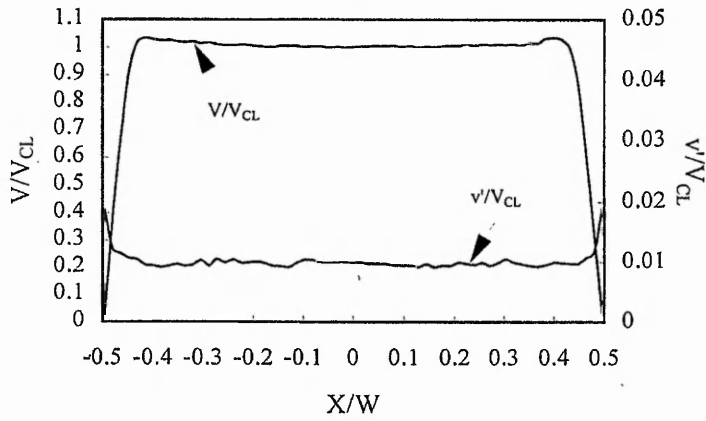


Figure 5.1a Velocity and streamwise turbulence intensity profiles across the slot nozzle width, $Re_w = 5,600$.

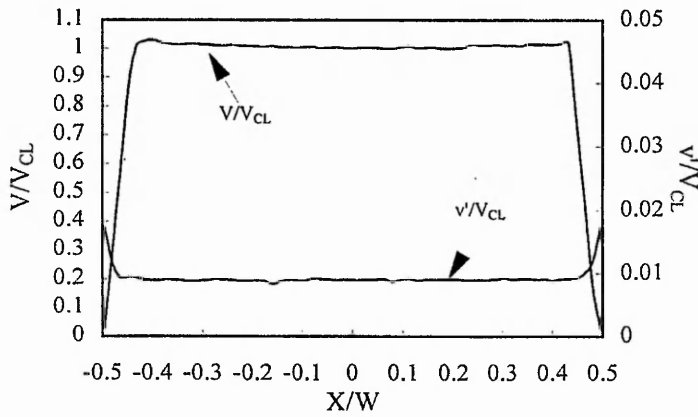


Figure 5.1b Velocity and streamwise turbulence intensity profiles across the slot nozzle width, $Re_w = 8,500$.

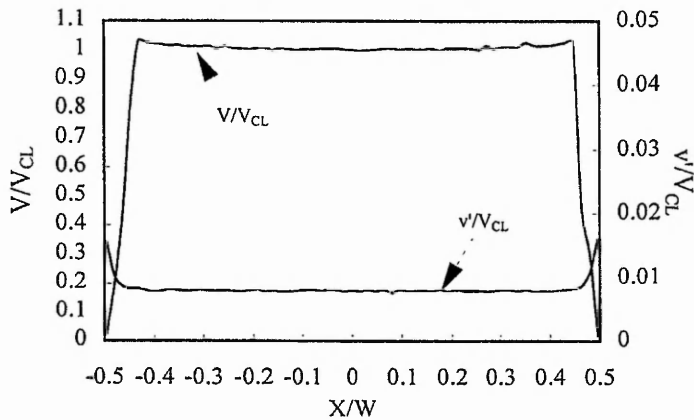


Figure 5.1c Velocity and streamwise turbulence intensity profiles across the slot nozzle width, $Re_w = 13,200$.

5.3 Heat Transfer Results

The surface heat transfer information was determined by the wall transient technique on the captured liquid crystal thermographic images from the recorded super-video tape. Detailed discussion of the wall transient technique and colour image processing procedure can be found in Section 3.4. Local heat transfer information will be related to the flow characteristics of slot nozzle width exit presented previously, throughout the discussion where appropriate.

5.3.1 Liquid crystal thermographic images

The applications of liquid crystal thermographic techniques have shown that quantitative as well as qualitative results can be obtained. Some insight into thermal propagation due to a heated air slot jet impingement on a semi-cylindrical convex surface can be given by a series of thermal visualization images at various Y/W and Re_w obtained with a liquid crystal thermographic technique as shown in Figures 5.2a to 5.2c. Note that only one half of the cylindrical surface is shown due to the symmetric setup. The highest temperature (in dark blue/blue contour) was observed at the stagnation region directly beneath the impinging slot jet, and decreasing gradually along the circumferential direction to the lowest temperature (in red contour). The liquid crystal thermographic images can be captured from a real time or a recorded super-video tape and then processed into useful heat transfer information as described in the Sections 3.3 & 3.4.

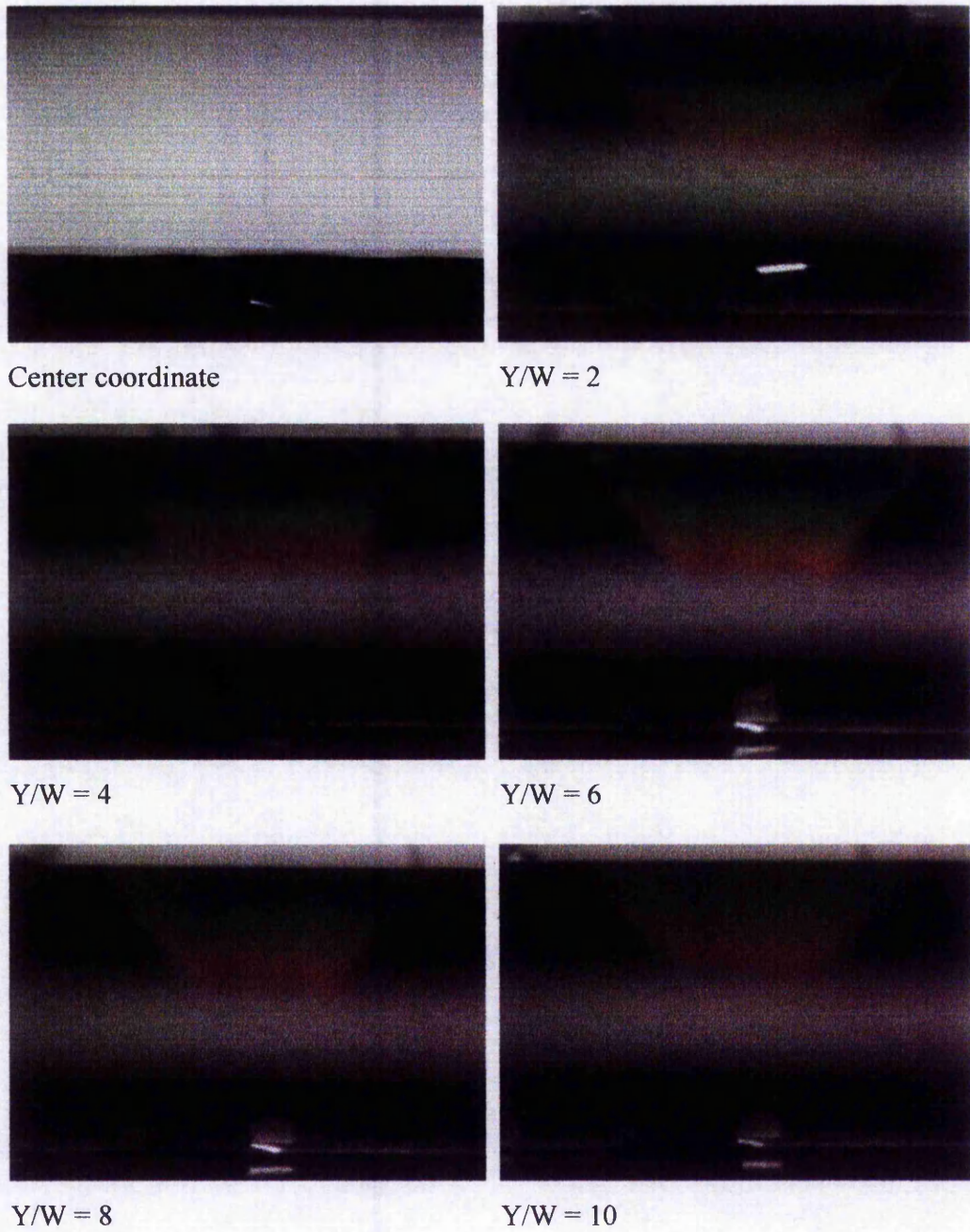


Figure 5.2a Thermal visualization of a heated air slot jet impinging on a semi-cylinder convex surface, $Re = 5,600$.

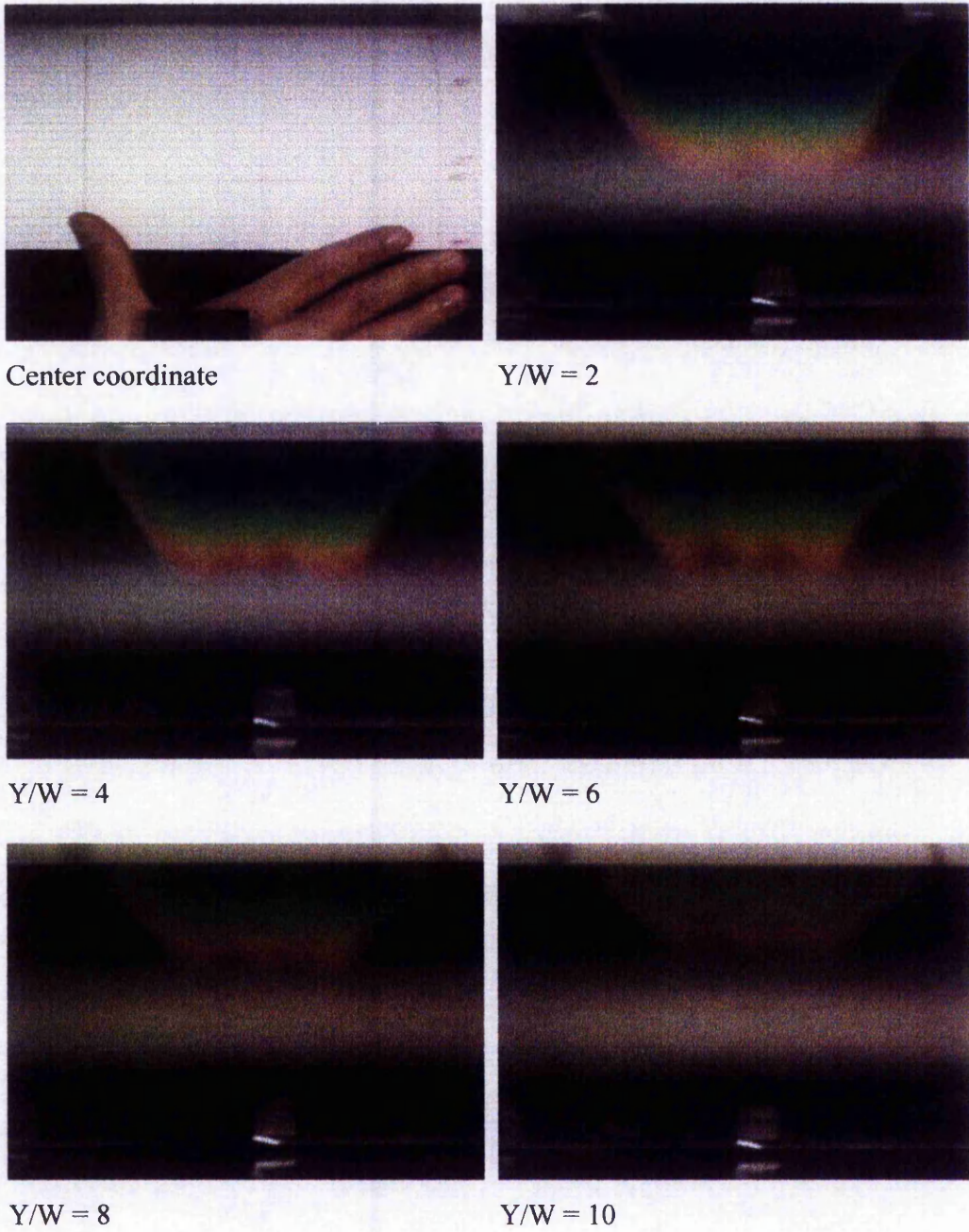


Figure 5.2b Thermal visualization of a heated air slot jet impinging on a semi-cylinder convex surface, $Re = 8,500$.

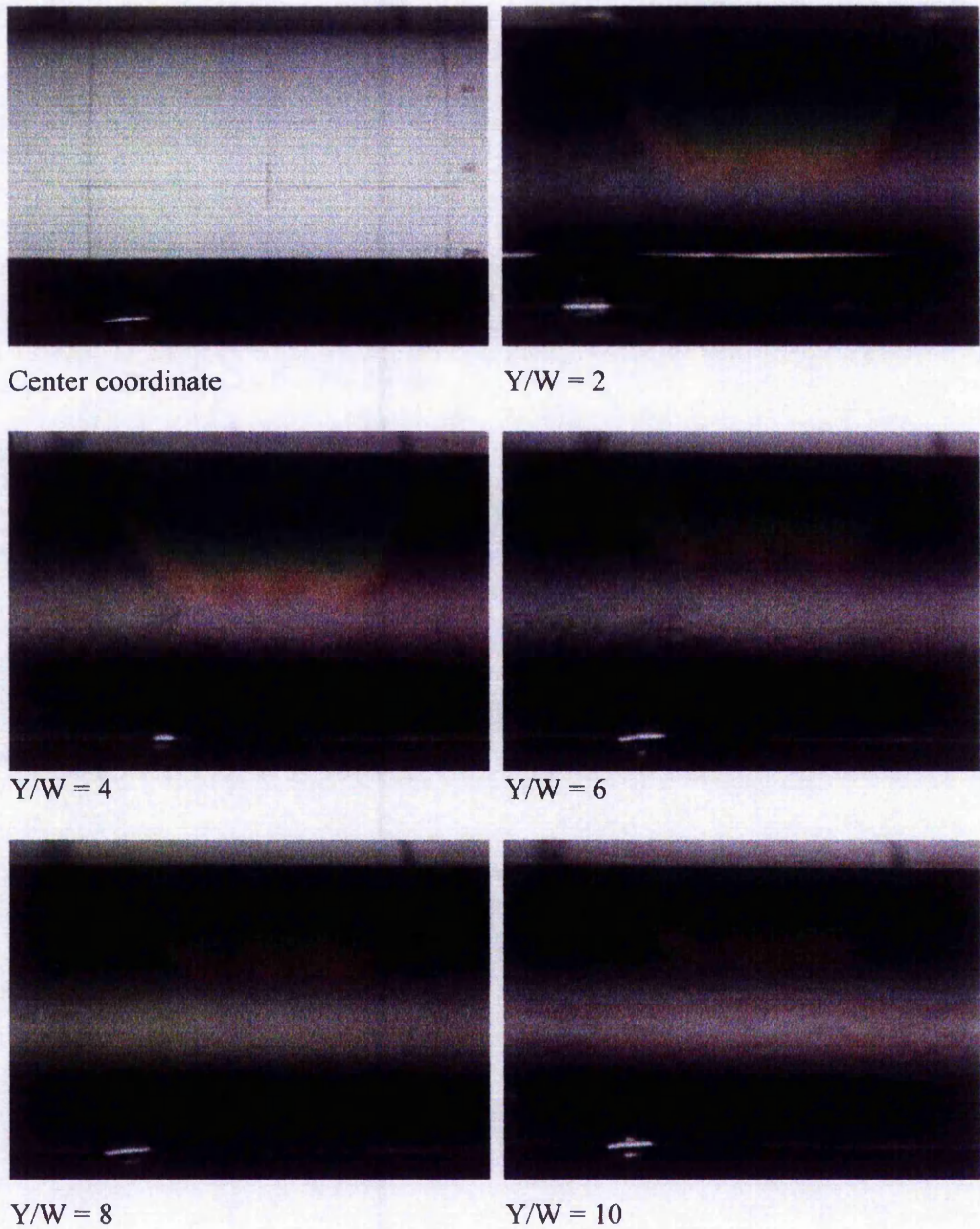


Figure 5.2c Thermal visualization of a heated air slot jet impinging on a semi-cylinder convex surface, $Re = 13,200$.

5.3.2 Heat transfer characteristics at the stagnation point

5.3.2.1 Effect of Reynolds number

The stagnation point heat transfer is of particular interest for heating, cooling and/or drying purposes because of its relatively high heat transfer rate. The stagnation point Nusselt number (Nu_0) versus the dimensionless slot nozzle-to-impingement surface spacings (Y/W) at various Reynolds number Re_w is plotted in Figure 5.3. The stagnation point Nusselt number increases monotonically for a given Reynolds number.

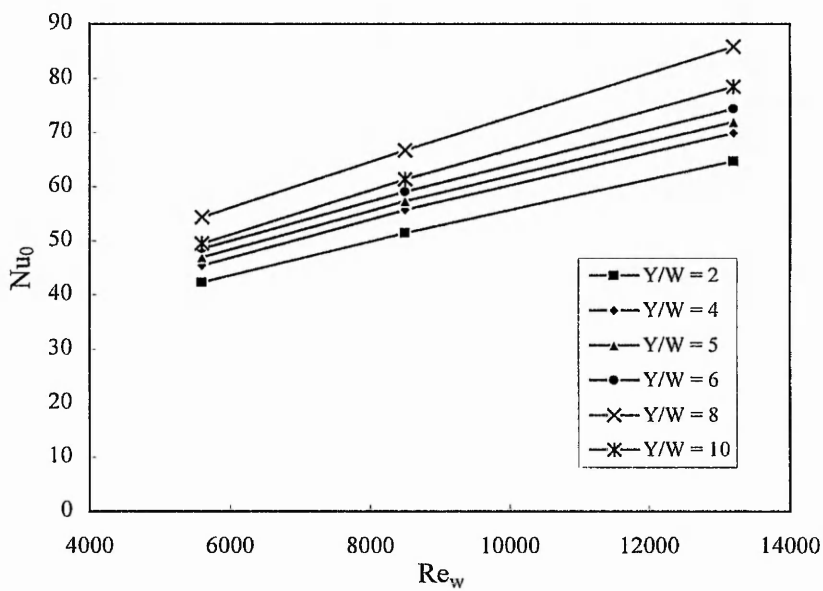


Figure 5.3 Effect of Reynolds number on the stagnation point Nusselt number.

Since all experiments in the present study were conducted with air and the Prandtl number for air is almost constant over the temperature range used. Correlations of Nu_0 in terms of the Reynolds number, Re and slot jet-to-impingement surface distance, Y/W are then obtained as follows:

For $2 \leq Y/W < 8$,

$$Nu_0 = 0.514 Re_w^{0.5} \left(\frac{Y}{W} \right)^{0.124} \quad \text{with a calculated standard deviation of } < 1\%. \quad (5.1)$$

For $8 \leq Y/W \leq 10$,

$$Nu_0 = 1.175 Re_w^{0.54} \left(\frac{Y}{W} \right)^{-0.401} \quad \text{with a calculated standard deviation of } <1\%. \quad (5.2)$$

The above correlations are valid for $5,600 \leq Re_w \leq 13,200$. Schlichting (1979) and Martin (1977) have stated that the Nusselt number at the stagnation region should be $Nu_0 \propto Re^{0.5}$ for laminar boundary-layer flow for the smaller slot nozzle-to-impingement surface distances of $Y/W = 2$ to 6 . Figure 5.3 shows a good agreement with one-half power of Reynolds number correlation ($Nu_0 \propto Re^{0.5}$). For the longer slot nozzle-to-impingement surface spacing of $Y/W > 6$, the Reynolds number dependence is stronger ($Nu_0 \propto Re^{0.54}$) because these spacings are beyond the potential core region and air entrainment effect on the jet momentum takes place. Gardon and Akfirat (1965) have discussed in detail the flow phenomena which affect the stagnation heat transfer coefficients. The results agree with the experimental Reynolds number correlation from Gau and Chung (1991) and Lee et al. (1997) for the convex surface case. This information is useful for design purposes if the oblique surface heat transfer rate can be maximised for a single slot impinging jet.

5.3.2.2 Effect of slot jet-to-impingement surface separation distance

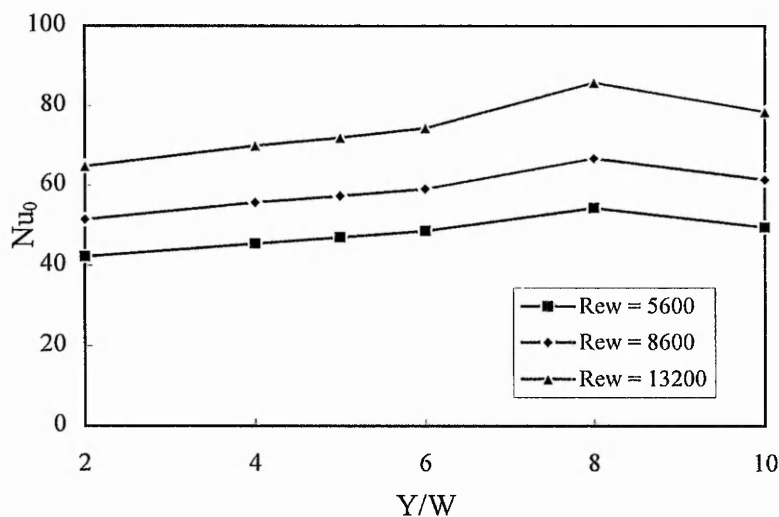


Figure 5.4 Effect of slot jet-to-impingement surface separation distance.

It can be seen from Figure 5.4 that Nu_0 gradually increases with Y/W and reaches a maximum of $Y/W=8$. A similar non-linear increase Nu_0 behaviour for increasing Y/W or Y/d is also found in the slot air jet impinging on an isothermal hot flat surface experiments of Gardon and Akfirat (1966) performed at $450 \leq Re \leq 50,000$ and $0.5 \leq Y/W \leq 80$, the round hot gas jet impinging on an isothermal plane surface experiments of Popiel et al. (1980) performed at $Re=1,050$ and $1,860$, and $2 \leq Y/d \leq 20$, the slot air jet impinging on a heated semicylindrical convex surface experiments of Gau and Chung (1991) performed at $6,000 \leq Re \leq 35,000$ and $2 \leq Y/W \leq 16$, an axisymmetric air jet impinging on a heated hemispherically convex surface experiments of Lee et al. (1997) performed at $11,000 \leq Re \leq 50,000$ and $2 \leq Y/d \leq 10$, and a submerged slot air on a circular cylinder performed at $78,000 \leq Re \leq 178,000$ and $2.2 \leq Y/W \leq 20$. Lee et al. (1997) showed that the potential core length of the free jet increased with increasing Reynolds number and remained roughly at the same magnitude of turbulence intensity in the potential core region. According to the descriptions by Livingood and Hrycak (1973), the extent of the potential core zone is 6 to 7 diameters for the axisymmetric jets and 4 to 7.7 slot widths for slot jets, although a wider range is also found from other investigators. It should also be noted that the turbulence intensity increases drastically beyond the potential core region due to more active exchange of momentum with surrounding ambient air, but decays slowly in the fully developed jet region. Ashforth-Frost et al. (1997) and Lee et al. (1997) found that the maximum Nusselt number at the stagnation point occurred at $Y/d \cong 6$ to 8 and $Y/W=9.2$, respectively. Whitney (1995) stated that the longer potential core and developing zones was mainly due to the confinement plate blocking the ingress of air from behind the semi-confined jet exit case. The experimental correlations of Nu_0 in terms of Reynolds number Re and the slot jet-to-impingement separation distance Y/W are referred to in Section 5.3.2.1.

Figure 5.5 shows the comparison between the stagnation Nusselt number of present data and the relevant published correlated data or experimental data available for a slot/circular jet impinging on a convex/flat surface.

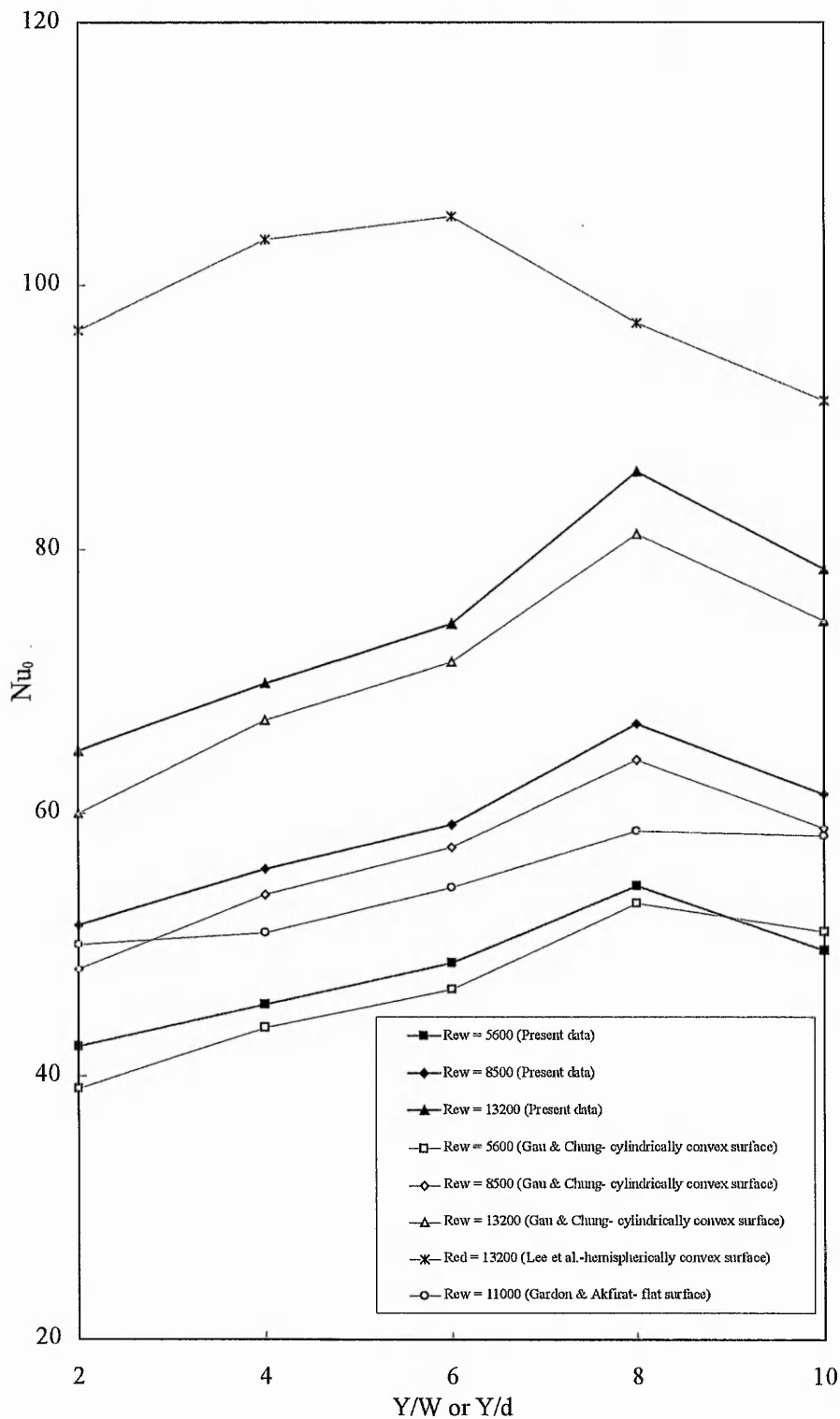


Figure 5.5 Comparison of the stagnation Nusselt number between present data for a semi-cylindrical convex surface and the published correlations the convex surfaces and flat surface.

The present results have good repeatability and are in good agreement with the correlated data obtained from Gau and Chung (1991) under similar conditions. The higher correlated Nu_0 data for Lee et al (1997) is probably attributed to the higher circular jet turbulence intensity ($Tu \sim 3.5\%$) at the nozzle exit and its jet exit velocity profile, which can significantly increase the stagnation heat transfer rate. The stagnation Nusselt number reaches a maximum of $Y/d = 6$ for the correlated $Re_d = 13,200$. Scholtz and Trass (1970) have also shown that the difference between a flat and a parabolic jet exit velocity profile can cause a deviation in the stagnation mass transfer coefficients of a factor of two for low Reynolds number circular impinging jets. On the other hand, the results obtained from Gardon and Akfirat (1996) are much lower than the present study. Becko (1976) stated that 20% extra correction on their results should be applied due to some experimental errors. Taking account of this experimental correction, a reasonable agreement can be made. It also shows that Nusselt number at the stagnation is less dependent of the target surface geometry.

5.3.3 Heat transfer characteristics along the semi-cylindrical convex surface

5.3.3.1 Effect of Reynolds number

Circumferential distributions of the local Nusselt numbers for different Reynolds numbers Re along the axis of the semi-cylinder surface are presented in Figures 5.6a to 5.6e. In each figure, the local Nusselt number Nu is plotted as a function of the dimensionless circumferential distance S/W , with $S/W = 0$ corresponding to the centerline of the slot impinging jet. According to the figures, the local Nusselt numbers increase with increasing Reynolds number. The local Nusselt numbers decrease with increasing the circumferential distance S from its maximum value at the stagnation point due to a presumed laminar boundary layer development up to $S/W = 3.1$ where transition in the boundary layer from laminar to turbulent flow occurs and it causes an increase in the local Nusselt numbers. This transition is completed at about $3.3 \leq S/W \leq 4.2$ where the second peak occurs in this region. But it is noted that the maximum Nu occurred at $S/W \cong 0.21$ from the centerline of the jet for $Y/W \leq 4$ in Figures 5.6a and 5.6b. A similar slot jet behaviour is also found at $Y/W = 4$ from Whitney (1995). This occurrence is due to the slot nozzle exit which gives a flat velocity profile indicating that the centerline turbulence level has not reached a fully

developed region. The turbulence level in the shear layer at the jet boundary is higher than on the jet centerline as shown in Figures 5.1a to 5.1c. This higher turbulence level causes a small increase in the Nusselt number just adjacent to the centerline of the jet. Pamadi and Belov (1980) have shown that the mechanism leading to the occurrence of the inner peak is due to the strong influence of mixing-induced and non-uniform turbulence in the developing jet. When the impingement surface is placed beyond the potential core region, the jet flow arriving the impingement is highly turbulent mixing due to the influence of the ambient air entrainment process. The circumferential Nusselt number distribution are shown in a bell shape in Figures 5.6d and 5.6e.

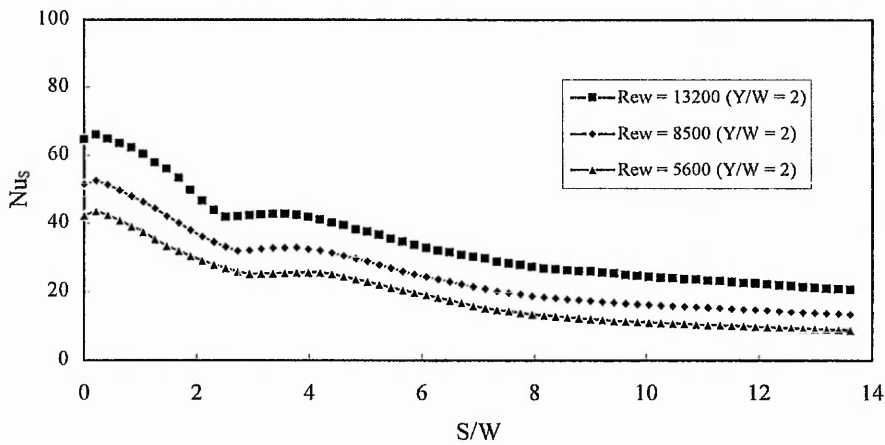


Figure 5.6a Circumferential Nusselt number distributions for different Re_w on the impingement surface at $Y/W=2$.

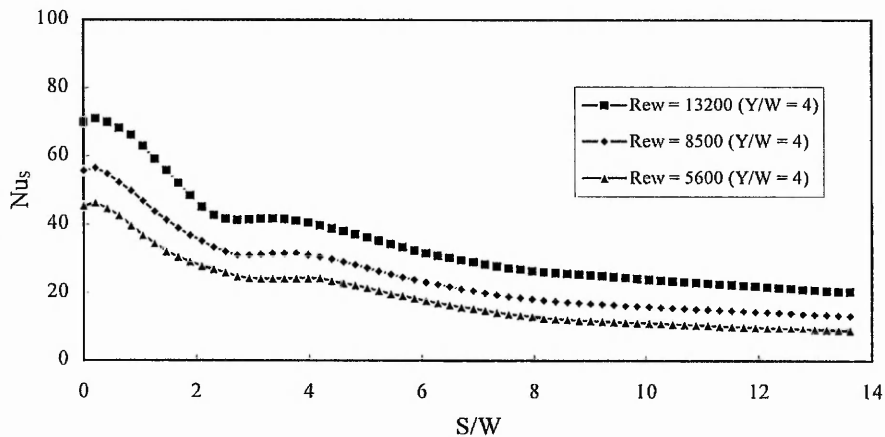


Figure 5.6b Circumferential Nusselt number distributions for different Re_w on the impingement surface at $Y/W=4$.

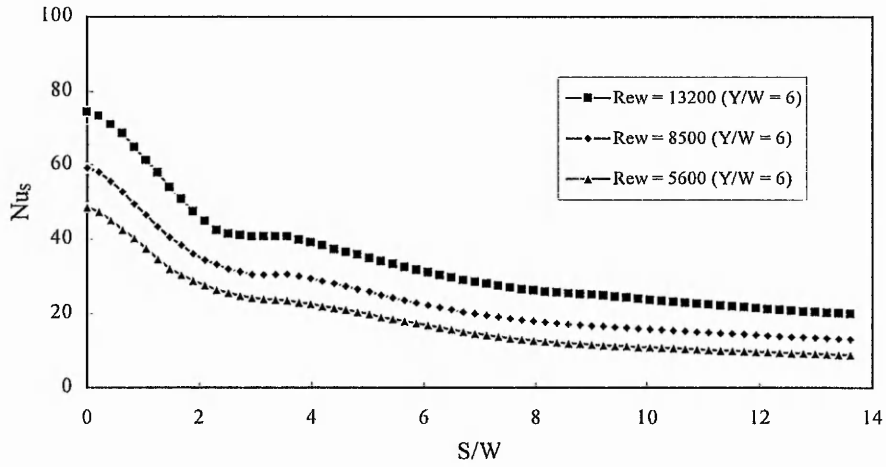


Figure 5.6c Circumferential Nusselt number distributions for different Re_w on the impingement surface at $Y/W=6$.

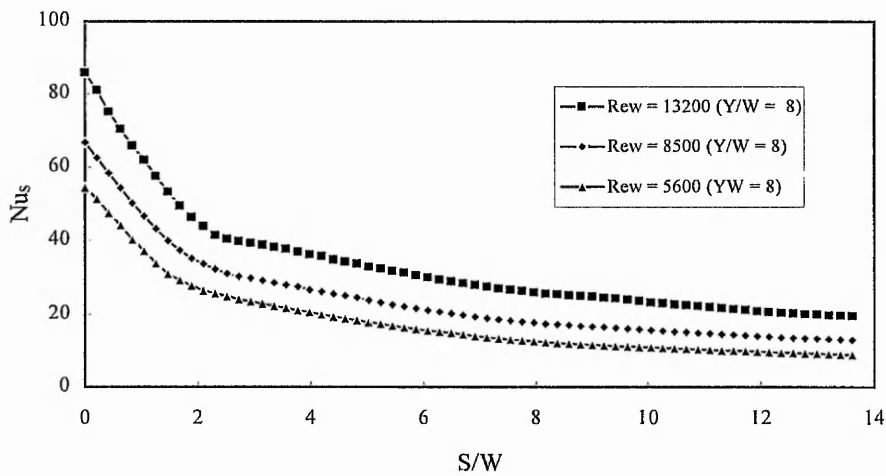


Figure 5.6d Circumferential Nusselt number distributions for different Re_w on the impingement surface at $Y/W=8$.

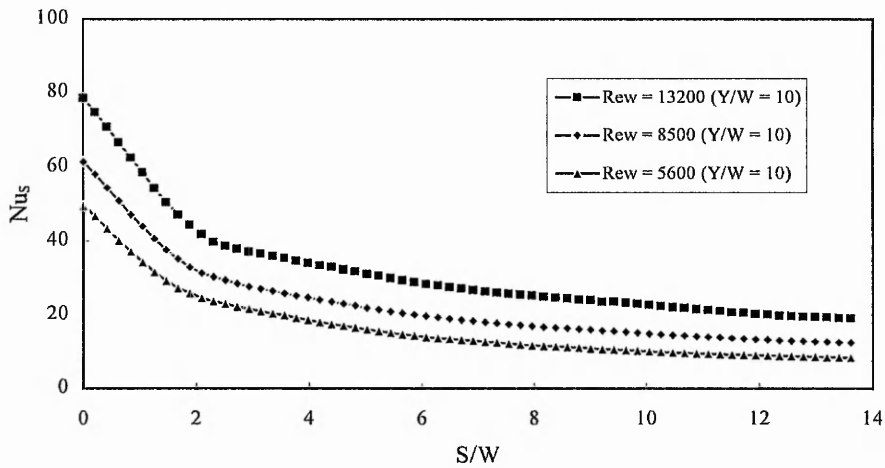


Figure 5.6e Circumferential Nusselt number distributions for different Re_w on the impingement surface at $Y/W=10$.

Around the circumferential Nusselt number distribution, the experimental data were correlated as follows:

For $2 \leq Y/W < 8$ and $0 \leq S/W \leq 13.6$ in Figures 5.6a to 5.6c,

$$\frac{Nu_s}{Nu_0} = 1.068 - 0.310\left(\frac{S}{W}\right) + 0.079\left(\frac{S}{W}\right)^2 - 0.012\left(\frac{S}{W}\right)^3 + 0.001\left(\frac{S}{W}\right)^4 - 2.141 \times 10^{-5}\left(\frac{S}{W}\right)^5$$

with a calculated standard deviation of 13.6%. (5.3)

For $8 \leq Y/W \leq 10$ and $0 \leq S/W \leq 13.6$ in Figures 5.6d and 5.6e,

$$\frac{Nu_s}{Nu_0} = 1.016 - 0.393\left(\frac{S}{W}\right) + 0.1\left(\frac{S}{W}\right)^2 - 0.013\left(\frac{S}{W}\right)^3 + 0.001\left(\frac{S}{W}\right)^4 - 2.089 \times 10^{-5}\left(\frac{S}{W}\right)^5$$

with a calculated standard deviation of 10.4%. (5.4)

The above correlations are valid for $5,600 \leq Re \leq 13,200$.

5.3.3.2 Effect of slot jet-to-impingement surface separation distance

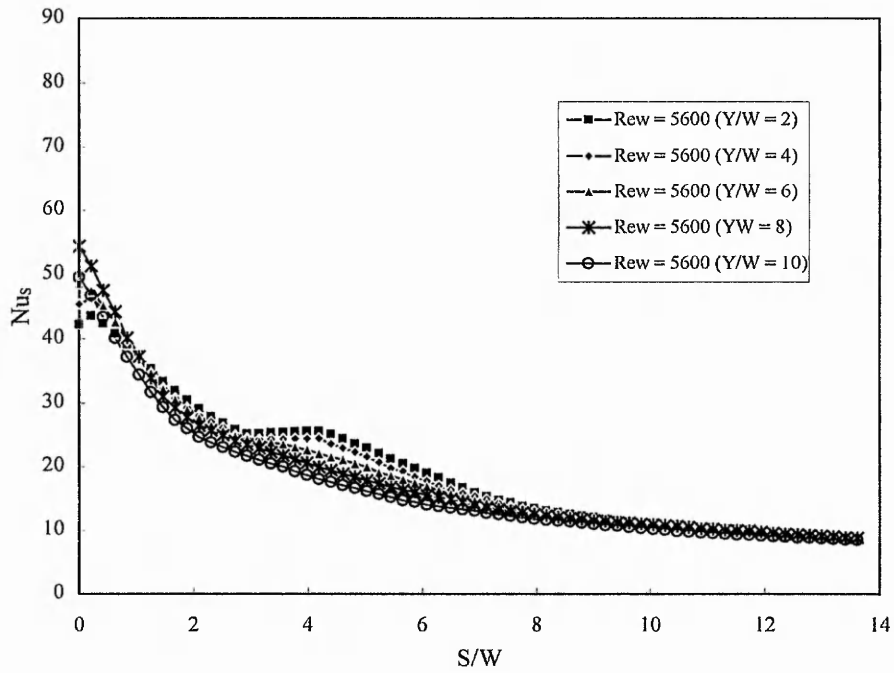


Figure 5.7a Circumferential Nusselt number distributions for different Y/W on the impingement surface at $Re_w = 5,600$.

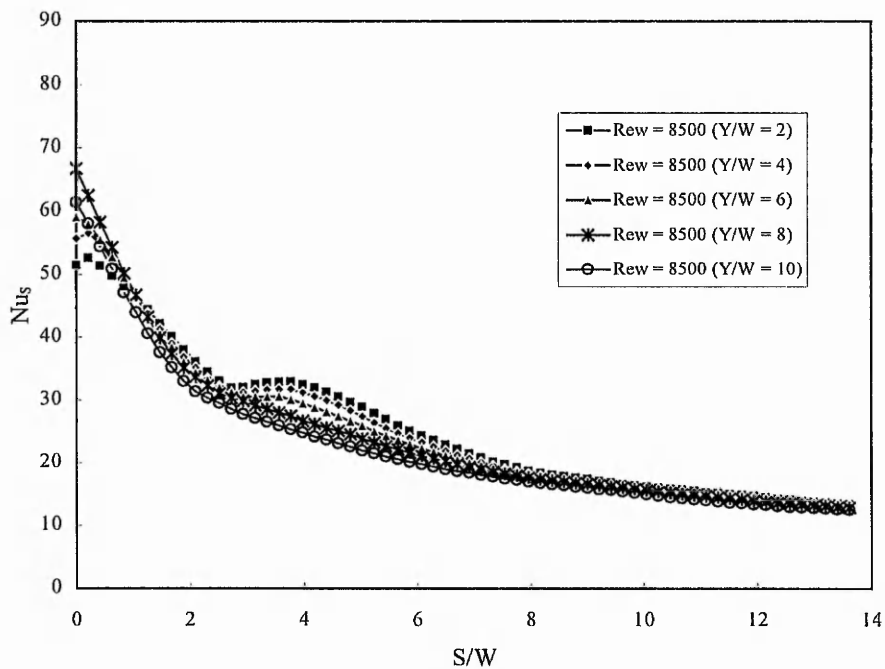


Figure 5.7b Circumferential Nusselt number distributions for different Y/W on the impingement surface at $Re_w = 8,500$.

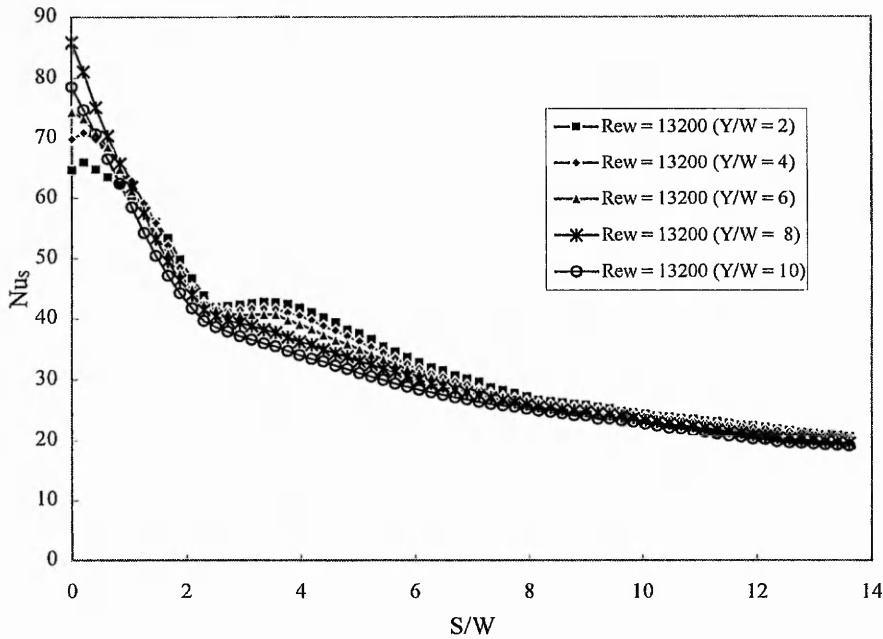


Figure 5.7c Circumferential Nusselt number distributions for different Y/W on the impingement surface at $Re_w = 13,200$.

Figures 5.7a to 5.7c correspond to increasing the parameter of dimensionless separation distance Y/W from 2 to 10 for three Reynolds numbers. In general, the circumferential local Nusselt numbers decreases from the stagnation point in respect to the parameters of Re_w and Y/W . For $Y/W = 2$ and 4 at low $Re_w = 5,600$, the transition starts to take place at $2.9 \leq S/W \leq 3.2$ and attain secondary peak (turbulent heat transfer) at $S/W \cong 4.2$. For $Y/W = 2$ and 4 at high $Re_w = 13,200$, the transition starts to place at $2.5 \leq S/W \leq 2.7$ and reach the secondary peak at $S/W \cong 3.4$. It is shown that the transition occurs sooner and is completed in a shorter circumferential distance for higher Reynolds number. The findings of Cadek and Zerkle (1974) and Lee et al. (1997) tend to support this observation in a different target geometry (i.e flat and convex cylindrical/hemispherical surfaces). When the impingement surface is placed beyond the potential core region, the jet flow arriving at impingement is highly turbulent and mixing due to the influence of the ambient air entrainment. The circumferential Nusselt number distribution are shown in a bell shape in Figures 5.6d and 5.6e. Beyond the circumferential distance S/W of about 9 slot width, the local Nusselt numbers are almost independent of the impingement surface distance with

respect to the studied Reynolds numbers Re_w . This behaviour could also indicate the existence of a fully developed wall jet at these locations. For $Y/W \geq 8$, all figures showed that the secondary peak almost disappear due to the stagnation region turbulence effects.

5.3.4 Comparison with the average Nusselt number on the semi-cylindrical convex surface and flat surface

Becko (1976) stated that the average Nusselt number over the circumferential local Nusselt number data is more desirable because such value is less sensitive to experimental errors and thus more reliable for engineering design. The average Nusselt numbers are then correlated in term of Re_w and Y/W over the circumferential distance S/W as follows:

For $2 \leq Y/W < 8$ and $0 \leq S/W \leq 13.6$,

$$Nu_{ave} = 0.514 Re_w^{0.5} \left(\frac{Y}{W}\right)^{0.124} \left[a - \frac{b}{2} \left(\frac{S}{W}\right) + \frac{c}{3} \left(\frac{S}{W}\right)^2 - \frac{d}{4} \left(\frac{S}{W}\right)^3 + \frac{e}{5} \left(\frac{S}{W}\right)^4 - \frac{f}{6} \left(\frac{S}{W}\right)^5 \right]$$

where $a = 1.068$, $b = 0.310$, $c = 0.079$, $d = 1.154 \times 10^{-2}$, $e = 8.133 \times 10^{-4}$ & $f = 2.141 \times 10^{-5}$

(5.5)

For $8 \leq Y/W \leq 10$ and $0 \leq S/W \leq 13.6$,

$$Nu_{ave} = 1.175 Re_w^{0.54} \left(\frac{Y}{W}\right)^{-0.401} \left[a - \frac{b}{2} \left(\frac{S}{W}\right) + \frac{c}{3} \left(\frac{S}{W}\right)^2 - \frac{d}{4} \left(\frac{S}{W}\right)^3 + \frac{e}{5} \left(\frac{S}{W}\right)^4 - \frac{f}{6} \left(\frac{S}{W}\right)^5 \right]$$

where $a = 1.016$, $b = 0.393$, $c = 0.1$, $d = 1.323 \times 10^{-2}$, $e = 8.503 \times 10^{-4}$ & $f = 2.089 \times 10^{-5}$

(5.6)

The above correlations are valid for $5,600 \leq Re \leq 13,200$ to be within 14%.

The average Nusselt numbers for a single slot jet impinging on a flat surface was correlated within $\pm 15\%$ by Martin (1977) as follows:

$$\text{Nu}_{\text{ave}} = \left(\frac{1.53}{\frac{X}{2W} + \frac{Y}{2W} + 1.39} \right) \text{Pr}^{0.42} \text{Re}^m \quad (5.7)$$

$$\text{where } m = 0.695 - \left(\frac{X}{2W} + \left(\frac{Y}{2W} \right)^{1.33} + 3.06 \right)^{-1}$$

$$\begin{aligned} \text{Range of validity:} \quad & 3,000 \leq \text{Re} \leq 90,000 \\ & 4 \leq X/W \leq 50 \\ & 4 \leq Y/W \leq 20 \end{aligned}$$

Results of these calculations on the average Nusselt numbers distribution along the semi-cylindrical convex surface and flat surface are presented in Figures 5.8a and 5.8b. These figures show that the average Nusselt numbers increases with increasing Reynolds number and decreases with increasing the lateral/circumferential distance, Y/W or S/W . The findings of Whitaker (1986) tends to support similar observation. It is also apparent that the decay rate of average circumferential Nusselt numbers along the cylindrical convex surface is much faster than that which occurs laterally along the flat surface. The decrease of the Nusselt number of the semi-cylindrical convex surface is attributed to the effect of stabilizing the entire flow and reducing the energy and momentum transport near the wall due to the occurrence of a centrifugal force along the surface as described by Schlichting (1979) and Mayle et al. (1979). Increasing the circumferential/lateral distance leads to lower the average Nusselt number due to a substantial number of low value local Nusselt numbers occurring into the calculation. It should also be noted that at low slot jet-to-impingement spacing Y/W (within potential core), low circumferential distance (i.e. $S/W < 6$) and low turbulent Reynolds

number, correlations for a flat plate can be used to predict Nu_{ave} to within 5%. This phenomenon is limited to this case. As S/W increases, the effect of curvature becomes apparent and the difference between the flat surface correlation and the present convex surface quickly increases. As Reynolds number Re_w increases, dramatic differences in the curves can be observed, for example at $Re_w = 13,200$ and $S/W = 10$ the present correlation leads to a 41% improvement as shown in Figure 5.8a. As Y/W increases, the effect difference becomes more pronounced as shown in Figure 5.8b.

In fact, the average Nusselt number value for impinging hot jets is about 10% higher than surface cooling at a given Reynolds number as described by Downs and James (1987). But, Hollworth and Gero (1984) and Goldstein et al. (1990) addressed the effect of thermal entrainment on impingement heat transfer depending on whether the surface is heated or cooled. They showed that, for the same Reynolds number, hot jets yield high Nusselt number however, if the adiabatic wall temperature is used to define heat transfer coefficient, data can be used to describe either arrangement.

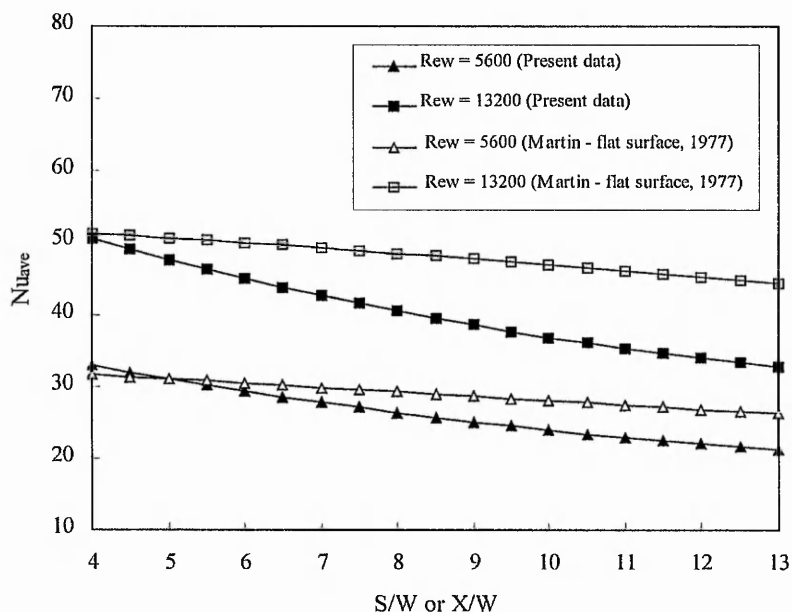


Figure 5.8a Comparison of average Nusselt number calculated using correlations for the semi-cylindrical convex surface and published correlations for the flat surface at $Y/W = 4$.

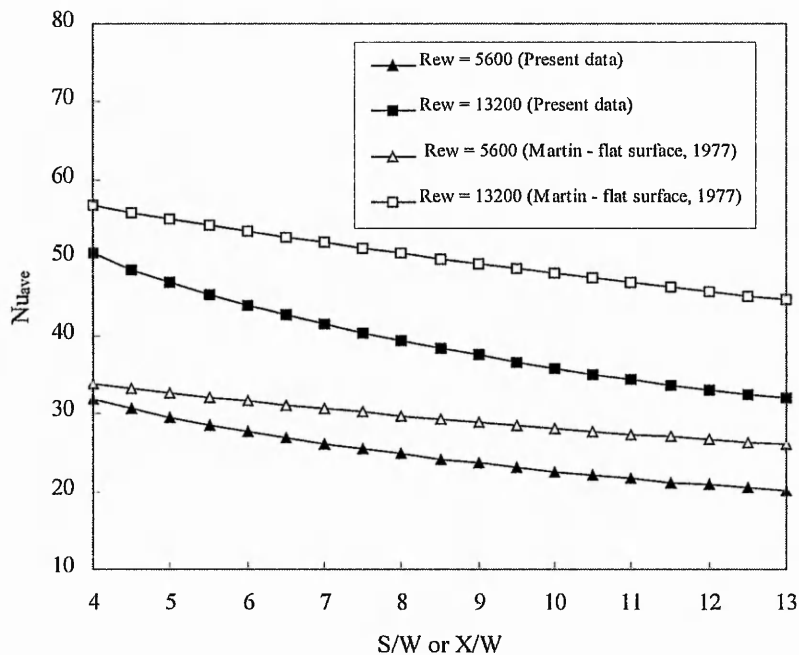


Figure 5.8b Comparison of average Nusselt number calculated using correlations for the semi-cylindrical convex surface and published correlations for the flat surface at $Y/W=8$.

5.4 Comparison between the Numerical and Experimental Heat Transfer Results

The standard $k-\epsilon$ turbulence model has been assessed due to its wide use in industry and availability in commercial CFD codes. The computed circumferential Nusselt number distribution is compared with the experimental results in Figures 5.9a to 5.9d. At the stagnation region however, Nu_0 is overpredicted up to 190%. The inflection point that represents the end of impingement region is predicted to be located at about $0.6 \leq S/W \leq 0.7$. In fact, the experimental results show that this region can be extended up to $3.1W$ from the centerline of a slot jet. In the wall jet ($S/W > 3$), the local Nusselt number is predicted to be within 29% of the experimental data. Ashforth-Frost (1994) has shown that the wall exerts an effect on the turbulence level distribution when the flow impinges on the target surface. This implies that the flow in the stagnation region is anisotropic (non-isotropic), with a return to isotropy further downstream along the wall. It should be noted that the turbulence models and wall functions have been

developed for fluid flows parallel to walls where isotropy predominates. In addition, the k - ε model is only valid for flows with sufficiently high Reynolds number ($Re > 132$) so that the flow characteristics near to the wall node may not be simulated accurately. For the grid cell between the wall and the near wall node, the k and ε values are obtained from a universal wall function accordingly.

It has been argued in Section 4.4 that if the local near wall Reynolds number is greater than 132 (or $y_p \sim Re^{0.5}$), then the wall function associated with the log-law can be used accurately to calculate shear stress, heat flux and other variables. Therefore the selection of near wall cell size (grid distribution) is vitally important in order to eliminate the uncertainties inherent to the cylinder boundary layer. In the present numerical model, this condition ($y_p > 11.5$) is only satisfied for S/W slightly greater than 0.49 and 0.64 with respect to the jet Reynolds number Re_w of 13,200 and 5,600, which also allows a more reliable prediction of Nu values along the circumferential surface. However, it is difficult to specify an appropriate value of local near wall Reynolds number or y_p over the whole computational domain especially in a developing wall flow region. The azimuthal velocity starts at zero at stagnation point and increases significantly along the wall, however this universal wall function is only valid for a fully developed boundary layer.

Since most of the discrepancies between the predictions and the measurements are seen in the stagnation region, it is plausible that using a more appropriate wall function should be able improved the predictions. In fact, the standard k - ε model does not predict appropriately in the stagnation region where the direction of flow changes suddenly and the variation of pressure changes substantially.

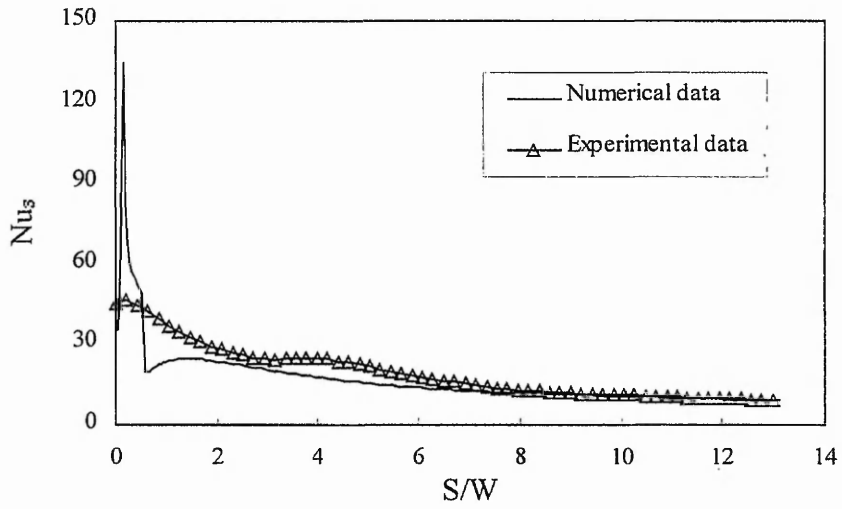


Figure 5.9a Circumferential Nusselt number distribution, $Re_w = 5,600$ & $Y/W = 4$.

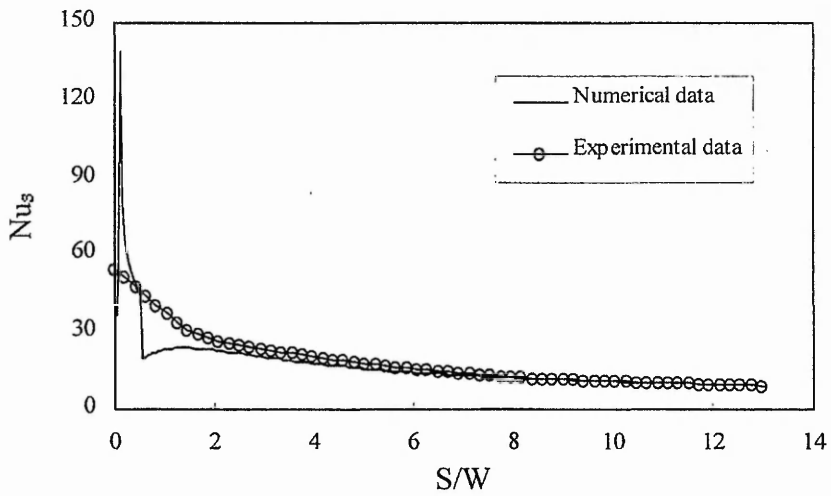


Figure 5.9b Circumferential Nusselt number distribution, $Re_w = 5,600$ & $Y/W = 8$.

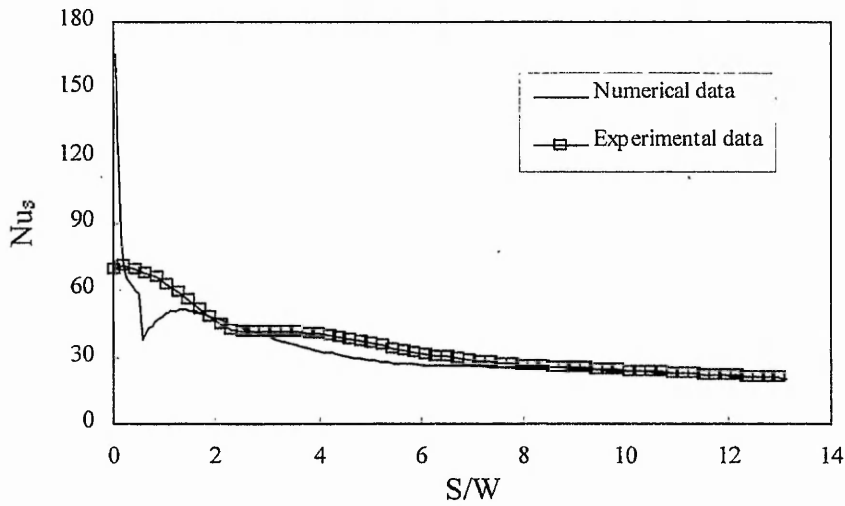


Figure 5.9c Circumferential Nusselt number distribution, $Re_w = 13,200$ & $Y/W = 4$.

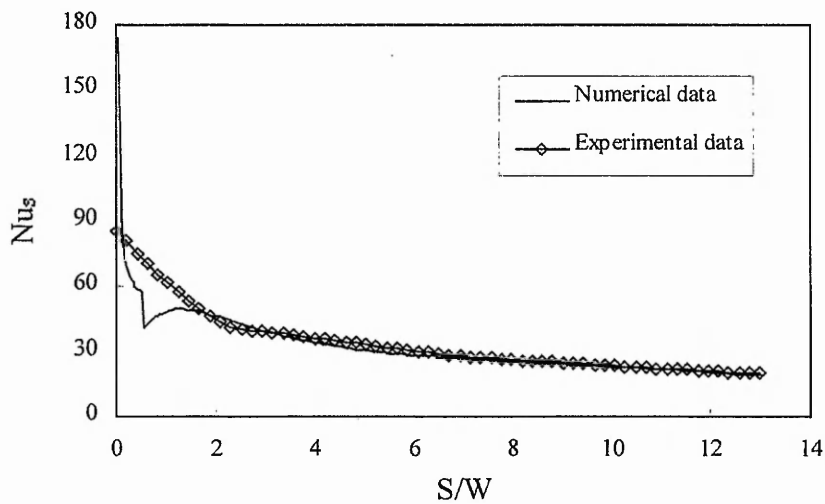


Figure 5.9d Circumferential Nusselt number distribution, $Re_w = 13,200$ & $Y/W = 8$.

5.5 Summary of Chapter

This chapter deals mainly with the parametric effects of jet Reynolds number (Re_w) and the slot jet-to-impingement surface spacing (Y/W) on the local and average circumferential Nusselt number distribution. Qualitative thermal visualization has been carried out to gain insight into thermal propagation due to a heated air slot jet on a semi-cylindrical convex surface. Quantitative measurements of flow characteristics at the slot nozzle exit and heat transfer characteristics have been made using the hot wire

anemometry and the developed liquid crystal thermographic system respectively. The experimental results have also been compared on the consistency and reliability with other relevant research works. The flow geometry has been modelled using computer simulation and results predicted using the $k-\varepsilon$ turbulence model.

The thermal visualisation demonstrated the thermal propagation due to a heated air slot jet impinging on a semi-cylindrical convex surface by a series of liquid crystal thermographic images at various Y/W and Re_w . The highest temperature (in dark blue/blue contour) was observed at the stagnation region directly beneath the impinging slot jet, and decreased gradually along the circumferential direction to the lowest temperature (in red contour).

The streamwise turbulence intensity at the slot nozzle exit was characterised over jet Reynolds number ranging from 5,600 to 13,200. The mean axial velocity profiles were found to be flat and uniform to within 3% over approximately the central 90% of the slot nozzle width, dropping very sharply to almost zero near the nozzle wall. The turbulence intensity profiles across the nozzle width were found to be at a value of around 1% turbulence intensity in the central region, and rising to about 2% at the nearest location to the nozzle wall.

The stagnation Nusselt number Nu_0 increases monotonically for a studied Reynolds numbers of 5,600 to 13,200 and continues to increase non-linearly to its peak values at $Y/W=8$. A similar non-linear Nu_0 behaviour for increasing Y/W has also been found from other authors' works. Correlations of Nu_0 in terms of Re_w and Y/W were derived.

The stagnation Nusselt number shows good agreement with $Nu_0 \propto Re_w^{0.5}$ laminar boundary-layer flow for $Y/W=2$ to 6 in this study. For the longer slot jet-to-impingement surface spacing of $Y/W > 6$, the Reynolds number dependence is stronger ($Nu_0 \propto Re_w^{0.54}$) and this attributed to these spacings being beyond the potential core region and air entrainment effects on the jet momentum takes place. The results agree with the Reynolds number correlation from other authors' works. The stagnation Nusselt number is less dependent on target surface geometry.

Circumferential Nusselt number distributions along the axis of the semi-cylindrical convex surface for different Re and Y/W parameters have been investigated. The circumferential local Nusselt numbers increase with increasing Reynolds numbers. However, the circumferential local Nusselt numbers decrease with increasing the circumferential distance S from its maximum value at stagnation point due to a presumed laminar boundary layer development up to $S/W = 3.1$ where transition in the boundary layer from laminar to turbulent flow occurs and it causes an increase in the local Nusselt numbers. This transition is completed at about $3.3 \leq S/W \leq 4.2$ where the second peak occurs in this region. However the maximum Nu occurs at $S/W \cong 0.21$ from the centerline of the jet for $Y/W \leq 4$. A similar slot jet behaviour was also shown to be found at $Y/W = 4$ by Whitney (1995). This occurrence is due to the slot nozzle exit which gives a flat velocity profile indicating that the centerline turbulence level has not reached a fully developed region. The turbulence level in the shear layer at the jet boundary is higher than on the jet centerline. This higher turbulence level causes a small increase in the Nusselt number just adjacent to the centerline of the jet.

For $Y/W = 2$ and 4 at low $Re_w = 5,600$, the transition starts to commence at around $2.9 \leq S/W \leq 3.2$ and reaches a secondary peak (turbulent heat transfer) at $S/W \cong 4.2$. For $Y/W = 2$ and 4 at high $Re_w = 13,200$, the transition starts to take place at around $2.5 \leq S/W \leq 2.7$ and attains the secondary peak at $S/W \cong 3.4$. It is shown that the transition occurs sooner and is completed in a shorter circumferential distance for higher jet Reynolds number. The findings of other authors tend to support this observation. Beyond the circumferential distance S of about 9 slot width, the local Nusselt numbers are almost independent of the impingement surface distance Y with respect to the studied Reynolds numbers Re_w . This behaviour can also indicate the existence of a fully developed wall jet at these locations. For $Y/W \geq 8$, it has been shown that the secondary peak almost disappeared due to the stagnation region turbulence effects. The circumferential Nusselt number distributions Nu_s were correlated in terms of Re_w , Y/W and S/W parameters.

The average Nusselt numbers were also correlated in terms of Re_w and Y/W over the circumferential distance S/W . The average Nusselt numbers increase with increasing

Reynolds number and decreases with increasing the lateral/circumferential distance, Y/W or S/W . It is also apparent that the decay rate of circumferential average Nusselt numbers along the cylindrical convex surface is much faster than that which occurs laterally along the flat surface. It should also be noted that at low slot jet-to-impingement spacing Y/W (within potential core), low circumferential distance (i.e. $S/W < 6$) and low turbulent Reynolds number, correlations for a flat plate can be used to predict Nu_{ave} to within 5%. This phenomenon is limited to this case. As S/W increases, the effect of curvature becomes apparent and the difference between the flat surface correlation and the present convex surface quickly increases. As Reynolds number Re_w increases, dramatic differences in the curves can be observed, for example at $Re_w = 13,200$ and $S/W = 10$ the present correlation leads to a 41% improvement. As Y/W increases, the effect difference becomes more pronounced.

The standard $k-\epsilon$ turbulence model has been assessed due to its wide use in industry and availability in commercial CFD codes. At the stagnation region Nu_0 is overpredicted up to 190%. The inflection point that represents the end of impingement region is predicted to be located at about $0.6 \leq S/W \leq 0.7$. In fact, the experimental results show that the stagnation region can be extended up to $3.1W$ from the centerline of slot jet. In the wall jet ($S/W > 3$), the local Nusselt number is predicted to be within 29% of the experimental data. It has been shown that the selection of a near wall cell size within the viscous sublayer along the cylinder boundary layer is very crucial to obtain the best predicted Nusselt number. The overprediction of the Nusselt number at the stagnation region is directly related to the overprediction of turbulent kinetic energy, but also the wall function prediction is invalid in this region. Ashforth-Frost (1994) has shown that the wall exerts an effect on the turbulence level distribution when the flow impinges on the target surface. This implies that the flow in the stagnation region is anisotropic, with a return to isotropy further downstream along the wall. It should be noted that the turbulence models and wall functions have been developed for fluid flows parallel to walls where isotropy predominates.

Recently, it has been identified that near wall correction is of crucial importance to calculations of near wall turbulent flows and the second momentum closures can provide significant improvement in the prediction of anisotropic flows.

Chapter 6 Conclusions and Recommendations

This final chapter commences with a summary of the conclusions of the major findings of the current study, with particular regard to the aims specified in Section 1.2. The conclusions are discussed in two sections based on the qualitative and quantitative experimental, and numerical results. Practical implications of these findings are presented and followed by the recommendations for further work.

6.1 Summary of Conclusions

A comprehensive review of relevant literature on the heat/mass transfer characteristics of a slot/circular jet on convex surface has been completed. An experimental air slot jet system has been successfully developed and commissioned to obtain the velocity and turbulence data at the slot nozzle exit using constant temperature hot wire anemometry. The same experimental rig was used to obtain surface heat transfer data using an automatic non-intrusive liquid crystal thermographic system based on colour image processing and transient wall heating techniques. A thermal visualization of the impinging slot jet on a semi-cylinder convex surface provided useful insight to the thermal field. Particular attention has been paid to the experimental planning and design of this facility in order to minimise experimental uncertainty and thus ensure the validity of the results.

The present study has provided new data for the influences of Reynolds number, Re_w and slot jet-to-impingement surface separation distance, Y/W on the local and average circumferential heat transfer characteristics from a turbulent impinging slot jet along a semi-cylindrical convex surface. Heat transfer results have been corroborated with previous research works and extended the existing heat transfer information for this configuration. Prior to the present work, no study of the surface heat transfer measurements for this configuration could be found in literature.

6.2 Qualitative and Quantitative Experimental Results

The thermal visualization experiments has demonstrated the thermal propagation phenomena due to a heated air slot jet impinging on a semi-cylindrical convex surface by a series of liquid crystal thermographic images at various Y/W and Re_w . The highest temperature (in dark blue/blue contour) was observed at the stagnation region directly beneath the impinging slot jet, and was seen to decrease gradually along the circumferential direction to the lowest temperature (in red contour).

Velocity and turbulence measurements of a slot jet were made to understand the slot nozzle exit characteristics over the studied jet Reynolds number range from 5,600 to 13,200 using constant temperature hot wire anemometry. The mean axial velocity profiles have been found to be flat and uniform to within 3% over approximately the central 90% of the slot nozzle width, dropping very sharply to almost zero near the nozzle wall. The turbulence intensity profiles across the nozzle width were found to be at a value of around 1% turbulence intensity in the central region, and rising to about 2% at the nearest location to the nozzle wall.

The stagnation point Nusselt number Nu_0 was shown to increase monotonically and non-linearly to its peak values at $Y/W = 8$. A similar non-linear Nu_0 behaviour for increasing Y/W was also found by Gardon and Akfirat (1966), Popiel et al. (1980), Gau and Chung (1991) and Lee et al. (1997). Correlations of Nu_0 in terms of Re_w and Y/W have been derived as follows:

For $2 \leq Y/W < 8$,

$$Nu_0 = 0.514 Re_w^{0.5} \left(\frac{Y}{W} \right)^{0.124} \quad \text{with a calculated standard deviation of } <1\%. \quad (6.1)$$

For $8 \leq Y/W \leq 10$,

$$Nu_0 = 1.175 Re_w^{0.54} \left(\frac{Y}{W} \right)^{-0.401} \quad \text{with a calculated standard deviation of } <1\%. \quad (6.2)$$

The above correlations are valid for $5,600 \leq Re_w \leq 13,200$. The stagnation Nusselt number shows good agreement with $Nu_0 \propto Re_w^{0.5}$ laminar boundary-layer flow for $Y/W = 2$ to 6 in this study which have been well documented by Schlichting (1979) and Martin (1977). For the longer slot nozzle-to-impingement surface spacing of $Y/W > 6$, the Reynolds number dependence is stronger ($Nu_0 \propto Re^{0.54}$) because these spacings are beyond the potential core region and air entrainment effect on the jet momentum takes place. The results agrees well with a Reynolds number exponent at stagnation point from Gau and Chung (1991) and Lee et al. (1997). It has also been shown that Nusselt number at the stagnation is less dependent of target surface geometry.

The circumferential local Nusselt numbers increase with increasing Reynolds numbers. However, the circumferential local Nusselt numbers decrease with increasing the circumferential distance S from its maximum value at stagnation point due to a presumed laminar boundary layer development up to $S/W = 3.1$ where transition in the boundary layer from laminar to turbulent flow occurs and it causes an increase in the local Nusselt numbers. This transition was completed at about $3.3 \leq S/W \leq 4.2$ where the second peak occurs in this region. But the maximum Nu occurs at $S/W \cong 0.21$ from the centerline of the jet for $Y/W \leq 4$. This observation is in line with a similar research findings by Whitney (1995). This occurrence is attributed to the fact that slot nozzle exit which gives a flat velocity profile, the centerline turbulence level has not reached a fully developed region and the turbulence level in the shear layer is higher than on the jet centerline. This higher turbulence level causes a small increase in the Nusselt number just adjacent to the centerline of the jet. Pamadi and Belov (1980) have shown that the mechanism leading to the occurrence of the inner peak is due to the strong influence of mixing-induced and non-uniform turbulence in the developing jet.

For $Y/W = 2$ and 4 at low $Re_w = 5,600$, the transition starts to take place at $2.9 \leq S/W \leq 3.2$ and attain secondary peak (turbulent heat transfer) at $S/W \cong 4.2$. For $Y/W = 2$ and 4 at high $Re_w = 13,200$, the transition commences at $2.5 \leq S/W \leq 2.7$ and reach the secondary peak at $S/W \cong 3.4$. It is shown that the transition occurs sooner and is completed in a shorter circumferential distance for higher Reynolds number. The findings of Cadek and Zerkle (1974) and Lee et al. (1997) tend to support this

observation. Beyond the circumferential distance S/W of about 9 slot width, the local Nusselt numbers are almost independent of the impingement surface distance Y with respect to the studied Reynolds numbers Re_w . This behaviour could also indicate the existence of a fully developed wall jet at these locations. For $Y/W \geq 8$, it has shown that the secondary peak almost disappears due to the turbulence effects in the stagnation region.

The circumferential Nusselt number distributions Nu_s were correlated in terms of Re_w , Y/W and S/W parameters as follows:

For $2 \leq Y/W < 8$ and $0 \leq S/W \leq 13.6$,

$$\frac{Nu_s}{Nu_0} = 1.068 - 0.310 \left(\frac{S}{W} \right) + 0.079 \left(\frac{S}{W} \right)^2 - 0.012 \left(\frac{S}{W} \right)^3 + 0.001 \left(\frac{S}{W} \right)^4 - 2.141 \times 10^{-5} \left(\frac{S}{W} \right)^5$$

with a calculated standard deviation of 13.6%. (6.3)

For $8 \leq Y/W \leq 10$ and $0 \leq S/W \leq 13.6$,

$$\frac{Nu_s}{Nu_0} = 1.016 - 0.393 \left(\frac{S}{W} \right) + 0.1 \left(\frac{S}{W} \right)^2 - 0.013 \left(\frac{S}{W} \right)^3 + 0.001 \left(\frac{S}{W} \right)^4 - 2.089 \times 10^{-5} \left(\frac{S}{W} \right)^5$$

with a calculated standard deviation of 10.4%. (6.4)

The above correlations are valid for $5,600 \leq Re \leq 13,200$ to be within 14%.

It was shown that the average Nusselt numbers increase with increasing Reynolds number and decreases with increasing the lateral/circumferential distance, Y/W or S/W . The findings of Whitaker (1986) tends to support similar observation. It is also apparent that the decay rate of average circumferential Nusselt numbers along the cylindrical convex surface is much faster than the average lateral Nusselt numbers along the flat surface. The decrease of the Nusselt number of the convex surface is attributed to the effect of stabilizing the entire flow and reducing the energy and momentum transport near the wall due to the occurrence of a centrifugal force along the surface as described by Schlichting (1979) and Mayle et al. (1979). Increasing the

circumferential/lateral distance leads to lower the average Nusselt number due to a substantial number of low value local Nusselt numbers occurring into the calculation. It should also be noted that at low slot jet-to-impingement spacing Y/W (within potential core), low circumferential distance (i.e. $S/W < 6$) and low turbulent Reynolds number, correlations for a flat plate can be used to predict Nu_{ave} to within 5%. This phenomenon is limited to this case. As S/W increases, the effect of curvature becomes apparent and the difference between the flat surface correlation and the present convex surface quickly increases. As Reynolds number Re_w increases, dramatic differences in the curves can be observed, for example at $Re_w = 13,200$ and $S/W = 10$ the present correlation leads to a 41% improvement. As Y/W increases, the effect difference becomes more pronounced.

In fact, Downs and James (1987) have described that the average Nusselt number value for impinging hot jets is about 10% higher than surface cooling at a given Reynolds number. But, Hollworth and Gero (1984) and Goldstein et al. (1990) addressed the effect of thermal entrainment on impingement heat transfer depending on whether the surface is heated or cooled. They showed that, for the same Reynolds number, hot jets yield high Nusselt number however, if the adiabatic wall temperature is used to define heat transfer coefficient, data can be used to describe either arrangement. The average Nusselt numbers were also correlated in terms of Re_w and Y/W over the circumferential distance S/W as follows:

For $2 \leq Y/W < 8$ and $0 \leq S/W \leq 13.6$,

$$Nu_{ave} = 0.514 Re_w^{0.5} \left(\frac{Y}{W} \right)^{0.124} \left[a - \frac{b}{2} \left(\frac{S}{W} \right) + \frac{c}{3} \left(\frac{S}{W} \right)^2 - \frac{d}{4} \left(\frac{S}{W} \right)^3 + \frac{e}{5} \left(\frac{S}{W} \right)^4 - \frac{f}{6} \left(\frac{S}{W} \right)^5 \right]$$

where $a = 1.068$, $b = 0.310$, $c = 0.079$, $d = 1.154 \times 10^{-2}$, $e = 8.133 \times 10^{-4}$ & $f = 2.141 \times 10^{-5}$

(6.5)

For $8 \leq Y/W \leq 10$ and $0 \leq S/W \leq 13.6$,

$$Nu_{ave} = 1.175 Re_w^{0.54} \left(\frac{Y}{W} \right)^{-0.401} \left[a - \frac{b}{2} \left(\frac{S}{W} \right) + \frac{c}{3} \left(\frac{S}{W} \right)^2 - \frac{d}{4} \left(\frac{S}{W} \right)^3 + \frac{e}{5} \left(\frac{S}{W} \right)^4 - \frac{f}{6} \left(\frac{S}{W} \right)^5 \right]$$

where $a = 1.016$, $b = 0.393$, $c = 0.1$, $d = 1.323 \times 10^{-2}$, $e = 8.503 \times 10^{-4}$ & $f = 2.089 \times 10^{-5}$

(6.6)

The above correlations are valid for $5,600 \leq Re \leq 13,200$ to be within 14%.

6.3 Numerical Results

Using various CFD codes the k - ϵ model, and other turbulence models, have been examined by Craft et al. (1993), Seyedein et al. (1994), Sarkar and So (1997), and Lai and Yang (1997). By comparison with these works, the commercial code PHOENICS has been demonstrated in this study to predict jet impingement heat transfer to the same level of accuracy and reliability as other available software codes using the standard k - ϵ turbulence model. In the stagnation region however, Nu_0 is overpredicted up to 190%. The inflection point that represents the end of impingement region is predicted to be located at about $0.6 \leq S/W \leq 0.7$. In fact, the experimental results show that the stagnation region can be extended up to $3.1W$ from the centerline of slot jet. In the wall jet ($S/W > 3$), the local Nusselt number is predicted to within 29% of the experimental data where the turbulent kinetic energy is reasonably predicted by the k - ϵ eddy viscosity model and the universal wall function is valid. It has been shown that the selection of a near wall cell size within the viscous sublayer along the cylindrical boundary layer is crucial in obtaining the best predicted Nusselt number. The overprediction of the Nusselt number at the stagnation region is not only directly related to the overprediction of turbulent kinetic energy, but also attributed to the inaccuracies in the universal wall function used for predicting the momentum and heat transfer processes near the wall in this region.

Recently, it has been identified that near wall correction is of crucial importance to calculations of near wall turbulent flows and the second momentum closures can provide significant improvement in the prediction of anisotropic flows.

6.4 Practical Applications of the Results

New correlations of local and average Nusselt numbers with the jet Reynolds number Re_w and the slot jet-to-impingement spacing Y/W have been established for the stagnation point and the circumferential distribution S/W along the semi-cylindrical convex surface. At larger Y/W , S/W and Re_w , flat plate correlations become invalid, and these new correlations should be used for optimum design. Detailed explanation can be found to Section 5.3.4. These provide previously unavailable guidelines for industrialists exploiting jet impingement for optimum heating/cooling applications.

The new experimental data obtained in the present study is valuable for the assessment of turbulence models on surface heat transfer. It is important for users of CFD codes to be aware of the capabilities and limitations of the codes they are using for design purposes. This data is supported by two dimensional jet and flat exit velocity profiles which provide known boundary conditions.

6.5 Recommendations for Further Work

A more detailed study of the stagnation region is necessary to assess the role of turbulence flow structure on heat transfer, the interaction between the thermal and hydrodynamic boundary layers as well as the wall jet region along the cylindrical convex surface. This can be achieved in the first instance using a combined hot and cold wire anemometry traversed through the flow structure.

The flow visualization study will provide insight into the flow structure of a slot turbulent jet impinging on the convex surface at various slot jet-to-impingement surface, slot width and surface curvature in regard to the rotating vortices on the stagnation and the vortex formation in the downstream region.

It is generally agreed that high turbulence production is associated with not only increased fan power requirement, but also enhanced surface heat transfer rate. Their relationship and optimisation can be further studied with the aid of hot and cold wire anemometry system and the developed liquid crystal thermographic system.

The developed non-intrusive liquid crystal thermographic system based on colour image processing and transient wall heating techniques can be used to determine the transient heat transfer information with a high speed frame colour video camera.

The experimental data obtained in the present study is useful as an ideal test case for assessment of any numerical or turbulence model on surface heat transfer. Although beyond the scope of the present study, there is no question that the 3-D time-dependent Navier Stokes equations (or Direct Numerical Simulation (DNS)) is the ultimate solution to deal with the turbulence problems with the revolution of computing capabilities and less computing cost in the near future. However, the $k-\epsilon$ turbulence model is still widely used in industry because of it is economy over more complex solutions. The limitation of this model should be borne in mind when interpreting results from commercial packages.

References

- Abe, K., Kondoh, T. and Nagano, Y., 1994. A New Turbulence Model for Predicting Fluid Flow and Heat Transfer in Separating and Reattaching Flows. *Int. J. Heat Mass Transfer*, **37**(1), pp. 139-151.
- Abramovich, G.N., 1963. *The Theory of Turbulent Jets*. MIT Press.
- Akino, N., Kunugi, T., Ichimiya, K., Mitsushiro, K. and Ueda, M., 1989a. Improved Liquid-Crystal Thermometry Excluding Human Color Sensation. *ASME J. of Heat Transfer*, **111**, pp.558-565.
- Akino, N., Kunugi, T., Ueda, M. and Kurosawa, A., 1989b. A Study on Thermo-Camera Using a Liquid-Crystal (Method of Multiple Regression Between Colour and Temperature). *ASME National Heat Transfer Conf.- Heat Transfer Measurements, Analysis, and Flow Visualization*, HTD-**112**, pp.115-122.
- Akino, N., Kunugi, T., Ichimiya, K., Mitsushiro, K. and Ueda, M., 1989. Improved Liquid-Crystal Thermometry Excluding Human Color Sensation. *J. of Heat Transfer*, **111**, pp.558-565.
- Alhomoud, A.A., 1984. Heat Transfer from a Circular Cylinder Due to a Slot Jet Impingement. *PhD thesis*, University of Minnesota, USA.
- Arganbright, D.G. and Resch, H., 1971. A Review of Basic Aspects of Heat Transfer Under Impinging Air Jets. *Wood Science and Technology*, **5**, pp.73-94.
- Ashforth-Frost, S., Wang, L. S. and Jambunathan, K., 1992. Application of Image Processing to Liquid Crystal Thermography. *Optical Methods and Data Processing in Heat and Fluid Flow*, IMechE, April 2-3, , London, pp.121-126.
- Ashforth-Frost, S., 1994. The Use of Liquid Crystals in Temperature Visualisation. Proc. Biomechanics '94, Technical University of Wroclaw, October 202-3, Poland, pp. 342-351.
- Ashfrost-Frost, S., Jambunathan, K. and Whitney, C. F., 1997. Velocity and Turbulence Characteristics of a Semiconfined Orthogonally Impinging Slot Jet. *Experimental Thermal and Fluid Science*, **14**, pp. 60-67.
- Babinsky, H. and Edwards, J. A., 1996. Automatic Liquid Crystal Thermography for Transient Heat Transfer Measurements in Hypersonic Flow. *Experiments in Fluids*, **21**, pp.227-236.
- Baughn, J. W. and Shimizu, S., 1989a. Heat Transfer Measurements from a Surface with Uniform Heat Flux and an Impingement Jet. *J. of Heat Transfer*, **111**, pp. 1096-1099.

- Baughn, J. W., Ireland, P. T., Jones, T. V. and Saniei, N., 1989b. A Comparison of the Transient and Heated-Coating Methods for the Measurement of Local Heat Transfer Coefficients on a Pin Fin. *J. of Heat Transfer*. **111**, pp. 877-881.
- Baughn, J. W., 1995. Review- Liquid Crystal Methods for Studying Turbulent Heat Transfer. *Int. J. Heat and Fluid Flow*, **16**, pp.365-375.
- Becko, Y., 1976. Impingement Cooling - A Review. *Von Karman Institute for Fluid Dynamics, Lecture Series 83*, 12-16 January, 44pp.
- Bonnett, P., 1989. Application of Liquid Crystals in Aerodynamic Testing. *PhD Thesis*. University of Oxford, UK.
- Bradshaw, P., 1997. Understanding and Prediction of Turbulent Flow- 1996. *Int. J. Heat and Fluid Flow*, **18**, pp. 45-54.
- Braun, M.J., Dzodzo, M. and Lattime, S.B., 1993. Automatic Computer Based Non-Intrusive Temperature Measurements in Laminar Natural Convection Using TLC in Enclosures with Variable Aspect Ratio", *ASME Paper No. FED-172*, pp.111-119.
- Button, B.L. and Wilcock, D., 1978. Impingement Heat Transfer: A Bibliography 1890-1975. *Previews of Heat and Mass Transfer*, **4**(3), pp.83-98.
- Button, B.L. and Jambunathan, K., 1989. Jet-Impingement Heat Transfer: A Bibliography 1976-1985. *Previews of Heat and Mass Transfer*, **15**(2), pp.149-179.
- Cadek, F. F., 1968. A Fundamental Investigation of Jet Impingement Heat Transfer. *PhD Thesis*, University of Cincinnati, USA.
- Cadek, F. F. and Zerkle, R. D., 1974. Local Heat Transfer Characteristics of Two-dimensional Impinging Air Jets Theory and Experiment. *Heat Transfer*, **11**, Paper FC1.4, pp. 15-19.
- Camci, G., Kim, K. and Hippensteele, S. A., 1991. A New Hue Capturing Technique for the Quantitative Interpretation of Liquid Crystal Images Used in Convective Heat Transfer Studies. *ASME Paper 91-GT-122*, pp.1-13.
- Camci, C., Kim, K., Hippensteele, S.A. and Poinsette, P. E., 1993. Evaluation of a Hue Capturing Based Transient Liquid Crystal Method for High-Resolution Mapping of Convective Heat Transfer on Curved Surfaces. *J. of Heat Transfer*, **115**, pp.311-318.
- Celik, I. and Shaffer, F. D., 1991. Analysis of Numerical Simulations of Mean Turbulent Flow Past a Circular Cylinder. *Forum on Turbulent Flows*, June 23-27, Oregon, USA. FED-**112**, pp. 153-158.

- Chan, T. L., Jambunathan, K., Leung, T. P. and Ashforth-Frost S., 1994. A Surface Temperature Calibration Method for Thermochromic Liquid Crystals using True-colour Image Processing. *Proc. of the 10th Int. Heat Transfer Conf.*, Brighton, UK, **2**, pp. 201-206.
- Chan, T. L., Leung, T. P., Jambunathan, K. and Ashforth-Frost, S., 1995. Calibration of Thermochromic Liquid Crystals applied to an Oblique Surface. IMechE Conference Transactions, *4th UK National Conference on Heat Transfer*, Sept. 26-27, pp. 61-66.
- Chan, T. L., 1997. Liquid Crystal Thermography of Heat Transfer Distribution on a Flat Plate in a Turbulent Impinging Circular Jet. *Proc. of the 2nd Int. Sym. on Heat Transfer Enhancement and Energy Conservation*, pp. 409-414.
- Clifford, R. J., Jones, T. V. and Dunne, S. T., 1983. Techniques for Obtaining Detailed Heat Transfer Coefficient Measurements Within Gas Turbine Blade and Vane Cooling Passages. *ASME Paper No. 83-GT-58*, 6pp.
- Cooper, T. E., Meyer, J. F., and Field, R. J., 1975. Liquid Crystal Thermography and Its Application to the Study of Convective Heat Transfer. *ASME Paper No. 75-HT-15*, 12pp.
- Crabtree, J. A., 1994. Use of Image Processing Techniques for Heat Transfer Measurements Using Thermochromic Liquid Crystals. *ASME Paper No. HTD-279*, pp.27-33.
- Craft, T. J., Graham, L. J. W. and Launder, B. E., 1993. Impinging Jet Studies for Turbulence Model Assessment- II. An Examination of the Performance of Four Turbulence Models. *Int. J. Heat Mass Transfer*, **36**(10), pp. 2685-97.
- Craft, T. J., Launder, B. E., and Suga, K., 1997. Transitional Phenomena with a Nonlinear Eddy-Viscosity Model. *Int. J. Heat and Fluid Flow*, **18**, pp. 15-28.
- Cziesla, T., Tandogan, E., and Mitra, N. K., 1997. Large-eddy Simulation of Heat Transfer from Impinging Slot Jets. *Numerical Heat Transfer, Part A*, **32**, pp. 1-17.
- Den Ouden, C. and Hoogendoorn, C. J., 1974. Local Convective-Heat-Transfer Coefficients for Jets Impinging on a Plate; Experiments Using a Liquid-Crystal Technique. *Proc. 5th Int. Heat Transfer Conf.*, AIChE, **5**, New York, pp.293-297.
- Davenport, C. J., 1989. A Technique for Measuring Local Heat Transfer Due to an Impinging Liquid Spray. *ASME National Heat Transfer Conf.- Heat Transfer Phenomena in Radiation, Combustion and Fires*, HTD-**106**, pp. 531-536.
- Dianat, M., Fairweather, M., and Jones, W. P., 1996. Predictions of Axisymmetric and Two-dimensional Impinging Turbulent Jets. *Int. J. Heat and Fluid Flow*, **17**, pp. 530-538.

- Downs, S. J. and James, E. H., 1987. Jet Impingement Heat Transfer - A Literature Survey. *ASME Paper No. 87-HT-35*, 10pp.
- Ellis, L. B. and Joubert, P. N., 1974. Turbulent Shear Flow in a Curved Duct. *J. Fluid Mech.*, pp. 65-84.
- Faghri, M., 1984. Slot Jet Impingement on a Cylinder. *ASME paper, 84-HT-71*, pp.1-4.
- Farina, D. J., Hacker, J. M., Moffat, R. J. and Eaton, J. K., 1994. Illuminant Invariant Calibration of Thermochromic Liquid Crystals. *Experimental Thermal and Fluid Science*, **9**, pp. 1-12.
- Fujisawa, N. and Kobayashi, R., 1987. Turbulence Characteristics of Wall Jets along Strong Convex Surfaces. *Int. J. Mech. Sci.*, **29**(5), pp. 311-320.
- Gardon, R. and Akfirat, J. C., 1966. Heat Transfer Characteristics of Impinging Two-dimensional Air Jets. *J. Heat Transfer*, Feb., pp. 101-108.
- Gau, C. and Chung, C. M., 1991. Surface Curvature Effect on Slot-Air-Jet Impingement Cooling Flow and Heat Transfer Process. *J. of Heat Transfer*, **113**, pp.858-864.
- Gauntner, J. W., Livingood, J. N B. and Hrycak, P., 1970. Survey of Literature on Flow Characteristics of a Single Turbulent Jet Impinging on a Flat Plate. *NASA TN D-5652*, pp.1-43.
- Giedt, W. H., 1951. Effect of Turbulence Level of Incident Air Stream on Local Heat Transfer and Skin Friction on a Cylinder. *J. of Aeronautical Science*, **18**, pp. 725-730.
- Gillespie, D. R. H., Guo, S. M., Wang, Z., and Ireland, P. T., 1996. A Comparison of Full Surface Local Heat Transfer Coefficient and Flow Field Studies Beneath Sharp-edged and Radiused Entry Impinging Jets. *ASME Paper No. 96-GT-428*, pp. 1-9.
- Goldstein, R. J., Sobolik, K. A. and Seol, W. S., 1990. Effect of Entrainment on the Heat Transfer to a Heated Circular Air Jet Impinging on a Flat Surface. *J. of Heat Transfer*, **112**, pp. 608-11.
- Gomiciaga, R., Lee, K. C. and Yianneskis, M., 1991. Development of a Liquid Crystal Thermographic Technique Using Video Image Processing. *Development in Heat Transfer*, IChem, June 20, Nottingham University, pp.1-13.
- Gostkowski, V. J. and Costello, F. A., 1970. The Effect of Free Stream Turbulence on the Heat Transfer from the Stagnation Point of a Sphere. *Int. J. Heat Mass Transfer*. **13**, pp. 1382-1386.
- Hay, J. L. and Hollingsworth, D. K., 1996. A Comparison of Trichromic Systems for Use in the Calibration of Polymer-Dispersed Thermochromic Liquid Crystals. *Experimental Thermal and Fluid Science*. **12**, pp.1-12.

- Herold, W. and Wiegel, D., 1980. Problems of the Photographic Documentation of Liquid Crystalline Thermographs. *Advances in Liquid Crystal Research and Applications*. (Ed. by Bata L.) Pergamon Press, Oxford, pp.1255-1259.
- Hippensteele, S. A., Russell, L. M. and Stepka, F. S., 1983. Evaluation of a Method for Heat Transfer Measurements and Thermal Visualization Using a Composite of a Heater Element and Liquid Crystals. *J. of Heat Transfer*. **105**, pp.184-189.
- Hollingsworth, D. K., Boehman, A. L., Smith, E.G. and Moffat, R. J., 1989. Measurement of Temperature and Heat Transfer Coefficient Distributions in a Complex Flow Using Liquid Crystal Thermography and True-Color Image Processing", ASME Winter Meeting, San Francisco, California, 10-15 Dec., *ASME Paper No. HTD-123*, pp.35-42.
- Hollworth, B. R. and Gero, S. I., 1984. Entrainment Effects on Impingement Heat Transfer: Part II- Local Heat Transfer Measurements. *J. of Heat Transfer*, **107**, pp. 910-915.
- Hrycak, P., 1981. Heat Transfer From Impinging Jets - A Literature Review, *AFWAL-TR-81-3054*, 63pp.
- Livingood, J. N. B. and Hrycak, P. 1973. Impingement Heat Transfer from Turbulent Air Jets to Flat Plates - A Literature Survey. *NASA TM X-2778*, 43pp.
- Ichimiya, K. and Hosaka, N., 1989. Experimental Study of Heat Transfer Characteristics due to Confined Impinging Two-dimensional Jets. *Trans. JSME*, Part B, **55**(518), pp. 3210-3215.
- Ireland, P. T. and Jones, T. V., 1985. The Measurement of Local Heat Transfer Coefficients in Blade Cooling Geometries. *AGARD Conference Proc. No. 390*, Paper 28.
- Ireland, P. T. and Jones, T. V., 1986. Detailed Measurements of Heat Transfer On and Around A Pedestal in Fully Developed Passage Flow", *Proc. of the 8th Int. Heat Transfer Conference, California, USA*, **3**, pp.975-980.
- Ireland, P., 1987. Internal Cooling of Turbine Blades. *PhD Thesis*, University of Oxford, UK, pp.1-173.
- Ireland, P. T. and Jones, T. V., 1987. The Response Time of A Surface Thermometer Employing Encapsulated Thermochromic Liquid Crystals. *J. Phys. E: Sci. Instrum.* **20**, pp. 1195-1199.
- Jambunathan, K., Lai, E., Moss, M. A. and Button, B. L., 1992. A Review of Heat Transfer Data for Single Circular Jet Impingement. *Int. J. Heat and Fluid Flow*, **13**(2), pp.106-115.

- Jambunathan, K. and Button, B. L., 1994. Jet Impingement Heat Transfer: A Bibliography 1986-1991, *Previews of Heat and Mass Transfer*, **20**(5), pp. 385-413.
- Jayatilleke, C. L., 1969. The Influence of Prandtl Number and Surface Roughness on the Resistance of the laminar Sub-layer to Momentum and Heat Transfer. *Progress in Heat and Mass Transfer*, **1**, pp. 193-329.
- Jones, W. P. and Launder, B. E., 1972. The Prediction of Laminarization with a Two-equation Model of Turbulence. *Int. J. Heat mass Transfer*, **15**, pp. 301-374.
- Jones, T. V., Wang, Z. and Ireland, P. T., 1992. The Use of Liquid Crystals in Aerodynamic and Heat Transfer Experiments. *Optical Methods and Data Processing in Heat and Fluid Flow*, April 2-3, London, pp.51-65.
- Kang, S. H. and Greif, R., 1992. Flow and Heat Transfer to a Circular Cylinder with a Hot Impinging Air Jet. *Int. J. Heat Mass Transfer*, **35**(9), pp.2173-2183.
- Kataoka, K., Hamano, S., Onishi, A., Kawasaki, H. and Li, G. Y., 1992. Control of Jet Impingement Heat Transfer by a Wake Flow Behind an Array of Circular Cylinders. *J. of Chemical Engineering of Japan*, **25**(1), pp.39-43.
- Kline, S. J. and McClintock, F. A., 1953. Describing Uncertainties in Single-Sample Experiments. *Mechanical Engineering*, **75**, pp. 3-8.
- Knowles, K., 1996. Computational Studies of Impinging Jets using k- ϵ Turbulence Models. *Int. J. for Numerical Methods in Fluids*, **22**, pp. 799-810.
- Kreith, F., 1955. The Influence of Curvature on Heat Transfer to Incompressible Fluids", *Trans. ASME*, **77**, pp. 1247-1256.
- Krzywoblocki, M. Z. V., 1956. Jets - Review of Literature. *Jet Propulsion*, September, pp.760-779.
- Kumada, M., Mabuchi, I. and Kawashima, Y., 1973. Mass Transfer on a Cylinder in the Potential Core Region of a Two-Dimensional Jet", *Heat Transfer - Japan Res.*, **2**(3), pp.53-66.
- Kumada, M., Mabuchi, I., Kawashima, Y. and Hirata, M., 1974. Mass Transfer on a Cylinder in Developed Region of a Two-Dimensional Jet. *Trans JSME*, **30**(330), pp. 471-478.
- Lai, J. C. S. and Yang, C. Y, 1997. Numerical Simulation of Turbulence Suppression: Comparisons of the Performance of Four k- ϵ turbulence Models. *Int. J. Heat and Fluid Flow*, **18**, pp. 574-584.
- Launder, B. E. and Spalding, D. B, 1974. The Numerical Computation of Turbulent Flows. *Computer Methods in Applied Mechanics and Engineering*, **3**, pp.269-289.

- Launder, B. E., 1991. Turbulence Modelling for Impinging Flows. EASE Education and Awareness Programme, ERCOFTAC UK North Pilot Centre and SERC CFD Community Club, , *Proc. from the Workshop*, 30 October, UMIST, UK .
- Lee, D. H., Chung, Y. S. and Kim, D. S., 1997. Turbulent Flow and Heat Transfer Measurements on a Curved Surface with a Fully Developed Round Impinging Jet. *Int. J. Heat and Fluid Flow*, **18**, pp. 160-169.
- Livingood, J. N. B. and Hrycak, P., 1973. Impingement Heat Transfer from Turbulent Air Jets to Flat Plates - A Literature Survey. *NASA TM X-2778*, pp.1-43.
- Lowery, G. W. and Vachon, R. I., 1975. The Effect of Turbulence on Heat Transfer from Heated Cylinders. *Int. J. Heat Mass Transfer*, **18**, pp.1229-1242.
- Malin, M. R., Prediction of Radially Spreading Turbulent Jets. *AIAA J.*, **26**, pp. 750-752.
- Maple, R. D., 1972. Utilization of Temperature Sensitive Liquid Crystals for Thermal Analysis and an Application to Transducer Investigations. *NUSC-TR-4235*, May 30, pp.1-50
- Martin, H., 1977. Heat and Mass Transfer between Impinging Gas Jets and Solid Surfaces. *Advances in Heat Transfer*. **13**, 60pp.
- Mayle, R. E., Blair, M. F. and Kopper, F. C., 1979. Turbulent Boundary Layer Heat Transfer on Curved Surfaces. *J. of Heat Transfer*, pp. 521-525.
- McCamy, C. S., Marcus, H. and Davidson, J. G., 1976. A Color Rendition Chart. *J. of Applied Photographic Engineering*, **11**(3), pp. 95-99.
- Mehta, R. D., 1977. The Aerodynamic Design of Blower Tunnels with Wide Angle Diffusers. *Prog. Aerospace Sci.*, **18**, pp. 59-120.
- Metzger, D. E. and Larson, E. E., 1986. Use of Melting Point Surface Coatings for Local Convective Heat Transfer Measurements in Rectangular Channel Flows with 90-deg. Turns. *J. of Heat Transfer*, **108**, pp. 48-54.
- Mizell, L., 1970. Liquid Crystals: A New Technique for Thermal Mapping of Electronic Components. *Microelectronics 4: 4th International Congr.*, Nov. 9-11, Munich, pp.450-475.
- Miyazaki, H., 1975. Flow and Heat-Transfer Characteristics for a Two-Dimensional Jet Impinging on a Circular Cylinder. *PhD thesis*, University of Minnesota, USA.
- Miyazaki, H. and Sparrow, E. M., 1976. Potential Flow Solution for Crossflow Impingement of a Slot Jet on a Circular Cylinder. *ASME Paper No. 76-FE-F*, pp.1-7.

- Moffat, R. J., 1985. Using Uncertainty Analysis in the Planning of an Experiment. *ASME J. Fluids Eng.*, **107**, pp 173-178.
- Moffat, R. J., 1990. Experimental Methods for Heat Transfer Studies. *Experimental Thermal and Fluid Science*. **3**, pp. 14-32.
- Mujumdar, A. S. and Douglas, W. J. M., 1972. Impingement Heat Transfer: A Literature Survey. *The Technical Association of Pulp and Paper Industries Meeting*, October, New Orleans, LA, USA, pp.107-136.
- Obot, N. T., Mujumdar, A. S. and Douglas, W. J. M., 1979. Effect of Nozzle Geometry on Impingement Heat Transfer under a Round Turbulent Jet. *ASME Paper No. 79-WA/HT-53*. pp. 1-12.
- O'Brien, J. E., Simoneau, R. J., LaGraff, J. E. and Morehouse, K. A., 1986. Unsteady Heat Transfer and Direct Comparison for Steady-state Measurements in Rotor-wake Experiment. *8th Int. Heat Transfer Conf.*, San Francisco, pp. 1243-1248.
- Ojha, S. K. and Gollakota, S., 1977. Jet Impingement on a Curved Surface. *AIAA J.*, **15**(4), pp.453-454.
- Pamadi, P. N. and Belov, I. A., 1980. A Note of the Heat Transfer Characteristics of Circular Impinging Jet. *Int. J. Heat Mass Transfer*, **23**, pp.783-787.
- Parker, R., 1973. Transient Surface Temperature Response of Liquid Crystal Films. *Molecular Crystals and Liquid Crystals*. **20**, pp.99-106.
- Parsley M., 1991. The HALLCREST Handbook of Thermochromic Liquid Crystal Technology. pp.1-34.
- Pantankar, S. V. and Spalding, D. B., 1972. A Calculation Procedure for Heat, Mass and Momentum Transfer in Three Dimensional Parabolic Flows. *Int. J. Heat Mass Transfer*, **15**, pp. 1787-1805.
- Polat, S., Mujumdar, A. S. and Douglas W. J. M., 1985. Heat Transfer Distribution under a Turbulent Impinging Jet- A Numerical Study. *Drying Technology*, **3**(1), pp. 15-38.
- Polat, S., Huang, B., Mujumdar, A. S. and Douglas, W. J. M., 1989. Numerical Flow and Heat Transfer under Impinging Jets: A Review. *Annual Review of Numerical Fluid Mechanics and Heat Transfer* (Ed. by Tien, C. L. and Chawla T. C.), **2**, pp.157-197.
- Popiel, Cz. O., van der Meer Th. H., and Hoogendoorn, C. J., 1980. Convective Heat Transfer on a Plate in and Impinging Round Hot Gas Jet of Low Reynolds Number. *Int. J. Heat Mass Transfer*, **23**, pp. 1055-1068.
- Potts, Dennis W., 1984. An Experimental Study of Jet Impingement on a Circular Cylinder. *Report No. AFIT/CI/NR 84-50T*, 192pp.

- Rojas, J. and Whitelaw, J. H., 1987. Forced Convective Heat Transfer in Curved Diffusers. *Trans. ASME*, **109**, pp.866-869
- Rodi, W., 1993. Turbulence Models and Their Application in Hydraulics - A State of the Art Review. *IAHR*, Balkema A. A. Publishers, 98pp.
- Rosten, H. I. and Worrell, J. K., 1988. Generalised Wall Functions for Turbulent Flow. *PHOENICS Journal of CFD and its Applications*, 1(1), pp. 81-109.
- Saad, N. R., 1981. Flow and Heat Transfer for Multiple Turbulent Impinging Slot Jets. *PhD Thesis*, McGill University, Canada.
- Saabas, H. J., Arora, S.C. and Messeh, W. A., 1987. Application of the Transient Test Technique to Measure Local Heat Transfer Coefficients Associated with Augmented Airfoil Cooling Passages. *ASME Paper No. 87-GT-212*.
- Sarkar, A. and So, R. M. C., 1997. A Critical Evaluation of Near-wall Two-equation Models against Direct Numerical Simulation Data. *Int. J. Heat and Fluid Flow*, 18, pp. 197-208.
- Sawyer, R. A., 1962. Two-dimensional Turbulent Jets with Adjacent Boundaries. *PhD Thesis*, University of Cambridge, UK.
- Sawyer, R. A., 1963. Two-dimensional Reattaching Jet Flows including the Effects of Curvature on Entrainment. *J. Fluid Mech.*, **17**(4), pp. 481-499.
- Scholtz, M. T. and Trass O., 1970. Mass Transfer in a Non-uniform Impinging Jet, *AIChE J.*, **16**(1), pp. 82-96.
- Schultz, D. L. and Jones, T. V., 1973. Heat Transfer measurements in Short-Duration Hypersonic Facilities, AGARD 165.
- Schuh, H. and Persson, B., 1964. Heat Transfer on Circular Cylinders Exposed to Free-Jet Flow. *Int. J. Heat Mass Transfer*, **7**, pp.1257-1271.
- Seban, R.A., 1960. The Influence of Free Stream Turbulence on the Local Heat Transfer from Cylinders. *J. of Heat Transfer*, May, pp.101-107.
- Seyedein, S. H., Hasan, M. and Mujumdar, A. S., 1994. Modelling of a Single Confined Turbulent Slot Jet Impingement using various k- ϵ Turbulence Models. *Appl. Math. Modelling*, **18**, pp. 526-537.
- Shiravi, A. H., Mujaumadar, A. S. and Kubes, G. J., 1995. Numerical Study of Heat Transfer and Fluid Flow in Multiple Turbulent Impinging Jets. *Drying Technology*, **13**(5-7), pp. 1359-1375.

- Shyy, W., Pang, Y., Chen, M.H. and Wei, D.Y., 1991. Heat Transfer and Convection Characteristics of Superheated Turbulent Jet Interacting with Solid Object. *Winter Ann. Meeting of ASME- Fundamentals of Forced and Mixed Convection and Transport Phenomena*, Georgia, USA. Dec 1-6, HTD-180, pp.29-39.
- Simon, T. W. and Moffat, R. J., 1982. Convex Curvature Effects on the Heated Turbulent Boundary Layer", *Proc. of the Seventh Int. Heat Transfer Conf.*, Muchen, Fed. Rep. of Germany, 3, pp.295-300.
- Smith, A. J. D. and Baxter, D. R. J., 1989. Liquid Crystal Thermography for Aerodynamic Heating Measurements in Short Duration Hypersonic Facilities, ICIASF '89, Sept. 18-21, pp.104-112.
- So, R. M. C. and Mellor, G. L., 1972. An Experimental Investigation of Turbulent Boundary Layers along Curved Surfaces. *NASA CR-1940*, 260pp.
- So, R. M. C. and Mellor, G. L., 1973. Experiment on Convex Effects in Turbulent Boundary Layers. *J. Fluid Mech.*, 60(1), pp. 43-62.
- Sparrow, E. M., Altemani, C. A. C. and Chaboki, A., 1984a. Jet-Impingement Heat Transfer for a Circular Jet Impinging in Crossflow on a Cylinder. *J. of Heat Transfer*, 106, pp.570-577.
- Sparrow, E. M. and Alhomoud A., 1984b. Impingement Heat Transfer at a Circular Cylinder Due to An Offset or Non-Offset Slot Jet. *Int. J. Heat Mass Transfer*, 27(12), pp. 2297-2306.
- Stasiek, J., Collins, M. W., Ciofalo, M. and Chew, P. E., 1996. Investigation of Flow and Heat Transfer in Corrugated Passages - I. Experimental Results. *Int. J. Heat Mass Transfer*, 39(1), pp.149-164.
- Tarasuk, J. D. and Castle, G. S. P., 1983. Temperature Distribution in an Electrically Heated Wide Metallic Foil. *J. of Heat Transfer*, 105, pp. 210-212.
- Thomann, H., 1968. Effect of Streamwise Wall Curvature on Heat Transfer in a Turbulent Boundary Layer. *J. Fluid Mech.*, 33, part 2, pp. 283-292.
- Toy, N. and Savory, E., 1992. Quantitative Assessment of Surface Temperatures Using Liquid Crystals and Digital Imaging. *Optical Methods and Data Processing in Heat and Fluid Flow*, April 2-3, IMechE, London, pp. 141-144.
- Valencia, A., Fiebig, M. and Mitra, N. K., 1995. Influence of Heat Conduction on Determination of Heat Transfer Coefficient by Liquid Crystal Thermography. *Experimental Heat Transfer*, 8, pp. 271-279.
- Van Heiningen A. R. J., Mujumdar, A. S. and Douglas, W. J. M., 1976. Numerical Prediction of the Flow Field and Impingement Heat Transfer Caused by a Laminar Slot Jet. *Trans ASME*, pp.654-658

- Vedula, R. P., Metzger, D. E. and Bickford, W. B., 1988. Effects of Lateral and Anisotropic Conduction on Determination of Local Convection Heat Transfer Characteristics with Transient Tests and Surface Coatings. *Winter Annual Meeting of ASME*, Chicago, USA, Nov 27 - Dec 2, HTD-I, pp. 21-27
- Viskanta, R., 1993. Heat Transfer to Impinging Isothermal Gas and Flame Jets. *Experimental Thermal and Fluid Science*, **6**, pp. 111-134.
- Wang, Z., Ireland, P. T. and Jones, T. V., 1995. An Advanced Method of processing Liquid Crystal Video Signals from Transient Heat Transfer Experiments. *J. of Turbomachinery*, **117**, pp. 184-189.
- Wang, Z., Ireland, P. T., Jones, T. V. and Davenport, R., 1996. A Color Image Processing System for Transient Liquid Crystal Heat Transfer Experiments. *J. of Turbomachinery*, **118**, pp. 421-427.
- Walz, D. R., 1964. Spot Cooling and Heating of Surfaces with High Velocity Impinging Air Jets: Part 2- Circular Jets on Plane and Curved Surfaces Slot Jets on Curved Surfaces. *Technical Report No.61*, Stanford University, USA, July, 111pp.
- Whitaker, K. W., 1992. A Study of the Heat Transfer Resulting from a Heated Jet Impinging upon a Cylinder. *PhD Thesis*, Texas A&M University, USA.
- Whitney, C., 1995. Heat Transfer Characteristics of Slot Jet Impingement. *PhD Thesis*. The Nottingham Trent University, UK.
- Wilson, D. J. and Goldstein, R. J., 1976. Turbulent Wall Jets with Cylindrical Streamwise Surface Curvature. *ASME Paper No. 76-FE-O*, pp. 550-557.

Bibliography

- Abramovich, G.N., 1963. *The Theory of Turbulent Jets*. MIT Press.
- Astin, A. V., 1954. *Tables of the Error Function and its Derivative*. National Bureau of Standard Applied, Applied Mathematics Series 41, Dept. of Commerce, USA.
- Bird, B. R., Stewart, W. E. and Lightfoot, E. N., 1960. *Transport Phenomena*. John Wiley & Sons, New York.
- Bradshaw, P., 1971. *An Introduction to Turbulence and its Measurement*. Pergamon Press.
- Bruun, H. H., 1995. *Hot-Wire Anemometry- Principles and Signal Analysis*. Oxford University Press, Oxford.
- CHAM Ltd., 1990. *The PHOENICS-Instruction Course Notes- CHAM/TR300*, London.
- CHAM Ltd., 1991. *The PHOENICS-Reference Manual-CHAM/TR200*, London.
- Coleman, H. W., and Steele, W. G., 1989. *Experimentation and Uncertainty Analysis for Engineers*. Wiley, New York.
- de Boer, J. B. and Fischer, D., 1981. *Interior Lighting*. Philips Technical Library, Kluwer Technical Books, New York.
- Gautschi, W., 1954. Error Function and Fresnel Integrals. *Handbook of Mathematical Functions with Formulas, Graphs and Mathematical Tables*, Dover Publications Inc..
- Hunt, R. W. G., 1991. *Measuring Colour*, Ellis Horwood, New York.
- Kasagi, N., Moffat, R.J. and Hirata, M., 1989. Liquid Crystals, *Handbook of Flow Visualization* (ed. by Yang, N. J.), Hemisphere, New York.
- Kreith, F. and Black, W. Z., 1980. *Basic Heat Transfer*. Harper and Row, New York.
- Launder, B. E. and Spalding, D. B., 1972. *Lectures in Mathematical Models of Turbulence*. Academic Press, London.
- Millerson, G., 1991. *The Technique of Lighting for Television and Film*. 3rd Ed. Focal Press, England.
- Pantankar, S. V., 1980. *Numerical Heat Transfer and Fluid Flow*. Hemisphere Publishing Co., New York.

Perry, A. E., 1982. *Hot Wire Anemometry*. Clarendon Press, Oxford.

Rodi, W., 1993. *Turbulence Models and Their Application in Hydraulics - A State of the Art Review*. IAHR, Balkema A. A. Publishers.

Schlichting, H., 1979. *Boundary Layer Theory*. 7th Ed. McGraw Hill, New York.

Shaw, C. T., 1992. *Using Computational Fluid Dynamics*. Prentice Hall, New York.

Spalding, D. B., 1991. *The PHOENICS Beginner's Guide- CHAM/TR100*, CHAM Ltd., London.

Sproson, W. N., 1983. *Colour Science in Television and Display Systems*. Adam Hilger Ltd., Bristol.

Appendix A- Profile coordinates of slot nozzle contraction

TRUE LENGTH, L = 153.2375 mm
 INLET WIDTH, D1 = 125 mm
 OUTLET WIDTH, D2 = 6.25 mm
 THE STREAM FUNCTION, PSI = 0.5

EPSILON = 0.6558857
 Q (inlet) = -6.167054
 Q (outlet) = 6.167077
 TRUE LENGTH = 153.2375

REF.	X VALUE, mm	Y VALUE, mm
1	0	3.125
2	0.3851034	3.127484
3	0.7702118	3.135038
4	1.155336	3.147967
5	1.540483	3.1668
6	1.925667	3.192301
7	2.310909	3.225512
8	2.696236	3.267779
9	3.081692	3.320824
10	3.467344	3.38681
11	3.853288	3.468416
12	4.239667	3.568964
13	4.626696	3.692539
14	5.014703	3.844162
15	5.404164	4.029986
16	5.795807	4.257542
17	6.190705	4.53603
18	6.590483	4.876665
19	6.997531	5.293109
20	7.415435	5.801919
21	7.849541	6.423106
22	8.307732	7.180673
23	8.801705	8.103127
24	9.3486	9.22383
25	9.973322	10.58088
26	10.71159	12.21622
27	11.61359	14.17318
28	12.74763	16.49175
29	14.2028	19.20067

30	16.08794	22.30618
31	18.52413	25.779
32	21.62834	29.5444
33	25.49002	33.48182
34	30.14828	37.43946
35	35.58062	41.2613
36	41.70959	44.81583
37	48.42327	48.01469
38	55.59974	50.81624
39	63.1256	53.21741
40	70.90601	55.24107
41	78.86707	56.92378
42	86.95383	58.30705
43	95.12692	59.43161
44	103.3587	60.33445
45	111.6301	61.04741
46	119.9279	61.59674
47	128.243	62.00327
48	136.5691	62.28279
49	144.9018	62.44619
50	153.2375	62.49996

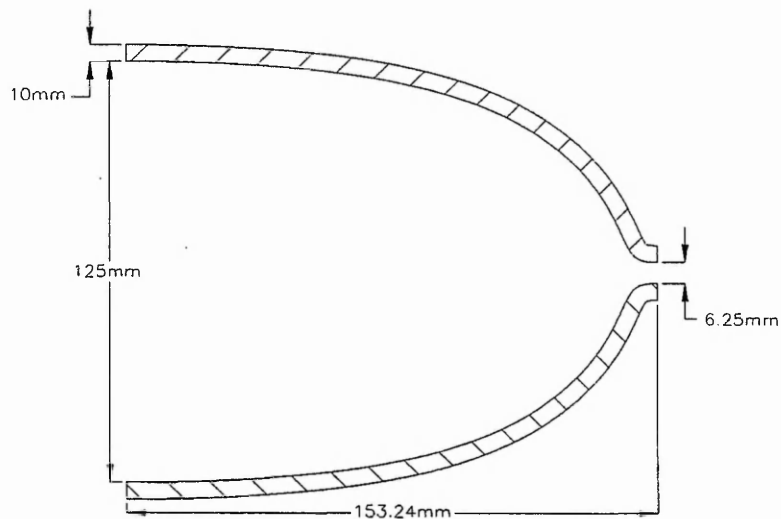


Figure A.1 Schematic diagram of the slot nozzle contraction in horizontal direction.

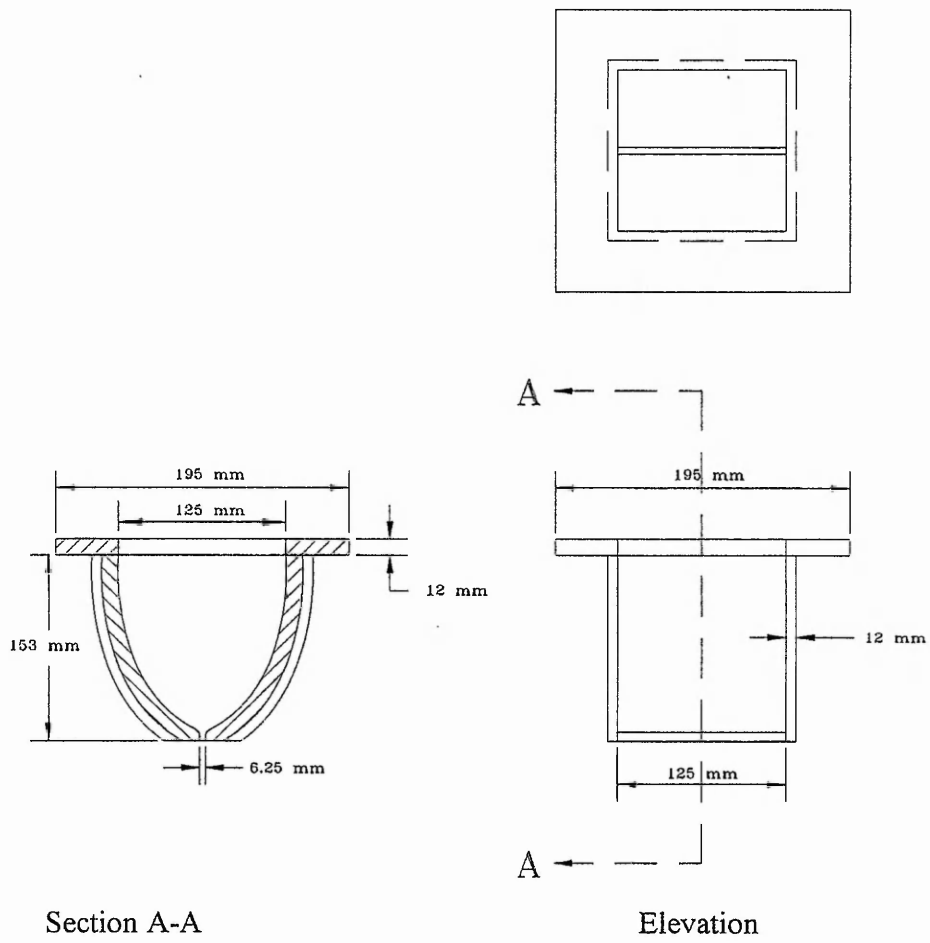


Figure A.2 Schematic diagram of the slot nozzle configuration in vertical direction.

Commands of the Calibration and Transient Programs

Two programs Calibration (Calib.c) and Transient (Trans.c) have been developed to obtain the relationship among the temperature, hue and video camera viewing angle of thermochromic liquid crystals, and determine the surface heat transfer information from a liquid crystal thermographic image in real time capture or from video tape recording.

These two programs have more than 36 command functions specifically developed for the present study as shown in Table B.1. For easier explanation, each command key is presented in a screen format.

Source codes in MS-C language are available either from the author:

Dr. T. L. Chan
 Department of Mechanical Engineering
 The Hong Kong Polytechnic University
 Hung Hom, Kowloon
 Hong Kong
 E-mail: mmtchan@polyu.edu.hk

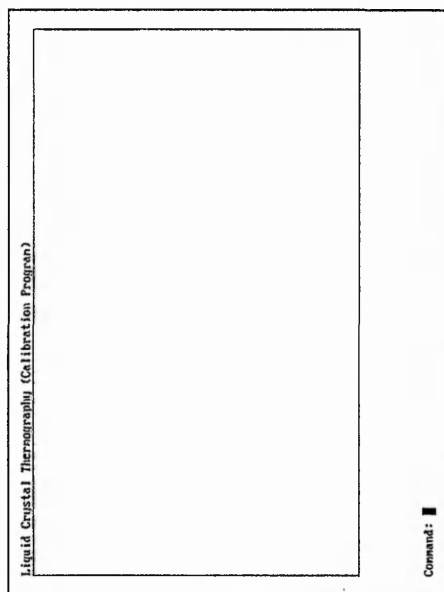
Or from
 Dr. K. Jambunathan
 Department of Mechanical Engineering
 The Nottingham Trent University
 Nottingham, NG1 4BU
 United Kingdom
 E-mail: nath.jambunathan@ntu.ac.uk

B.1 Calibration program commands user menu in screen format
 B.2 Transient program commands user menu in screen format

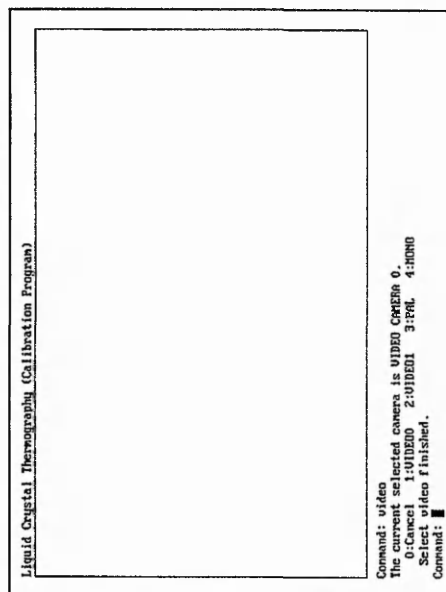
Calibration Program Command Functions Screen Display- Appendix B.1

	Calibration Program Command	Transient Program Command
1	Cclear	Centre
2	Cdefine	Dir
3	Cdelete	Exit
4	Cmap	Filter
5	Crestore	Grab
6	Csave	HT_value
7	Exit	Matrix
8	Dir	Objectmode
9	Grab	Restore
10	Hclear	Rrestore
11	Hdefine	Save
12	Hdelete	Scale
13	Hrestore	Sname
14	Hsave	Snap
15	Hscan	Symmetry
16	Hshow	Video
17	Snap	Writemode
18	Trestore	
19	Video	

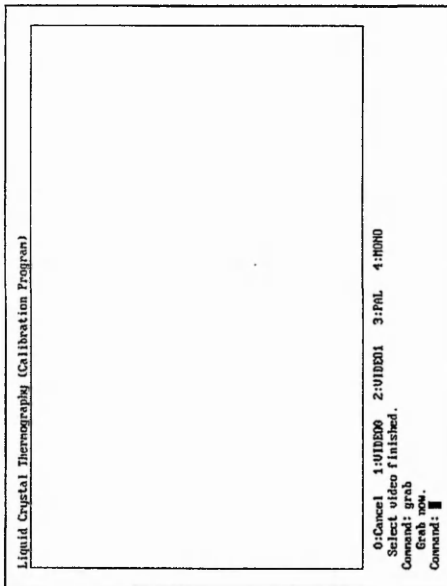
Table B.1. Program command functions



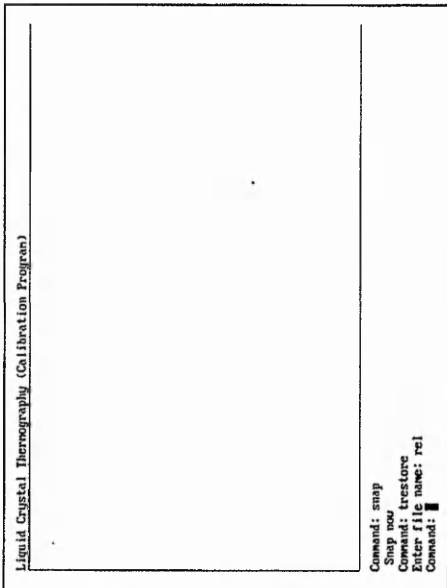
Calibration Program Start Screen



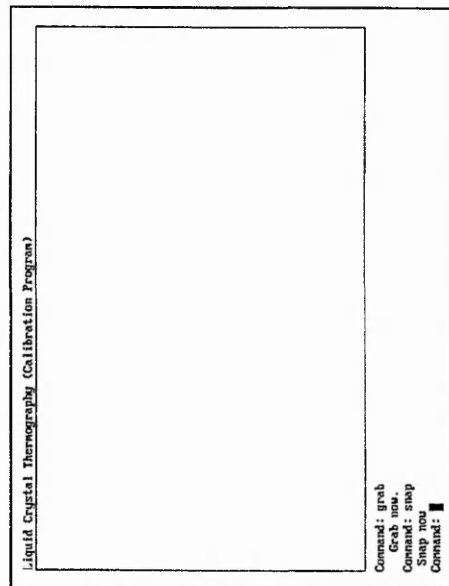
Command 'Video' Screen



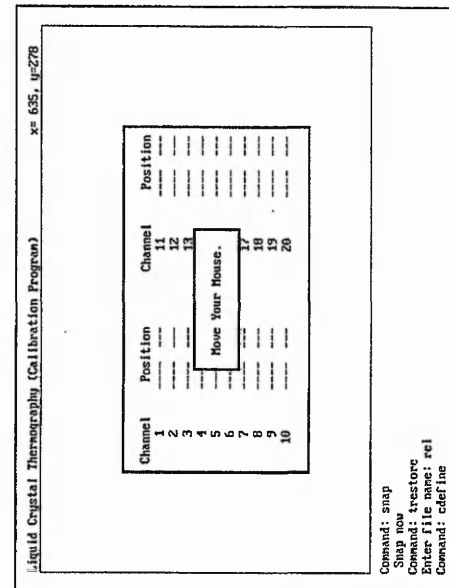
Command 'Grab' Screen



Command 'Trestore' Screen



Command 'Snap' Screen



Command 'Cdefine' Screen 1

Liquid Crystal Thermography (Calibration Program) x= 677, y=553

Channel	Position	Channel	Position
1	759 348	11
2	12
3	13
4	14
5	15
6	16
7	17
8	18
9	19
10	20

Command: cdefine
 Position: 759, 348
 which channel? (1-20): 1
 continue?(y/n) y

Command 'Cdefine' Screen 2

Liquid Crystal Thermography (Calibration Program) x= 561, y=348

Channel	Position	Channel	Position
1	759 348	11
2	12
3	13
4	14
5	15
6	16
7	17
8	18
9	19
10	20

which channel? (1-20): 1
 continue?(y/n) y
 Position: 561, 348
 which channel? (1-20): █

Command 'Cdefine' Screen 3

Liquid Crystal Thermography (Calibration Program) x= 561, y=348

Channel	Position	Channel	Position
1	759 348	11
2	561 348	12
3	13
4	14
5	15
6	16
7	17
8	18
9	19
10	20

continue?(y/n) y
 Position: 561, 348
 which channel? (1-20): 2
 continue?(y/n) █

Command 'Cdefine' Screen 4

Liquid Crystal Thermography (Calibration Program) x= 158, y=154

Channel	Position	Channel	Position
1	759 348	11	354 252
2	561 348	12	154 252
3	457 348	13	56 252
4	255 348	14	663 154
5	154 348	15	562 154
6	56 348	16	464 154
7	769 252	17	369 154
8	663 252	18	269 154
9	562 252	19	169 154
10	466 252	20

continue?(y/n) y
 Position: 158, 154
 which channel? (1-20): 19
 continue?(y/n) █

Command 'Cdefine' Screen 5

Liquid Crystal Thermography (Calibration Program) x= 157, y=157

Channel	Position	Channel	Position
1	759 348	11	356 252
2	561 348	12	154 252
3	457 348	13	56 252
4	255 348	14	663 154
5	154 348	15	562 154
6	56 348	16	464 154
7	760 252	17	360 154
8	659 252	18	260 154
9	562 252	19	158 154
10	460 252	20	

Command:
 Command: csave
 Command: Enter file name: channel
 Command: cdelete
 Command: Delete which channel? (1-20): 19

Command 'Cdefine' Screen 6

Liquid Crystal Thermography (Calibration Program) x= 157, y=157

Channel	Position	Channel	Position
1	759 348	11	356 252
2	561 348	12	154 252
3	457 348	13	56 252
4	255 348	14	663 154
5	154 348	15	562 154
6	56 348	16	464 154
7	760 252	17	360 154
8	659 252	18	260 154
9	562 252	19	158 154
10	460 252	20	

Command:
 Command: csave
 Command: Enter file name: channel

Command 'Csave' Screen 1

Liquid Crystal Thermography (Calibration Program) x= 157, y=157

Channel	Position	Channel	Position
1	759 348	11	356 252
2	561 348	12	154 252
3	457 348	13	56 252
4	255 348	14	663 154
5	154 348	15	562 154
6	56 348	16	464 154
7	760 252	17	360 154
8	659 252	18	260 154
9	562 252	19	158 154
10	460 252	20	

Command:
 Command: csave
 Command: Enter file name: channel
 Command: cdelete
 Command: Delete which channel? (1-20): 19

Command 'Csave' Screen 2

Liquid Crystal Thermography (Calibration Program) x= 157, y=157

Channel	Position	Channel	Position
1	759 348	11	356 252
2	561 348	12	154 252
3	457 348	13	56 252
4	255 348	14	663 154
5	154 348	15	562 154
6	56 348	16	464 154
7	760 252	17	360 154
8	659 252	18	260 154
9	562 252	19	158 154
10	460 252	20	

Command:
 Command: csave
 Command: Enter file name: channel
 Command: cdelete
 Command: Delete which channel? (1-20): 19

Command 'Csave' Screen 3

Liquid Crystal Thermography (Calibration Program) x= 157, y=157

Channel	Position	Channel	Position
1	759 348	11	356 252
2	561 348	12	154 252
3	457 348	13	56 252
4	255 348	14	663 154
5	154 348	15	562 154
6	56 348	16	464 154
7	760 252	17	360 154
8	659 252	18	260 154
9	562 252	19	---
10	460 252	20	---

Enter file name: channel
 Command: cdelete
 Delete which channel? (1-20): 19
 Command: cdelete
 Delete which channel? (1-20): 8
 Command: cdelete
 Delete which channel? (1-20): 0

Command 'Cdelete' Screen 1

Liquid Crystal Thermography (Calibration Program) x= 157, y=157

Channel	Position	Channel	Position
1	759 348	11	356 252
2	561 348	12	154 252
3	457 348	13	56 252
4	255 348	14	663 154
5	154 348	15	562 154
6	56 348	16	464 154
7	760 252	17	360 154
8	659 252	18	260 154
9	562 252	19	---
10	460 252	20	---

Command: cdelete
 Delete which channel? (1-20): 19
 Command: cdelete
 Delete which channel? (1-20): 8
 Command: █

Command 'Cdelete' Screen 2

Liquid Crystal Thermography (Calibration Program) x= 157, y=157

Channel	Position	Channel	Position
1	759 348	11	356 252
2	561 348	12	154 252
3	457 348	13	56 252
4	255 348	14	663 154
5	154 348	15	562 154
6	56 348	16	464 154
7	760 252	17	360 154
8	659 252	18	260 154
9	562 252	19	---
10	460 252	20	---

Command: cdelete
 Delete which channel? (1-20): 19
 Command: cdelete
 Delete which channel? (1-20): 8
 Command: cclear

Command 'Cclear' Screen 1

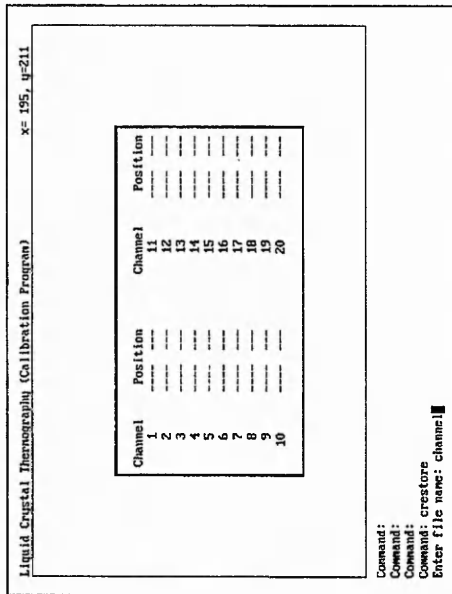
Liquid Crystal Thermography (Calibration Program) x= 157, y=157

Channel	Position	Channel	Position
1	759 348	11	356 252
2	561 348	12	154 252
3	457 348	13	56 252
4	255 348	14	663 154
5	154 348	15	562 154
6	56 348	16	464 154
7	760 252	17	360 154
8	659 252	18	260 154
9	562 252	19	---
10	460 252	20	---

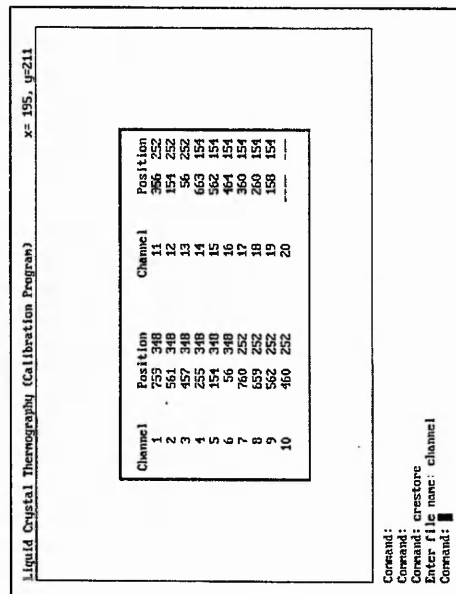
Really want to delete all?
 0 to cancel, any key to continue...

Command: cdelete
 Delete which channel? (1-20): 19
 Command: cdelete
 Delete which channel? (1-20): 8
 Command: cclear

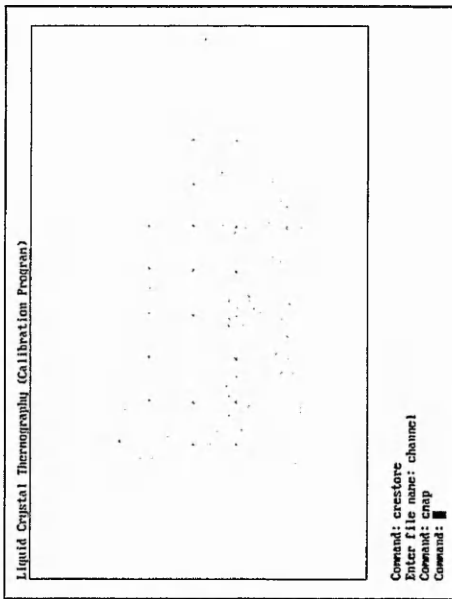
Command 'Cclear' Screen 2



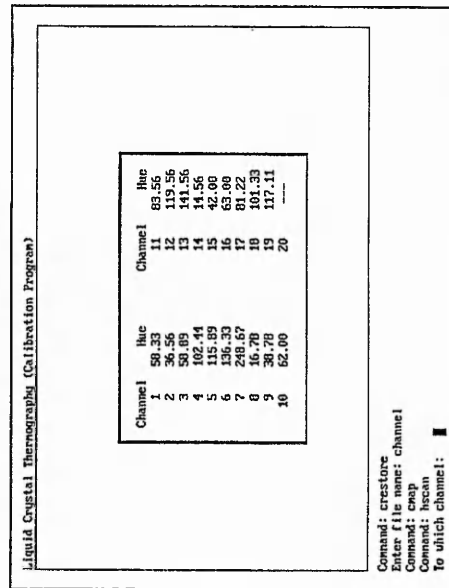
Command 'Crestore' Screen 1



Command 'Crestore' Screen 2



Command 'Cmap' Screen



Command 'Hscan' Screen 1

Liquid Crystal Thermography (Calibration Program)

Channel	Hic	Channel	Hic
1	7.67	11	84.33
2	41.22	12	113.67
3	66.33	13	140.22
4	91.56	14	17.67
5	109.22	15	44.22
6	125.11	16	63.56
7	141.44	17	81.00
8	16.78	18	95.56
9	37.78	19	112.89
10	61.56	20	---

Command: grab
 Grab now.
 Command: hscan
 ID which channel: 19
 Channel: 1
 Temperature: 36.8

Command 'Hscan' Screen 2

Liquid Crystal Thermography (Calibration Program)

Channel	Hic	Channel	Hic
1	7.67	11	84.33
2	41.22	12	113.67
3	66.33	13	140.22
4	91.56	14	17.67
5	109.22	15	44.22
6	125.11	16	63.56
7	141.44	17	81.00
8	16.78	18	95.56
9	37.78	19	112.89
10	61.56	20	---

To which channel: 19
 Channel: 1
 Angle: 0.00
 Enter to accept, d to redifine

Command 'Hscan' Screen 3

Liquid Crystal Thermography (Calibration Program)

Channel	Hic	Channel	Hic
1	7.67	11	84.33
2	41.22	12	113.67
3	66.33	13	140.22
4	91.56	14	17.67
5	109.22	15	44.22
6	125.11	16	63.56
7	141.44	17	81.00
8	16.78	18	95.56
9	37.78	19	112.89
10	61.56	20	---

Channel: 1
 Temperature: 36.8
 Angle: 0.00
 Enter to accept, d to redifine
 Channel: 2
 Temperature: 37.4

Command 'Hscan' Screen 4

Liquid Crystal Thermography (Calibration Program)

Channel	Hic	Channel	Hic
1	7.67	11	84.33
2	41.22	12	113.67
3	66.33	13	140.22
4	91.56	14	17.67
5	109.22	15	44.22
6	125.11	16	63.56
7	141.44	17	81.00
8	16.78	18	95.56
9	37.78	19	112.89
10	61.56	20	---

Channel: 15
 Temperature: 36.3
 Channel: 16
 Temperature: 36.5
 Channel: 17
 Temperature: 37
 Channel: 18
 Temperature: 37.5
 Channel: 19
 Temperature: ---

Command 'Hscan' Screen 5

Liquid Crystal Thermography (Calibration Program)

Channel	Huc	Channel	Huc
1	61.00	11	67.89
2	65.00	12	69.007
3	63.00	13	64.002
4	62.00	14	62.00
5	67.002	15	65.00
6	65.001	16	71.00
7	64.334	17	65.00
8	61.00	18	65.33
9	64.00	19	64.009
10	63.00	20	---

Channel: 16 Temperature: 36.5
 Channel: 17 Temperature: 37
 Channel: 18 Temperature: 37.5
 Channel: 19 Temperature: 38.2
 To which channel: █

Command 'Hscan' Screen 6

Liquid Crystal Thermography (Calibration Program)

Channel	Huc	Channel	Huc
1	10.000	11	78.44
2	41.56	12	112.11
3	65.56	13	127.33
4	94.67	14	23.00
5	115.78	15	46.89
6	135.86	16	67.33
7	141.00	17	67.33
8	24.33	18	100.56
9	46.44	19	117.89
10	67.56	20	---

Which channel: 1 Temperature: 36.6
 Angle : 0.09
 Enter to accept, d to redef ine
 Which channel: 2 Temperature: 37.4 █

Command 'Hdefine' Screen 2

Liquid Crystal Thermography (Calibration Program)

Channel	Huc	Channel	Huc
1	9.0000	11	78.67
2	45.33	12	112.00
3	62.78	13	134.22
4	93.22	14	28.56
5	107.22	15	43.78
6	128.78	16	64.22
7	148.994	17	84.67
8	22.22	18	102.11
9	41.33	19	120.89
10	64.67	20	---

Command: Hdefine
 Which channel: 1 Temperature: 36.6
 Angle : 0.00
 Enter to accept, d to redef ine
 █

Command 'Hdefine' Screen 1

Liquid Crystal Thermography (Calibration Program)

Channel	Huc	Channel	Huc
1	10.000	11	78.44
2	41.56	12	112.11
3	65.56	13	127.33
4	94.67	14	23.00
5	115.78	15	46.89
6	135.86	16	67.33
7	141.00	17	67.33
8	24.33	18	100.56
9	46.44	19	117.89
10	67.56	20	---

Which channel: 2 Temperature: 37.4
 Angle : 0.00
 Enter to accept, d to redef ine
 █

Command 'Hdefine' Screen 3

Liquid Crystal Thermography (Calibration Program)

Presentation of unprocessed data

POINT	Hue	Temp	Chan	Angle	POINT	Hue	Temp	Chan	Angle
1	9.0	36.21	1	0.00	16	109.2	37.47	4	0.00
2	16.8	40.64	7	0.00	17	112.9	37.07	18	0.00
3	17.7	41.10	13	0.00	18	113.0	38.85	1	0.00
4	37.8	34.25	8	0.00	19	113.7	37.01	11	0.00
5	41.2	36.49	1	0.00	20	125.1	30.95	5	0.00
6	41.5	36.19	2	0.00	21	140.2	38.21	12	0.00
7	44.5	36.47	2	0.00	22	141.4	38.88	6	0.00
8	60.3	36.47	2	0.00					
9	61.6	36.01	9	0.00					
10	63.6	36.52	15	0.00					
11	81.0	37.06	16	0.00					
12	84.3	36.74	10	0.00					
13	91.5	36.42	3	0.00					
14	95.6	37.69	17	0.00					
15	104.8	36.17	13	0.00					

Total points: 22 ENTER to exit the function.

Angle : 0.00
Enter to accept, d to redefine

Which channel:
Command: hshow

Command 'Hshow' Screen

Liquid Crystal Thermography (Calibration Program)

Channel	Hue	Channel	Hue
1	9.2208	11	86.33
2	46.00	12	115.00
3	84.30	13	125.22
4	94.44	14	25.11
5	103.67	15	45.67
6	123.11	16	65.78
7	8.7894	17	77.78
8	21.44	18	97.896
9	46.33	19	112.44
10	66.11	20	---

Which channel:
Command: hshow
Command: hdelete
Enter point to delete: 21

Command 'Hdelete' Screen 1

Liquid Crystal Thermography (Calibration Program)

Presentation of unprocessed data

POINT	Hue	Temp	Chan	Angle	POINT	Hue	Temp	Chan	Angle
1	9.0	36.21	1	0.00	16	109.2	37.47	4	0.00
2	16.8	40.64	7	0.00	17	112.9	37.07	18	0.00
3	17.7	41.10	13	0.00	18	113.0	38.85	1	0.00
4	37.8	34.25	8	0.00	19	113.7	37.01	11	0.00
5	41.2	36.49	1	0.00	20	125.1	30.95	5	0.00
6	41.5	36.19	2	0.00	21	141.4	38.88	6	0.00
7	44.5	36.47	2	0.00					
8	60.3	36.47	2	0.00					
9	61.6	36.01	9	0.00					
10	63.6	36.52	15	0.00					
11	81.0	37.06	16	0.00					
12	84.3	36.74	10	0.00					
13	91.5	36.42	3	0.00					
14	95.6	37.69	17	0.00					
15	104.8	36.17	13	0.00					

Total points: 21 ENTER to exit the function.

Command: hshow
Command: hdelete
Enter point to delete: 21
Command: hshow

Command 'Hdelete' Screen 2

Liquid Crystal Thermography (Calibration Program)

Channel	Hue	Channel	Hue
1	9.2208	11	86.33
2	46.00	12	115.00
3	84.30	13	125.22
4	94.44	14	25.11
5	103.67	15	45.67
6	123.11	16	65.78
7	8.7894	17	77.78
8	21.44	18	97.896
9	46.33	19	112.44
10	66.11	20	---

Enter point to delete: 20
Command: hshow
Command: hsave
Enter title name: hue

Command 'Hsave' Screen

Liquid Crystal Thermography (Calibration Program)

Name	Size
CHANNEL	B4
C7.MRP	3350
CS.DBJ	38622
C7.MRP	68247
CS.DBJ	3350
CS.MRP	38622
CS.C	68247
CS.MRP	3350
CS.C	68247
CHL1898.DBJ	1273
CHKDUP.DBT	247038
CS.DBJ	508
MRP	508
CHKC.TXT	505
CS.DBJ	38622
CS.DBJ	38622

Channel	huc
11	86.33
12	115.00
13	136.22
14	25.11
15	45.67
16	65.78
17	57.86
18	77.78
19	112.44
20	---

Enter file name: huc
 Command: fashor
 Path(only if spec): c:\noncapt\cal\lv.*

Command 'Dir' Screen 1

Liquid Crystal Thermography (Calibration Program)

Channel	huc	Channel	huc
1	9.2200	11	86.33
2	46.00	12	115.00
3	65.11	13	136.22
4	94.44	14	25.11
5	103.67	15	45.67
6	123.11	16	65.78
7	8.7884	17	77.78
8	21.44	18	97.896
9	46.33	19	112.44
10	66.11	20	---

Total Size = 1314563
 Command: exit

Command 'Exit' Screen

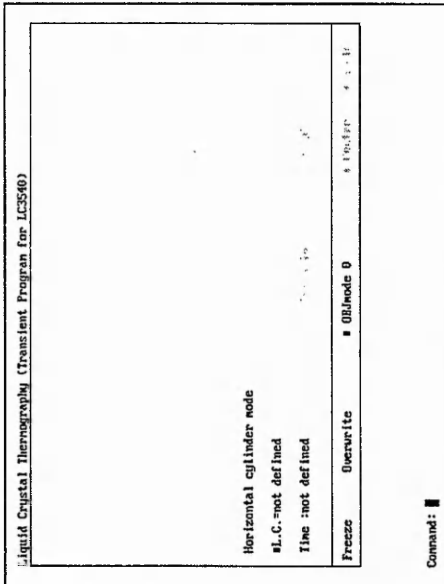
Liquid Crystal Thermography (Calibration Program)

Channel	huc	Channel	huc
1	9.2200	11	86.33
2	46.00	12	115.00
3	65.11	13	136.22
4	94.44	14	25.11
5	103.67	15	45.67
6	123.11	16	65.78
7	8.7884	17	77.78
8	21.44	18	97.896
9	46.33	19	112.44
10	66.11	20	---

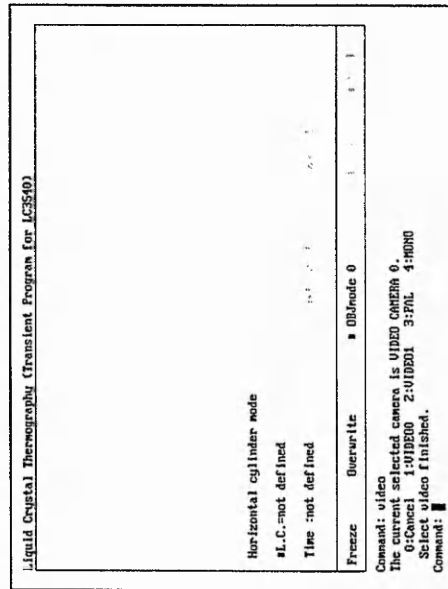
Total Size = 1314563
 Command: █

Command 'Dir' Screen 2

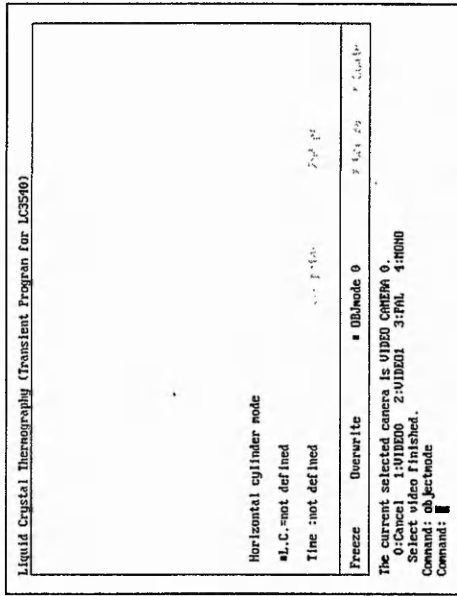
Transient Program Command Functions Screen Display- Appendix B.2



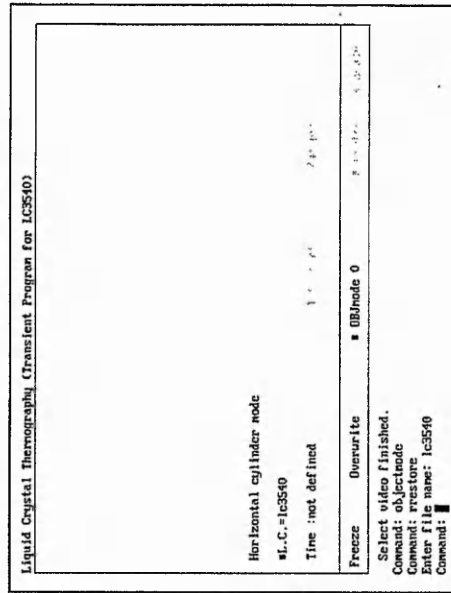
Transient Program Start Screen



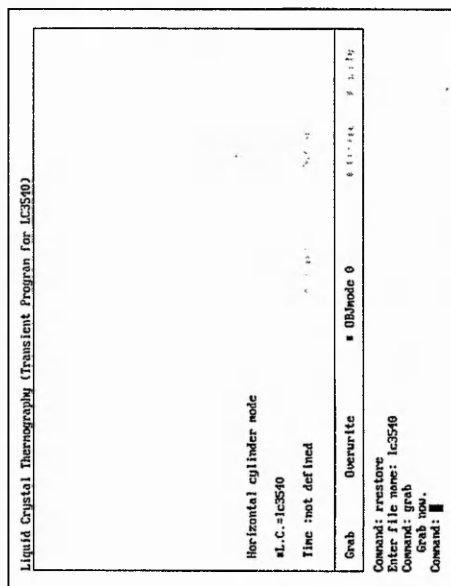
Command 'Video' Screen



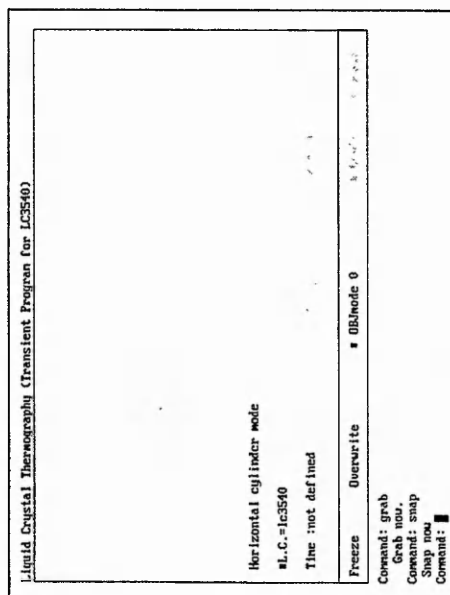
Command 'Objectmode' Screen



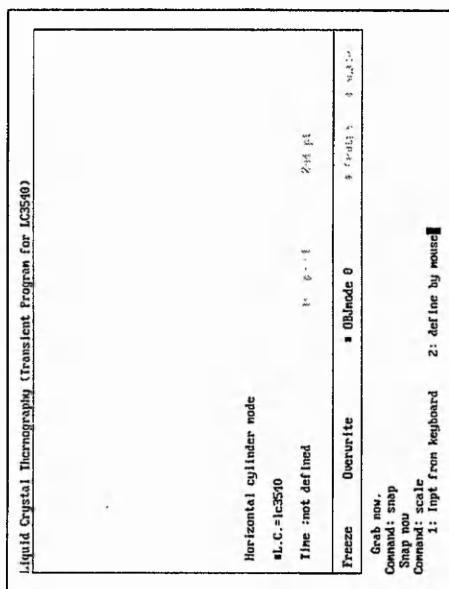
Command 'Restore' Screen



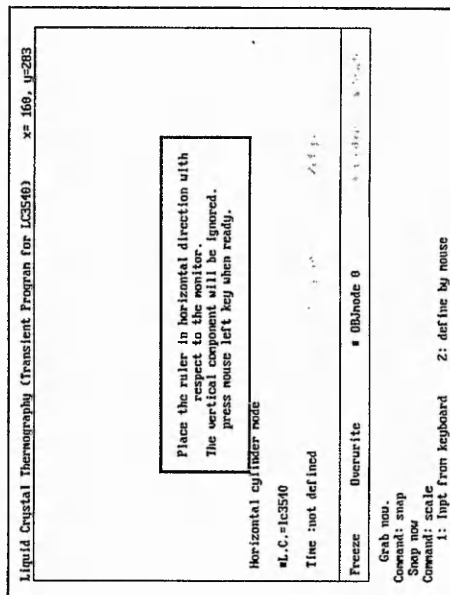
Command 'Grab' Screen



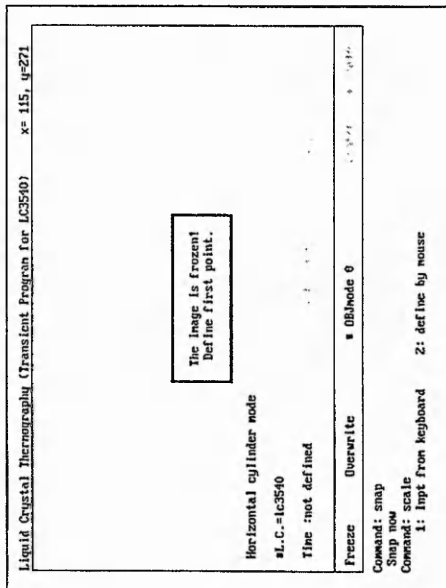
Command 'Snap' Screen



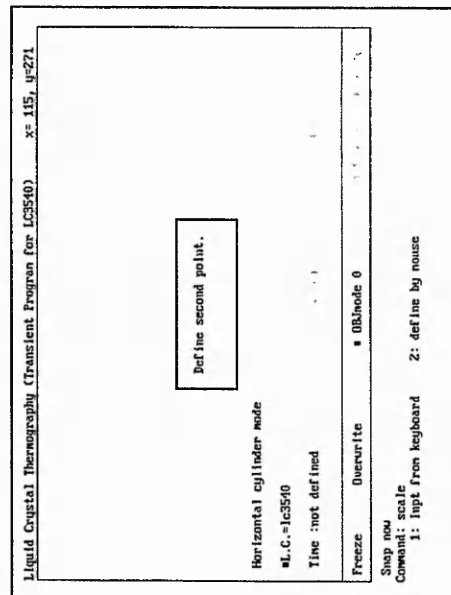
Command 'Scale' Screen 1



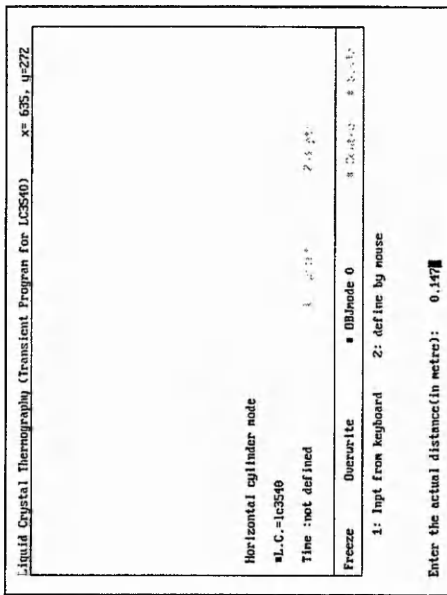
Command 'Scale' Screen 2



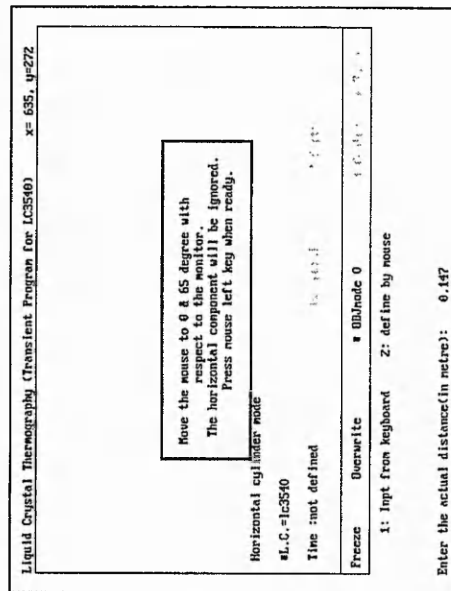
Command 'Scale' Screen 3



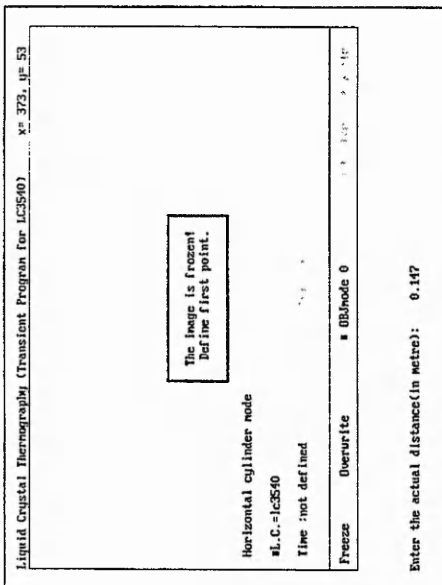
Command 'Scale' Screen 4



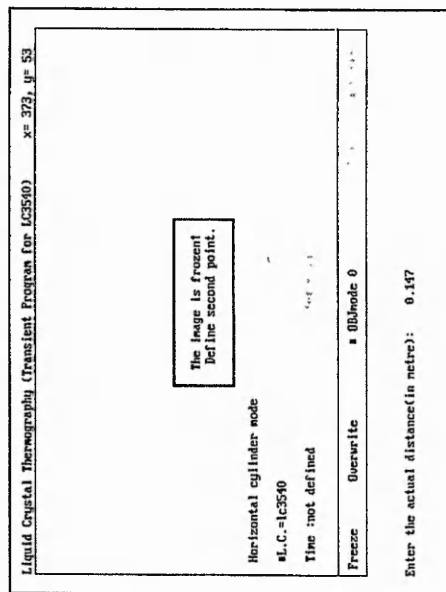
Command 'Scale' Screen 5



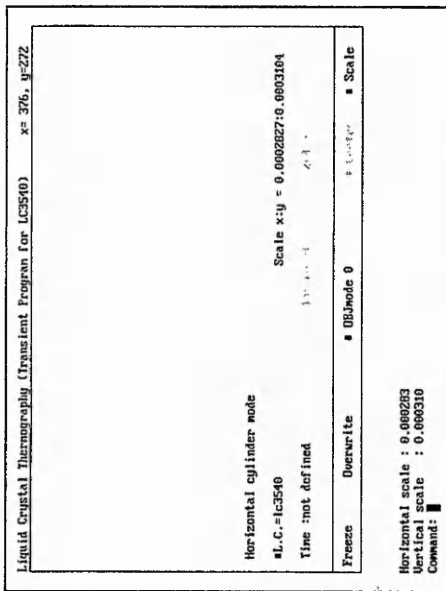
Command 'Scale' Screen 6



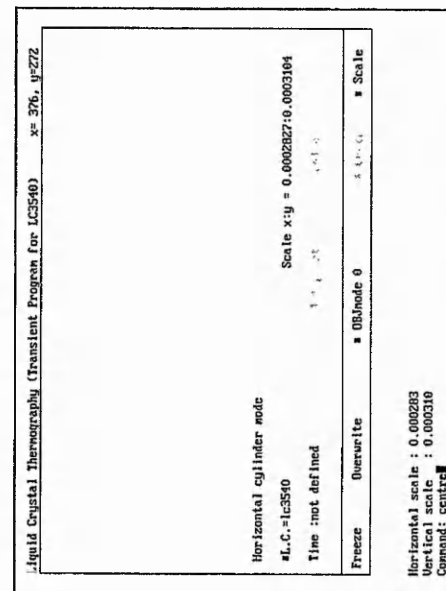
Command 'Scale' Screen 7



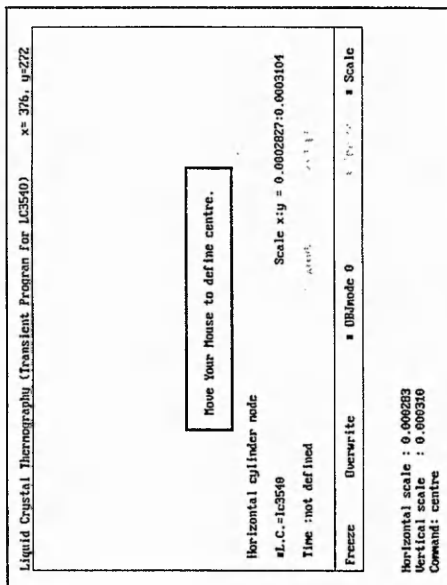
Command 'Scale' Screen 8



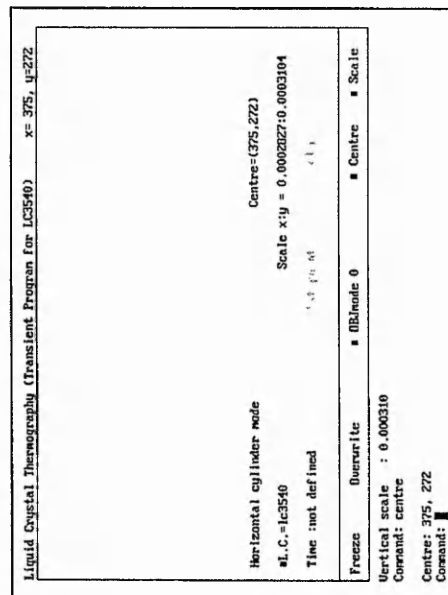
Command 'Scale' Screen 9



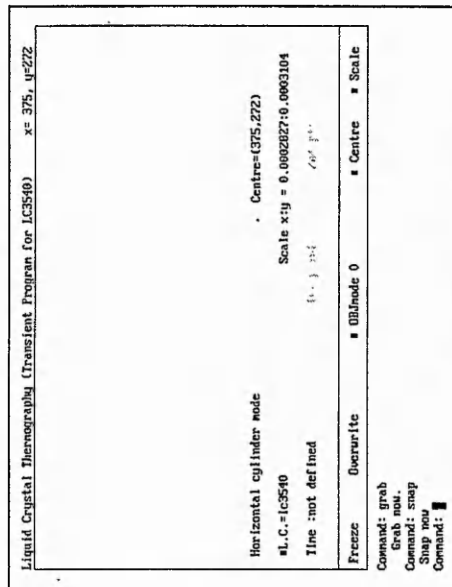
Command 'Centre' Screen 32



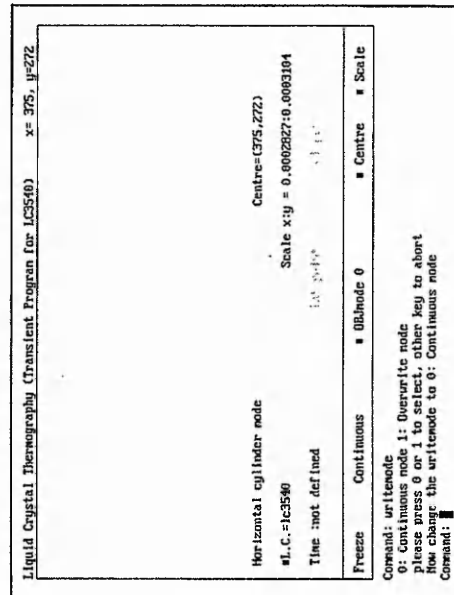
Command 'Centre' Screen 2



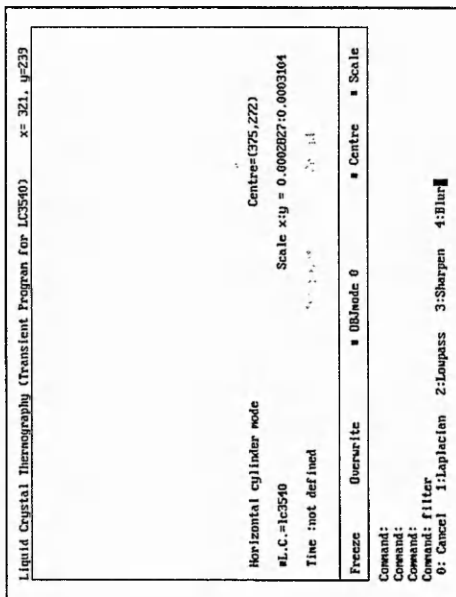
Command 'Centre' Screen 3



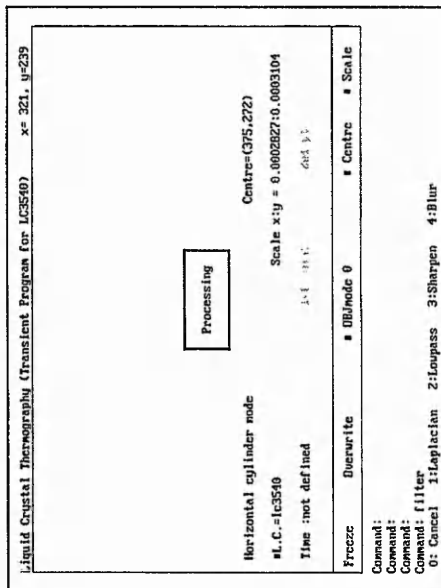
Command 'Grab' and 'Snap' Screen



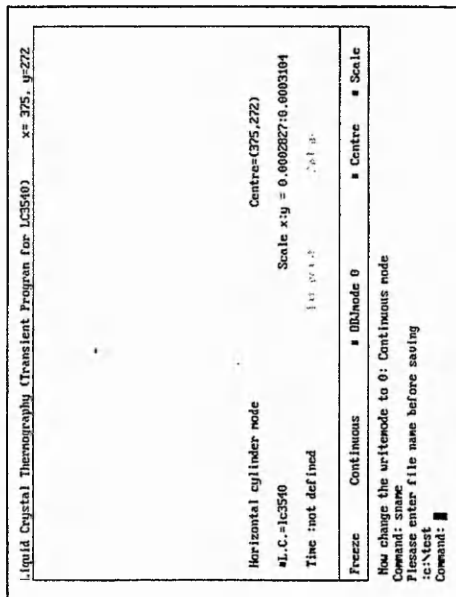
Command 'Write mode' Screen



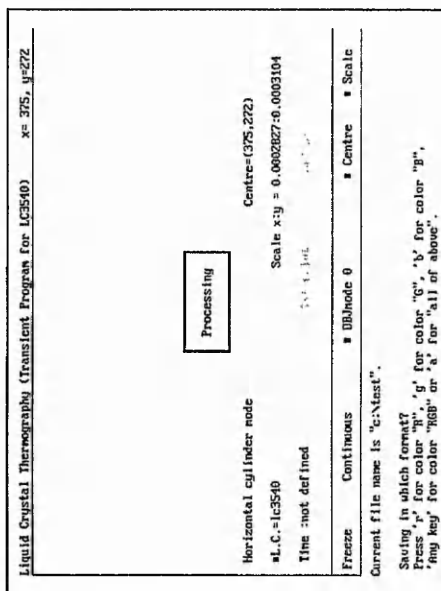
Command 'Filter' Screen 1



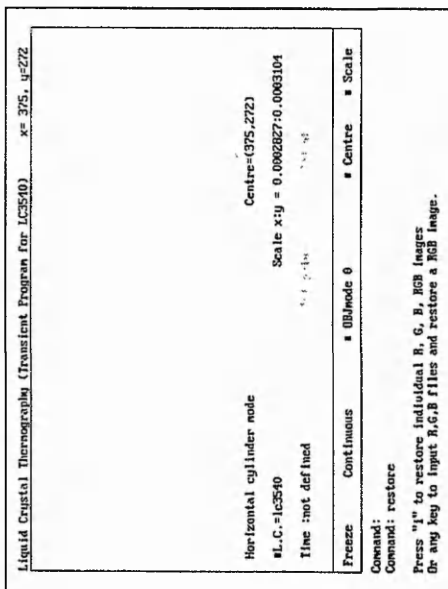
Command 'Filter' Screen 2



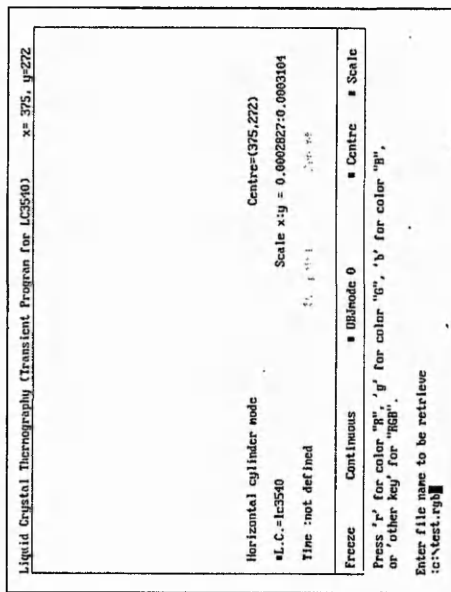
Command 'Sname' Screen



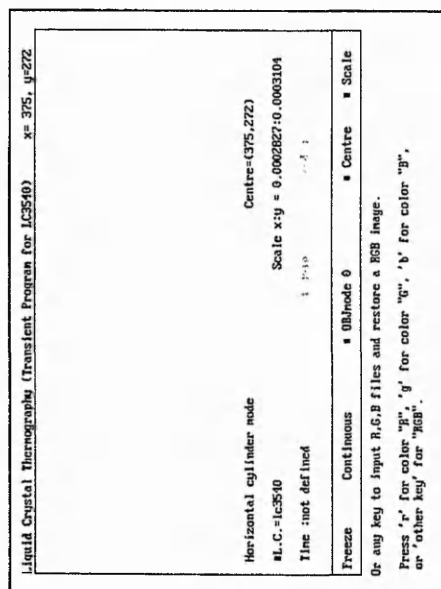
Command 'Save' Screen



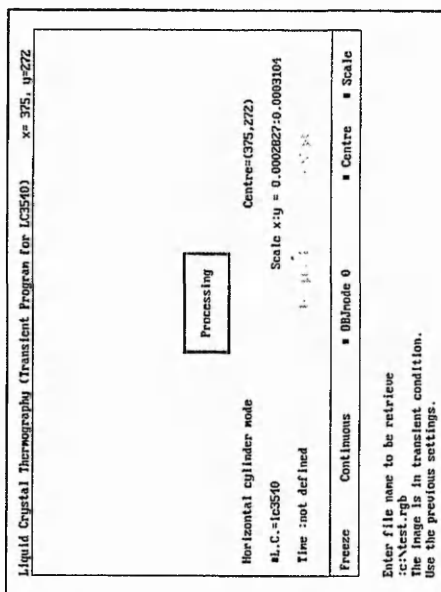
Command 'Restore' Screen 1



Command 'Restore' Screen 3



Command 'Restore' Screen 2



Command 'Restore' Screen 4

Liquid Crystal Thermography (Transient Program for LC3540) x= 375, y=272

Horizontal cylinder mode
 Centre=(375,272)
 Scale x:y = 0.0002827:0.0003104
 #L.C.=lc3540
 Time :30.00 sec.

Freeze Continuous OBJmode 0 Centre Scale

Operation successfully completed.

Command: settine
 Enter the time to acquire from the zero second: 30
 Command: Ht_value

Command 'Settime' Screen

Liquid Crystal Thermography (Transient Program for LC3540) x= 375, y=272

Horizontal cylinder mode
 Centre=(375,272)
 Scale x:y = 0.0002827:0.0003104
 #L.C.=lc3540
 Time :30.00 sec.

Freeze Continuous OBJmode 0 Centre Scale

Command: settine
 Enter the time to acquire from the zero second: 30
 Command: Ht_value
 Time(30.000000):

Command 'Ht value' Screen 1

Liquid Crystal Thermography (Transient Program for LC3540) x= 375, y=272

Horizontal cylinder mode
 Centre=(375,272)
 Scale x:y = 0.0002827:0.0003104
 #L.C.=lc3540
 Time :30.00 sec.

Freeze Continuous OBJmode 0 Centre Scale

Time(30.000000):
 centre->(375,272) scale hor:ver-> 0.000283:0.000310
 Liquid Crystal Title name-> LC3540
 USE THE ABOVE UNJUST MAKE SURE IT IS USEFUL ONE!!
 C TO CONFIRM.

Command 'Ht value' Screen 2

Liquid Crystal Thermography (Transient Program for LC3540) x= 375, y=272

Horizontal cylinder mode
 Centre=(375,272)
 Scale x:y = 0.0002827:0.0003104
 #L.C.=lc3540
 Time :30.00 sec.

Freeze Continuous OBJmode 0 Centre Scale

USE THE ABOVE UNJUST MAKE SURE IT IS USEFUL ONE!!
 C TO CONFIRM.
 specimen: K->0.188160 density-> 1150.000000 C-> 1465.300005
 USE THE ABOVE UNJUST MAKE SURE IT IS USEFUL ONE!!
 C TO CONFIRM.

Command 'Ht value' Screen 3

Liquid Crystal Thermography (Transient Program for LC3540) x= 375, y=272

Horizontal cylinder mode
 Centre=(375,272)
 Scale x:y = 0.0002827:0.0003104
 #L.C.=lc3540
 Time :30.00 sec.

Freeze Continuous DBmode 0 Centre Scale

C TO CONFIRM.
 Delta X-pixel-> 5 =0.0014H
 Delta Angle-> 1.00°
 USE THE ABOVE VALUES MAKE SURE IT IS USEFUL ONE!!
 C TO CONFIRM.

Command 'Ht value' Screen 4

Liquid Crystal Thermography (Transient Program for LC3540) x= 375, y=272

Horizontal cylinder mode
 Centre=(375,272)
 Scale x:y = 0.0002827:0.0003104
 #L.C.=lc3540
 Time :30.00 sec.

Freeze Continuous DBmode 0 Centre Scale

USE THE ABOVE VALUES MAKE SURE IT IS USEFUL ONE!!
 C TO CONFIRM. ->X40.000000" UJet-> 0.200000
 Ufmc-> 0.040000 URCK-> 28.658871
 USE THE ABOVE VALUES MAKE SURE IT IS USEFUL ONE!!
 C TO CONFIRM.

Command 'Ht value' Screen 5

Liquid Crystal Thermography (Transient Program for LC3540) x= 375, y=272

Horizontal cylinder mode
 Centre=(375,272)
 Scale x:y = 0.0002827:0.0003104
 #L.C.=lc3540
 Time :30.00 sec.

Freeze Continuous DBmode 0 Centre Scale

C TO CONFIRM.
 Jet temperature->40.000000" UJet-> 0.200000
 USE THE ABOVE VALUES MAKE SURE IT IS USEFUL ONE!!
 C TO CONFIRM.
 Please enter the ambient temperature(°C): 16.81

Command 'Ht value' Screen 6

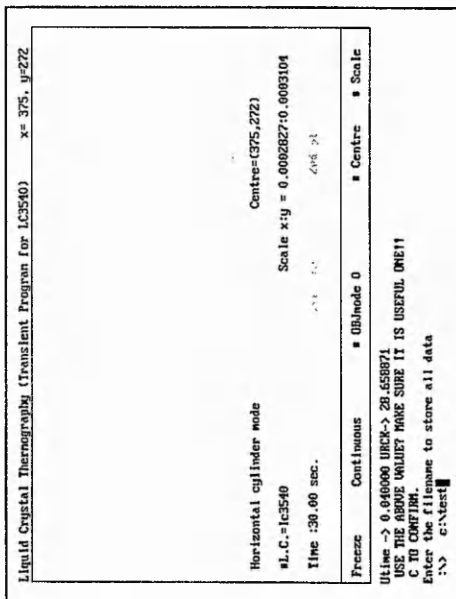
Liquid Crystal Thermography (Transient Program for LC3540) x= 375, y=272

Horizontal cylinder mode
 Centre=(375,272)
 Scale x:y = 0.0002827:0.0003104
 #L.C.=lc3540
 Time :30.00 sec.

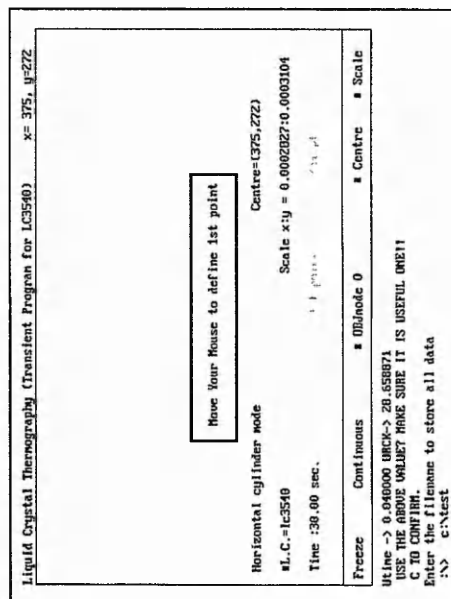
Freeze Continuous DBmode 0 Centre Scale

Please enter the ambient temperature(°C): 16.81
 ULC0 -> 0.257300 Uamb-> 0.200000
 Ufmc -> 0.040000 URCK-> 28.658871
 USE THE ABOVE VALUES MAKE SURE IT IS USEFUL ONE!!
 C TO CONFIRM.

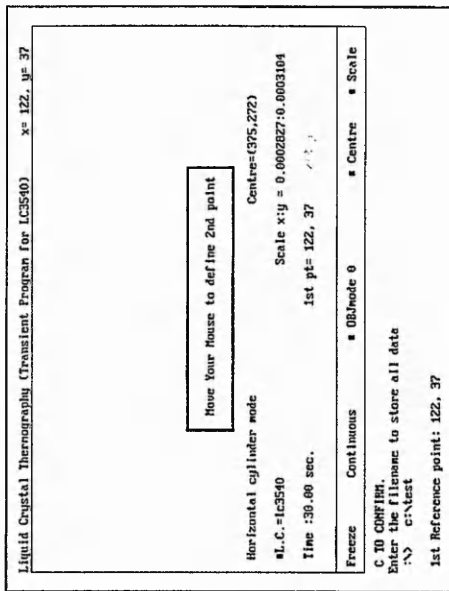
Command 'Ht value' Screen 7



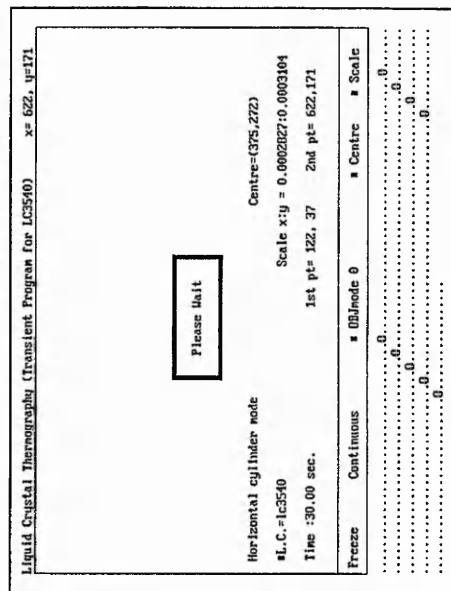
Command 'Ht value' Screen 8



Command 'Ht value' Screen 9



Command 'Ht value' Screen 10



Command 'Ht value' Screen 11

```

Liquid Crystal Thermography (Transient Program for LC3540)
-----
Horizontal cylinder node
#L.C.=LC3540
Time :30.00 sec.
Centre=(375,272)
Scale x:y = 0.0002850:0.0003100
Freeze Continuous 0BJ/node 0 Centre Scale
Command: matrix
Enter the filename to be retrieved: c:\next
Enter the filename to be saved: c:\nexttest
    
```

Command 'Matrix' Screen

```

Liquid Crystal Thermography (Transient Program for LC3540)
-----
Horizontal cylinder node
#L.C.=LC3540
Time :30.00 sec.
Centre=(375,272)
Scale x:y = 0.0002850:0.0003100
Freeze Continuous 0BJ/node 0 Centre Scale
Command: symmetry
Enter the filename to be retrieved: c:\next
Enter the filename to be saved: c:\nexttest
    
```

Command 'Symmetry' Screen

```

Liquid Crystal Thermography (Transient Program for LC3540)
-----
Horizontal cylinder node
#L.C.=LC3540
Time :30.00 sec.
Centre=(375,272)
Scale x:y = 0.0002857:0.0003104
Freeze Continuous 0BJ/node 0 Centre Scale
Command: exit
    
```

Command 'Exit' Screen

Appendix C - Data reduction equation and propagation of uncertainty for the determination of heat transfer coefficient.

Equation (3.13) gives the solution to the one-dimensional transient conduction equation subject to the stated boundary and initial conditions, as

$$\frac{T_{(0,t)} - T_{\text{amb}}}{T_j - T_{\text{amb}}} = \theta = 1 - e^{-\eta} (1 - \text{erf} \sqrt{\eta}) \quad (\text{C.1})$$

where

$$\eta = \frac{h^2 \alpha t}{k^2} = \frac{h^2 t}{k \rho c} \quad (\text{C.2})$$

simplifying Equation (D.1) by putting $\gamma = \sqrt{\eta}$ leads to

$$\theta = 1 - e^{-\gamma^2} (1 - \text{erf}(\gamma)) \quad (\text{C.3})$$

Applying the procedure of Kline and McClintock (1953) to obtain the error in h propagated through these equations, gives

$$\partial h = \left[\left(\frac{\partial h}{\partial t} \delta t \right)^2 + \left(\frac{\partial h}{\partial \sqrt{\rho c k}} \delta \sqrt{\rho c k} \right)^2 + \left(\frac{\partial h}{\partial T_{(0,t)}} \delta T_{(0,t)} \right)^2 + \left(\frac{\partial h}{\partial T_j} \delta T_j \right)^2 + \left(\frac{\partial h}{\partial T_{\text{amb}}} \delta T_{\text{amb}} \right)^2 \right]^{0.5} \quad (\text{C.4})$$

Since, the partial derivatives with respect to t and $\sqrt{\rho ck}$ can be found directly by differentiating equation (C.2):

$$\frac{\partial h}{\partial t} = -\frac{\gamma\sqrt{\rho ck}}{2t^{1.5}} = -\frac{h}{2t}$$

$$\frac{\partial h}{\partial\sqrt{\rho ck}} = -\frac{\gamma}{\sqrt{t}} = -\frac{h}{\sqrt{\rho ck}} \quad (\text{C.5})$$

and the partial derivatives with respect to the measured temperatures are expressed as:

$$\frac{\partial h}{\partial T_{(0,t)}} = \frac{\partial h}{\partial \theta} \frac{\partial \theta}{\partial T_{(0,t)}}$$

$$\frac{\partial h}{\partial T_j} = \frac{\partial h}{\partial \theta} \frac{\partial \theta}{\partial T_j}$$

$$\frac{\partial h}{\partial T_{\text{amb}}} = \frac{\partial h}{\partial \theta} \frac{\partial \theta}{\partial T_{\text{amb}}} \quad \text{where} \quad \frac{\partial h}{\partial \theta} = \frac{\partial h}{\partial \gamma} \frac{\partial \gamma}{\partial \theta} \quad (\text{C.6})$$

The first derivative term $\frac{\partial \gamma}{\partial \theta}$ can be found as follows:

$$\frac{\partial \theta}{\partial \gamma} = \frac{\partial}{\partial \gamma} \left(1 - e^{-\gamma^2} [1 - \text{erf}(\gamma)] \right)$$

$$= \frac{2}{\sqrt{\pi}} - 2\gamma e^{-\gamma^2} [1 - \text{erf}(\gamma)]$$

$$= \frac{2 - 2\sqrt{\pi}\gamma(1 - \theta)}{\sqrt{\pi}}$$

Hence
$$\frac{\partial \gamma}{\partial \theta} = \frac{\sqrt{\pi}}{2 - 2\sqrt{\pi}\gamma(1 - \theta)} \quad (\text{C.7})$$

Differentiating θ with respect to the measured temperature leads to,

$$\begin{aligned}\frac{\partial \theta}{\partial T_{(0,t)}} &= \frac{1}{T_j - T_{amb}} \\ \frac{\partial \theta}{\partial T_j} &= \frac{(T_{(0,t)} - T_{amb})}{(T_j - T_{amb})^2} \\ \frac{\partial \theta}{\partial T_{amb}} &= \frac{T_{(0,t)} - T_{amb}}{(T_j - T_{amb})^2}\end{aligned}\quad (C.8)$$

Substituting the partial derivatives into Equations (C.5):

$$\begin{aligned}\frac{\partial h}{\partial T_{(0,t)}} &= \frac{h}{\beta(T_\infty - T_{amb})} \\ \frac{\partial h}{\partial T_\infty} &= \frac{-h(T_{(0,t)} - T_o)}{\beta(T_\infty - T_o)^2} \\ \frac{\partial h}{\partial T_o} &= \frac{h(T_{(0,t)} - T_{amb})}{\beta(T_\infty - T_o)^2} \quad \text{where } \beta = 2\gamma[\pi^{-0.5} - \gamma(1-\theta)]\end{aligned}\quad (C.9)$$

By substituting these derivatives into Equation (C.4), dividing by h and replacing γ with $\sqrt{\eta}$, yields the uncertainty of heat transfer coefficient:

$$\frac{\partial h}{h} = \left[\left(\frac{\delta t}{2t} \right)^2 + \left(\frac{\delta(\sqrt{\rho c k})}{\sqrt{\rho c k}} \right)^2 + \left(\frac{1}{\beta(T_j - T_{amb})} \right)^2 \left(\delta T_{(0,t)}^2 + (\theta - 1)^2 \delta T_{amb}^2 + \theta^2 \delta T_j^2 \right) \right]^{0.5}$$

$$\text{where } \beta = 2\sqrt{\eta}[\pi^{-0.5} - \sqrt{\eta}(1-\theta)] \quad (C.10)$$

Appendix D - CCD video camera viewing angle analysis in slot jet experiment

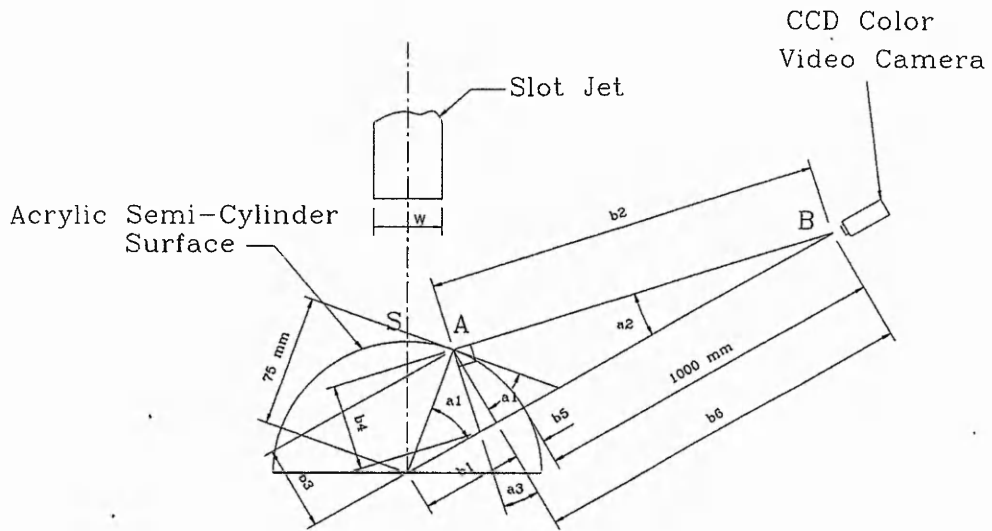


Figure D.1 The geometry of video camera viewing angle on the target surface.

The point A is taken as an example to calculate its corresponding viewing angle. The focal length, 1000 mm of the CCD video camera is fixed at the location B.

$$\text{Radius of semi-cylinder surface} = r = b1 + b5 = 75 \text{ mm} \quad (\text{D.1})$$

$$\sin(a1) = b3 / r \quad (\text{D.2})$$

Hence,
$$a1 = \sin^{-1}(b3 / r) \quad (\text{D.3})$$

$$b1 = \sqrt{r^2 - (b3)^2} \quad (\text{D.4})$$

$$b5 = r - b1 \quad (\text{D.5})$$

$$b6 = b5 + 1000 \text{ mm} \quad (\text{D.6})$$

$$\tan(a2) = b3 / b6 \quad (\text{D.7})$$

Hence,
$$a_2 = \tan^{-1}(b_3 / b_6) \quad (D.8)$$

$$b_2 = \sqrt{(b_6)^2 + (b_3)^2} \quad (D.9)$$

$$\tan(a_2) = b_4 / b_2 \quad (D.10)$$

Hence
$$b_4 = \tan(a_2) \times b_2 \quad (D.11)$$

$$\cos(a_3) = b_3 / b_4 \quad (D.12)$$

Hence
$$a_3 = \cos^{-1}(b_3 / b_4) \quad (D.13)$$

As result, the video camera viewing angle = $a_1 + a_3$ (D.14)

At 65° angular line and 0° stagnation line are equivalent to 0° and 68.7° of video camera viewing angles as shown in Figure D.2.

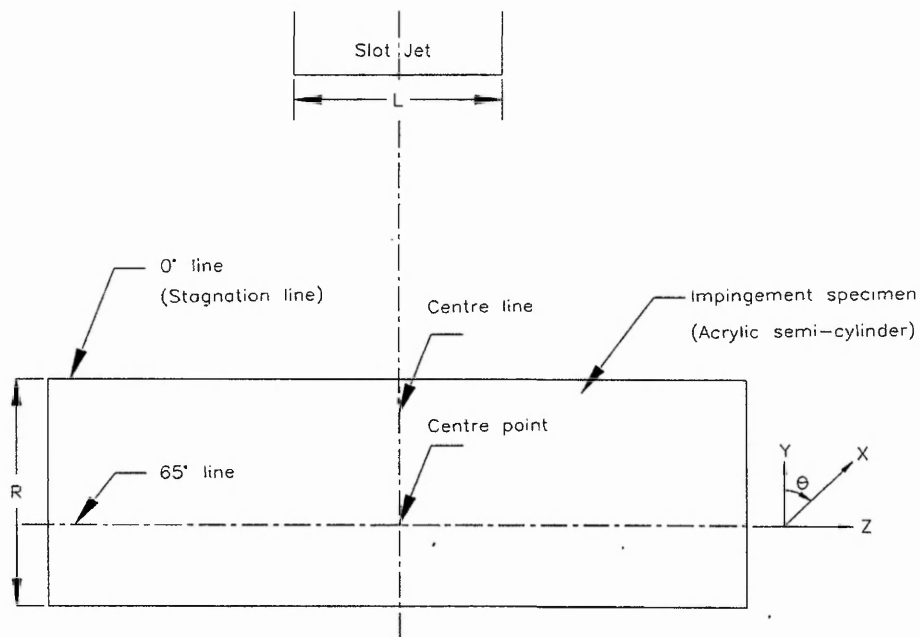


Figure D.2 Schematic diagram of the representation of video camera viewing angle on the semi-cylinder specimen, $R=75$ mm.

Appendix E - A typical PHOENICS data input file, Q1 and GROUND.for coding for computing the heat transfer and flow characteristics on a semi-cylindrical convex surface due to an impinging slot jet .

E.1 Q1 file

TALK=F;RUN(1, 1);VDU=VGAMOUSE

GROUP 1.

TEXT(POLAR GRID, Z/W=2, Vexit=35.8m/s, 0.8% turbulence intensity)

**Vexit is mean flat jet exit; IX1 is edge of jet.
 **Router is semi-cylinder outer radius +2SLOTW (for ZW=2 case).
 **RINNER is a PHOENICS variable that allows the y extent to be measured from the surface of the semi-cylinder.
 **angU and angV are the angles of the velocity components which constitute the mean jet exit velocity. Since in polar coordinates, X is measured in radians, the magnitude of the angles for each inlet cell is equal to XULAST*XFRAC(I) where I is the X cell. Remember that velocities are store data the upstream side of the cells, not at the cell centres. This means that the inlet velocity components (which make up the resultant jet exit velocity) are calculated using different values of XFRAC.

REAL(angU,angV,Vin,Uin,Router,TKEin,EPSin,GFRAC)

REAL(Tin,Tsurf,GK,SLOTW,CP,Vexit)

INTEGER(RZW)

* INLET TEMPERATURE

Tin=40

* SURFACE AMBIENT TEMPERATURE

Tsurf=17.1

* CONDUCTIVITY OF AIR AT Tin

GK=0.02724

* WIDTH OF THE SLOT JET NOZZLE

SLOTW=6.25E-3

* SPECIFIC HEAT OF AIR AT Tin

CP=1005.6

* EXIT VELOCITY

Vexit=35.75

* SLOT JET-IMPINGEMENT SURFACE RATIO

RZW=2

* INNER RADIUS -RADIUS OF SEMI-CYLINDER

RINNER=0.075

* OUTER RADIUS - MEASURED FROM CENTRE OF CYLINDER TO NOZZLE

Router=RINNER+RZW*SLOTW

** Egde of jet is IX1

** NO. OF CELLS IN THE FIVE REGIONS

INTEGER(IX1,IX2,IX3,IX4,IX5)

IX1=8

IX2=16

IX3=8

IX4=54

IX5=24

GROUP 3. X-direction grid specification

**QUADRANT ONLY modelled = 0.51π
 CARTES=F
 * TOTAL NO. OF CELLS IN THE WHOLE DOMAIN OF X-DIRECTION
 NX=IX1+IX2+IX3+IX4+IX5
 * NO. OF REGIONS IN X-DIRECTION
 NREGX=5

** First region (IX1 cells) is the jet inlet, IX=1 to IX1:
 IREGX=1;GRDPWR(X,IX1,0.003125/Router,1.0)

** Second region covers the shear layer:
 IREGX=2;GRDPWR(X,IX2,0.00625/Router,1.0)

** Subsequent regions gradually enlarge the cell size for the remainder of the domain:
 IREGX=3;GRDPWR(X,IX3,0.00625/Router,1.0)
 IREGX=4;GRDPWR(X,IX4,0.0625/Router,1.0)
 IREGX=5;GRDPWR(X,IX5,0.0625/Router,1.0)

Group 4. Y Grid

**NO. OF CELLS IN THE WHOLE DOMAIN OF Y-DIRECTION
 INTEGER(IY1,IY2)
 IY1=14
 IY2=40
 * RADIUS OF CYLINDER
 * RINNER=0.075
 * TOTAL NO. OF CELLS IN WHOLE DOMAIN OF Y-DIRECTION
 NY=IY1+IY2

* NO. OF REGIONS IN Y-DIRECTION
 NREGY=2

** First region covers near wall region. The number of cells should be varied in order to find the best near wall cell size that will give a reasonable value of y^+ .

IREGY=1;GRDPWR(Y,IY1,0.14*(Router-RINNER),1.0)

** Second region invokes a uniform cell size over domain.

IREGY=2;GRDPWR(Y,IY2,0.86*(Router-RINNER),1.0)

GROUP 5. Z-direction grid specification

GROUP 6. Body-fitted coordinates or grid distortion

GROUP 7. Variables stored, solved & named

NAME(46)=BLOK ; NAME(47)=DEN1 ; NAME(48)=PRPS

SOLVE(P1,U1,V1,TEM1,BLOK,DEN1,PRPS)

STORE(ENUT,BLOK,DEN1,PRPS)

* CREATE STORAGE FOR SELF-DEFINED VARIABLES
 * C1=HEAT TRANSFER COEFFICIENT
 * C2=NUSSELT NUMBER
 * C3=STANTON NUMBER

STORE(C1,C2,C3)

SOLUTN(P1,Y,Y,Y,N,N,N)
 SOLUTN(U1,Y,Y,N,N,N,N)
 SOLUTN(V1,Y,Y,N,N,N,N)
 SOLUTN(TEM1,Y,Y,Y,N,N,Y)

* K-E TURBULENCE MODEL IS USED IN THIS CASE

TURMOD(KEMODL)

IVARBK=-1
 ISOLBK=1

GROUP 8. Terms (in differential equations) & devices

DIFCUT=0.5

NEWRH1=T
 NEWENL=T

ISOLX=0;ISOLY=0;ISOLZ=0

GROUP 9. Properties of the medium (or media)

**Typical thermophysical property data may be expressed as
 the function of temperature within the range from
 273 to 300 deg C as given below:

$RHO1 = 1.177 - ((1.177 - 1.284) * ((300 - (Tsurf + 273)) / (300 - 273)))$
 $ENUL = 1.568E-5 - ((1.568E-5 - 1.343E-5) * ((300 - (Tsurf + 273)) / (300 - 273)))$
 $PRNDTL(TEM1) = 0.707 - ((0.707 - 0.713) * ((300 - (Tsurf + 273)) / (300 - 273)))$
 PRT(TEM1)=0.9

GROUP 10. Inter-phase-transfer processes and properties

GROUP 11. Initialization of variable or porosity fields

** FOR THE FIRST RUN ONLY make initial guesses:
 FIINIT(U1) = Vexit/10.0 ; FIINIT(V1) = Vexit/50.0;
 FIINIT(TEM1) = Tsurf ; FIINIT(P1) = Vexit*RHO1/1000.0
 FIINIT(EP) = EPSin/2 ; FIINIT(KE) = TKEin/2
 FIINIT(BLOK) = 1.0

```

** For RESTART runs tell PHOENICS to read data from PHI file
and invoke RESTRST(ALL) command
*FIINIT(U1) =READFI ; FIINIT(V1) =READFI
*FIINIT(TEM1) =READFI ; FIINIT(P1) =READFI
*FIINIT(EP) =READFI ; FIINIT(KE) =READFI
*FIINIT(BLOK) =READFI
*RESTRT(ALL)

```

GROUP 12. Convection and diffusion adjustments

GROUP 13. Boundary conditions and special sources

** GFRAC = XFRAC(II-1), ie. the distance to the cell before last.

GFRAC=0

```

** Define jet inlet velocity**
** IX1 denotes as the edge of the jet, then IX1 can be
set to any value, as long as it is defined as that value in
Group 1, and the following DO loop will work satisfactorily.
ie. A PATCH will be created for every IX1. This would allow
you to define a non-uniform inlet velocity.
** Notice that the V velocity is defined as -V since the y
grid is measured from RINNER.

```

DO II=1,IX1

```

** X velocity component of Vexit:
angU=XULAST*XFRAC(II)
Uin=Vexit*SIN(angU)

```

```

** Y component of Vexit:
IF(II.EQ.1) THEN
angV=0.5*XULAST*XFRAC(II)
ELSE
angV=angU-0.5*XULAST*(XFRAC(II)-GFRAC)
ENDIF
Vin=Vexit*COS(angV)

```

```

** Assuming turbulence intensity(TI)=1% of inlet velocity and
that TI is equal in three-dimensions ie. isotropic, then for
flow from Shaw (1992) :TKE=0.5(u**2 + v**2)

```

TKEin=0.5*((0.008*Uin)**2+(0.008*Vin)**2)

```

** EPSin BASED ON Lmix=0.1W, where W is jet width, according to
Lauder and Spalding (1972, 1974).

```

EPSin=0.1643*(TKEin**1.5)/(0.1*SLOTW)

```

INLET(JET:II:,NORTH,;II:,;II:,NY,NY,1,1,1,1)
VALUE(JET:II:,P1,Vin*RHO1)
VALUE(JET:II:,V1,-Vin)
VALUE(JET:II:,U1,Uin)
VALUE(JET:II:,EP,EPSin)
VALUE(JET:II:,KE,TKEin)

```

VALUE(JET:II;,TEM1,Tin)

** Set GFRAC to be old value of circumferential(X) distance:

GFRAC=XFRAC(II)

ENDDO

** Set the cells near the jet exit to be wall cells, to approxi
the thickness of the nozzle.

PATCH(NOZZLE,NWALL,IX1+1,IX1+IX2,NY,NY,1,1,1,1)
COVAL(NOZZLE,U1,FIXVAL,0.0)
COVAL(NOZZLE,V1,FIXVAL,0.0)
COVAL(NOZZLE,TEM1,FIXVAL,Tsurf)

** Set outlet boundary conditions

By using the SAME argument, we ensure that if there is any
inflow on these outflow boundaries, its properties will be
equal to the outflow (ie. will not be set to zero as default).

** Outflow**: Upper entrainment boundary

PATCH(ENTRAIN,NORTH,IX1+IX2+1,NX,NY,NY,1,1,1,1)
COVAL(ENTRAIN,P1,FIXVAL,0.0)
COVAL(ENTRAIN,U1,ONLYMS,SAME)
COVAL(ENTRAIN,V1,ONLYMS,SAME)
COVAL(ENTRAIN,EP,ONLYMS,SAME)
COVAL(ENTRAIN,KE,ONLYMS,SAME)
COVAL(ENTRAIN,TEM1,ONLYMS,SAME)

** Downstream outlet

PATCH(OUTLET,EAST,NX,NX,1,NY,1,1,1,1)
COVAL(OUTLET,P1,FIXVAL,0.0)
COVAL(OUTLET,U1,ONLYMS,SAME)
COVAL(OUTLET,V1,ONLYMS,SAME)
COVAL(OUTLET,EP,ONLYMS,SAME)
COVAL(OUTLET,KE,ONLYMS,SAME)
COVAL(OUTLET,TEM1,ONLYMS,SAME)

** Impingement surface

GRND2 sets the logarithmic law-of-the-wall as defined in
Rosten and Worrell (1988):

PATCH(IMP,SWALL,1,NX,1,1,1,1,1,1)
COVAL(IMP,U1,GRND2,0.0)
COVAL(IMP,V1,GRND2,0.0)
COVAL(IMP,EP,GRND2,GRND2)
COVAL(IMP,KE,GRND2,GRND2)
COVAL(IMP,TEM1,GRND2,Tsurf)

EGWF=T

GROUP 15. Termination of sweeps

LSWEEP=8000

RESREF(U1)=1.E-8
 RESREF(V1)=1.E-8
 RESREF(P1)=1.E-8
 RESREF(KE)=1.E-8
 RESREF(EP)=1.E-8
 RESREF(TEM1)=1.E-8

GROUP 16. Termination of iterations

GROUP 17. Under-relaxation devices

** It is necessary to start with FALSDT relaxation for the vectors
 to allow them to fluctuate. Once stability has been obtained
 then this can be changed to LINRLX for all variables.

RELAX(P1,LINRLX,0.1);RELAX(TEM1,FALSDT,0.1)
 RELAX(U1,FALSDT,0.1);RELAX(V1,FALSDT,0.1)
 RELAX(EP,FALSDT,0.1);RELAX(KE,FALSDT,0.1)

GROUP 18. Limits on variables or increments to them

GROUP 19. Special calls from EARTH to GROUND

*COMMUNICATE WITH OWN GROUND.FOR PROGRAM

PATCH(HEATLOSS,SWALL,#1,#NREGX,#1,#1,#1,#1,1,1)
 COVAL(HEATLOSS,TEM1,GRND,Tsurf)
 *END

USEGRD=T

*COMMUNICATE WITH OWN GROUND.FOR PROGRAM

RG(1)=Tin
 RG(2)=Tsurf
 RG(3)=GK
 RG(4)=SLOTW
 RG(5)=RHO1
 RG(6)=CP
 RG(7)=Vexit
 RG(8)=RINNER

*END

GROUP 20. Preliminary print-out

ECHO=T

GROUP 21. Print-out of variables

```
OUTPUT(P1,Y,Y,Y,Y,Y,Y)
OUTPUT(U1,Y,Y,Y,Y,Y,Y)
OUTPUT(V1,Y,Y,Y,Y,Y,Y)
OUTPUT(ENUT,Y,Y,Y,Y,Y,Y)
OUTPUT(EP,Y,Y,Y,Y,Y,Y)
OUTPUT(KE,Y,Y,Y,Y,Y,Y)
OUTPUT(TEM1,Y,Y,Y,Y,Y,Y)
OUTPUT(BLOK,N,N,Y,N,N,N)
OUTPUT(DEN1,N,N,Y,N,N,N)
OUTPUT(PRPS,N,N,Y,N,N,N)
```

```
WALPRN=T
INIFLD=T
```

GROUP 22. Spot-value print-out

```
* MONITOR POINT IN X,Y,Z-PLANE
IXMON=12;IYMON=20;IZMON=1
```

```
TSTSWP=-1
```

GROUP 23. Field print-out and plot control

```
* IXPRL VALUE IS CHANGED IF NX IS CHANGED
IXPRF=1;IXPRL=NX
IYPRF=1;IYPRL=NY
NXPRIN=1;NYPRIN=1
NPLT=20
```

```
ITABL=3
NUMCLS=6
```

GROUP 24. Dumps for restarts

```
SAVE=T
STOP
```



```

EQUIVALENCE (GVexit,RG(7))
EQUIVALENCE (GRINNER,RG(8))

IXL=IABS(IXL)
IF(IGR.EQ.13) GO TO 13
IF(IGR.EQ.19) GO TO 19
GO TO (1,2,3,4,5,6,25,8,9,10,11,12,13,14,25,25,25,25,19,20,25,
125,23,24),IGR
25 CONTINUE
RETURN
C*****
C
C--- GROUP 1. Run title and other preliminaries
C
  1 GO TO (1001,1002,1003),ISC

C * -----GROUP 1 SECTION 3 -----
C--- Use this group to create storage via GXMAKE which it is not
C   necessary to dump to PHI for restarts
C
  1003 CONTINUE
  GO TO 25
C
  1001 CONTINUE
  c  CALL MAKE(DYV2D)
  CALL MAKE(DYG2D)
  c  CALL MAKE(DXG2D)
  CALL MAKE(XG2D)
C
C   User may here change message transmitted to the VDU screen
C   IF(IGR.EQ.1.AND.ISC.EQ.1) THEN
C     CALL WRYT40('PHOENICS VERSION NUMBER IS : 2.2 ')
C     CALL WRYT40('GROUND CALCS HEAT TRANSFER COEFFICIENTS. ')
C   ENDIF
C
  RETURN
  1002 CONTINUE
  RETURN
C*****
C
C--- GROUP 2. Transience; time-step specification
C
  2 CONTINUE
  RETURN
C*****
C
C--- GROUP 3. X-direction grid specification
C
  3 CONTINUE
  RETURN
C*****
C
C--- GROUP 4. Y-direction grid specification
C
  4 CONTINUE
  RETURN
C*****

```

```

C
C--- GROUP 5. Z-direction grid specification
C
  5 CONTINUE
  RETURN
C*****
C
C--- GROUP 6. Body-fitted coordinates or grid distortion
C
  6 CONTINUE
  RETURN
C*****
C * Make changes for this group only in group 19.
C--- GROUP 7. Variables stored, solved & named
C*****
C
C--- GROUP 8. Terms (in differential equations) & devices
C
  8 GO TO (81,82,83,84,85,86,87,88,89,810,811,812,813,814,815,816)
  1,ISC
  81 CONTINUE
C * ----- SECTION 1 -----
C For U1AD.LE.GRND--- phase 1 additional velocity. Index VELAD
  RETURN
  82 CONTINUE
C * ----- SECTION 2 -----
C For U2AD.LE.GRND--- phase 2 additional velocity. Index VELAD
  RETURN
  83 CONTINUE
C * ----- SECTION 3 -----
C For V1AD.LE.GRND--- phase 1 additional velocity. Index VELAD
  RETURN
  84 CONTINUE
C * ----- SECTION 4 -----
C For V2AD.LE.GRND--- phase 2 additional velocity. Index VELAD
  RETURN
  85 CONTINUE
C * ----- SECTION 5 -----
C For W1AD.LE.GRND--- phase 1 additional velocity. Index VELAD
  RETURN
  86 CONTINUE
C * ----- SECTION 6 -----
C For W2AD.LE.GRND--- phase 2 additional velocity. Index VELAD
  RETURN
  87 CONTINUE
C * ----- SECTION 7 ---- Volumetric source for gala
  RETURN
  88 CONTINUE
C * ----- SECTION 8 ---- Convection fluxes
C--- Entered when UCONV =.TRUE.; block-location indices are:
C LD11 for east and north (accessible at the same time),
C LD12 for west and south (accessible at the same time),
C LD2 for high (which becomes low for the next slab).
C User should provide INDVAR and NDIREC IF's as appropriate.
  RETURN
  89 CONTINUE
C * ----- SECTION 9 ---- Diffusion coefficients

```

```

C--- Entered when UDIFF =.TRUE.; block-location indices are LAE
C   for east, LAW for west, LAN for north, LAS for
C   south, LD11 for high, and LD11 for low.
C   User should provide INDVAR and NDIREC IF's as above.
C   EARTH will apply the DIFCUT and GP12 modifications after the user
C   has made his settings.
C
C   RETURN
810 CONTINUE
C * ----- SECTION 10 --- Convection neighbours
C   RETURN
811 CONTINUE
C * ----- SECTION 11 --- Diffusion neighbours
C   RETURN
812 CONTINUE
C * ----- SECTION 12 --- Linearised sources
C   RETURN
813 CONTINUE
C * ----- SECTION 13 --- Correction coefficients
C   RETURN
814 CONTINUE
C * ----- SECTION 14 --- User's own solver
C   RETURN
815 CONTINUE
C * ----- SECTION 15 --- Change solution
C   RETURN
816 CONTINUE
C * ----- SECTION 16 --- Change DVEL/DPs
C   RETURN
C
C * See the equivalent section in GREX for the indices to be
C   used in sections 7 - 16
C
C * Make all other group-8 changes in GROUP 19.
C*****
C
C--- GROUP 9. Properties of the medium (or media)
C
C   The sections in this group are arranged sequentially in their
C   order of calling from EARTH. Thus, as can be seen from below,
C   the temperature sections (10 and 11) precede the density
C   sections (1 and 3); so, density formulae can refer to
C   temperature stores already set.
C   9 GO TO (91,92,93,94,95,96,97,98,99,900,901,902,903,904,905),ISC
C*****
900 CONTINUE
C * ----- SECTION 10 -----
C   For TMP1.LE.GRND----- phase-1 temperature Index TEMP1
C   RETURN
901 CONTINUE
C * ----- SECTION 11 -----
C   For TMP2.LE.GRND----- phase-2 temperature Index TEMP2
C   RETURN
902 CONTINUE
C * ----- SECTION 12 -----
C   For EL1.LE.GRND----- phase-1 length scale Index LEN1
C   RETURN

```

```

903 CONTINUE
C * ----- SECTION 13 -----
C For EL2.LE.GRND----- phase-2 length scale Index LEN2
RETURN
904 CONTINUE
C * ----- SECTION 14 -----
C For SOLVE(TEM1)----- phase-1 specific heat
RETURN
905 CONTINUE
C * ----- SECTION 15 -----
C For SOLVE(TEM2)----- phase-2 specific heat
RETURN
91 CONTINUE
C * ----- SECTION 1 -----
C For RHO1.LE.GRND--- density for phase 1    Index DEN1
RETURN
92 CONTINUE
C * ----- SECTION 2 -----
C For DRH1DP.LE.GRND--- D(LN(DEN))/DP for phase 1
C                               Index D1DP
RETURN
93 CONTINUE
C * ----- SECTION 3 -----
C For RHO2.LE.GRND--- density for phase 2    Index DEN2
RETURN
94 CONTINUE
C * ----- SECTION 4 -----
C For DRH2DP.LE.GRND--- D(LN(DEN))/DP for phase 2
C                               Index D2DP
RETURN
95 CONTINUE
C * ----- SECTION 5 -----
C For ENUT.LE.GRND--- reference turbulent kinematic viscosity
C                               Index VIST
RETURN
96 CONTINUE
C * ----- SECTION 6 -----
C For ENUL.LE.GRND--- reference laminar kinematic viscosity
C                               Index VISL
RETURN
97 CONTINUE
C * ----- SECTION 7 -----
C For PRNDTL(.).LE.GRND--- laminar PRANDTL nos., or diffusivity
C                               Index LAMPR
RETURN
98 CONTINUE
C * ----- SECTION 8 -----
C For PHINT(.).LE.GRND--- interface value of first phase
C                               Index FII1
RETURN
99 CONTINUE
C * ----- SECTION 9 -----
C For PHINT(.).LE.GRND--- interface value of second phase
C                               Index FII2
RETURN
C*****
C

```

```

C--- GROUP 10. Inter-phase-transfer processes and properties
C
  10 GO TO (101,102,103,104),ISC
  101 CONTINUE
C * ----- SECTION 1 -----
C   For CFIPS.LE.GRND--- inter-phase friction coeff.
C                               Index INTFRC
  RETURN
  102 CONTINUE
C * ----- SECTION 2 -----
C   For CMDOT.EQ.GRND- inter-phase mass transfer Index INTMDT
  RETURN
  103 CONTINUE
C * ----- SECTION 3 -----
C   For CINT().EQ.GRND--- phase1-to-interface transfer coefficients
C                               Index COI1
  RETURN
  104 CONTINUE
C * ----- SECTION 4 -----
C   For CINT().EQ.GRND--- phase2-to-interface transfer coefficients
C                               Index COI2
  RETURN
C*****
C
C--- GROUP 11. Initialization of variable or porosity fields
C                               Index VAL
  11 CONTINUE
  RETURN
C*****
C
C--- GROUP 12. Convection and diffusion adjustments
C
  12 CONTINUE
  RETURN
C*****
C
C--- GROUP 13. Boundary conditions and special sources
C                               Index for Coefficient - CO
C                               Index for Value - VAL
  13 CONTINUE
  GO TO (130,131,132,133,134,135,136,137,138,139,1310,
  11311,1312,1313,1314,1315,1316,1317,1318,1319,1320,1321),ISC
  130 CONTINUE

C----- SECTION 1 ----- coefficient = GRND

  IF(ISWEEP.NE.LSWEEP-1) GOTO 131

  OPEN(UNIT=20,STATUS='UNKNOWN',FILE='ALL.DAT')

  IF(NPATCH.EQ.'HEATLOSS') THEN
  IF(INDVAR.EQ.ITEM1) THEN

    CALL GETYX(C1,GHTC,200,200)
    CALL GETYX(C2,GNU,200,200)
    CALL GETYX(C3,GST,200,200)
    CALL GETYX(ITEM1,GTEMP,200,200)

```

```

CALL GETYX(DYG2D,GDIST,200,200)
CALL GETYX(XG2D,RAD,200,200)
CALL GETYX(U1,GU1,200,200)
CALL GETYX(V1,GV1,200,200)
CALL GETYX(P1,GP1,200,200)
CALL GETYX(EP,GEP,200,200)
CALL GETYX(KE,GKE,200,200)

ENDIF
ENDIF

WRITE(20,1199)

1199  FORMAT(' IX ', XCRAD ' ', XRAD ' ', XANGLE',
1    ' XRARCW', GHTC ' ', GNU ' ',
1    '   GST ', GU1 ' ', GV1 ' ',
1    '   GP1 ', GEP ' ', GKE ' ',
1    '   GTEMP ')
      DO IY=1,NY
        WRITE(20,1990)IY
1990  FORMAT('IY=',I3)
      DO IX=1,NX

        XCRAD(IY,IX)=RAD(IY,IX)

        IF(IX.EQ.1) THEN
          XRAD(IY,IX)=2*RAD(IY,IX)
          XRARCW(IY,IX)=(RG(8)/RG(4))*XRAD(IY,IX)
        ELSE
          XRAD(IY,IX)=2*RAD(IY,IX)-XRAD(IY,IX-1)
          XRARCW(IY,IX)=(RG(8)/RG(4))*XRAD(IY,IX)
        ENDIF
        XANGLE(IY,IX)=(XRAD(IY,IX)/3.141592654)*180

        WRITE(20,1200)IX,XCRAD(IY,IX),XRAD(IY,IX),XANGLE(IY,IX),
1    XRARCW(IY,IX),GHTC(IY,IX),GNU(IY,IX),GST(IY,IX),GU1(IY,IX),
1    GV1(IY,IX),GP1(IY,IX),GEP(IY,IX),GKE(IY,IX),GTEMP(IY,IX)
1200  FORMAT(I3,' ',F10.6,' ',F10.6,' ',F8.4,' ',F8.4,' ',
1    F12.4,' ',F12.4,' ',F14.6,' ',F12.4,' ',F14.6,' ',
1    F12.4,' ',F14.4,' ',F12.4,' ',F12.4)

      ENDDO
    ENDDO

    RETURN
131 CONTINUE
C----- SECTION 2 ----- coefficient = GRND1
    RETURN
132 CONTINUE
C----- SECTION 3 ----- coefficient = GRND2
    RETURN
133 CONTINUE
C----- SECTION 4 ----- coefficient = GRND3
    RETURN
134 CONTINUE
C----- SECTION 5 ----- coefficient = GRND4
    RETURN

```

```

135 CONTINUE
C----- SECTION 6 ----- coefficient = GRND5
  RETURN
136 CONTINUE
C----- SECTION 7 ----- coefficient = GRND6
  RETURN
137 CONTINUE
C----- SECTION 8 ----- coefficient = GRND7
  RETURN
138 CONTINUE
C----- SECTION 9 ----- coefficient = GRND8
  RETURN
139 CONTINUE
C----- SECTION 10 ----- coefficient = GRND9
  RETURN
1310 CONTINUE
C----- SECTION 11 ----- coefficient = GRND10
  RETURN
1311 CONTINUE
C----- SECTION 12 ----- value = GRND
  RETURN
1312 CONTINUE
C----- SECTION 13 ----- value = GRND1
  RETURN
1313 CONTINUE
C----- SECTION 14 ----- value = GRND2
  RETURN
1314 CONTINUE
C----- SECTION 15 ----- value = GRND3
  RETURN
1315 CONTINUE
C----- SECTION 16 ----- value = GRND4
  RETURN
1316 CONTINUE
C----- SECTION 17 ----- value = GRND5
  RETURN
1317 CONTINUE
C----- SECTION 18 ----- value = GRND6
  RETURN
1318 CONTINUE
C----- SECTION 19 ----- value = GRND7
  RETURN
1319 CONTINUE
C----- SECTION 20 ----- value = GRND8
  RETURN
1320 CONTINUE
C----- SECTION 21 ----- value = GRND9
  RETURN
1321 CONTINUE
C----- SECTION 22 ----- value = GRND10
  RETURN
C*****
C
C--- GROUP 14. Downstream pressure for PARAB=.TRUE.
C
14 CONTINUE
  RETURN

```

```

C*****
C* Make changes to data for GROUPS 15, 16, 17, 18 GROUP 19.
C*****
C
C--- GROUP 19. Special calls to GROUND from EARTH
C
  19 GO TO (191,192,193,194,195,196,197,198,199,1910,1911),ISC
  191 CONTINUE
C * ----- SECTION 1 ---- Start of time step.
  RETURN
  192 CONTINUE
C * ----- SECTION 2 ---- Start of sweep.
  RETURN
  193 CONTINUE
C * ----- SECTION 3 ---- Start of iz slab.
  RETURN
  194 CONTINUE
C * ----- SECTION 4 ---- Start of iterations over slab.
  RETURN
  1911 CONTINUE
C * ----- SECTION 11---- After calculation of convection
C          fluxes for scalars, and of volume
C          fractions, but before calculation of
C          scalars or velocities
  RETURN
  199 CONTINUE
C * ----- SECTION 9 ---- Start of solution sequence for
C          a variable
  RETURN
  1910 CONTINUE
C * ----- SECTION 10---- Finish of solution sequence for
C          a variable
  RETURN
  195 CONTINUE
C * ----- SECTION 5 ---- Finish of iterations over slab.
  RETURN
  196 CONTINUE
C * ----- SECTION 6 ---- Finish of iz slab.
  RETURN
  197 CONTINUE
C * ----- SECTION 7 ---- Finish of sweep.
  RETURN
  198 CONTINUE
C * ----- SECTION 8 ---- Finish of time step.
C
  RETURN
C*****
C
C--- GROUP 20. Preliminary print-out
C
  20 CONTINUE
  RETURN

```

```
C*****  
C* Make changes to data for GROUPS 21 and 22 only in GROUP 19.  
C*****  
C  
C--- GROUP 23. Field print-out and plot control  
  23 CONTINUE  
  RETURN  
C*****  
C  
C--- GROUP 24. Dumps for restarts  
C  
  24 CONTINUE  
  END
```

Publications